



Norwegian University of
Science and Technology

Measuring Vibrations and assessing Dynamic Properties of tall Timber Buildings

Måling av vibrasjoner og kartlegging av
dynamiske egenskaper i høye trehus

Magnus Fjeld Olsen
Ola Hansen

Civil and Environmental Engineering

Submission date: June 2016

Supervisor: Kjell A Malo, KT



Co-supervisor: Ole Andre Øiseth, KT

Norwegian University of Science and Technology
Department of Structural Engineering



MASTER THESIS 2016

SUBJECT AREA: Timber Structures, Dynamics	DATE: 10 th of june, 2016	NO. OF PAGES: 187
--	---	----------------------

TITLE:	
English title	
Norwegian title	
BY:	 
Magnus Fjeld Olsen and Ola Hansen	

SUMMARY:
The main goal behind this thesis is to evaluate the dynamic properties of the world's tallest timber building, Treet, in Bergen. The dynamic properties will be extracted from recorded acceleration time series. Measurements will also be acquired and evaluated for Moholt 50|50, a new student housing project initiated by Studentsamskipnaden i Trondheim.

Acceleration measurements are performed using accelerometers from Kistler, PCB Piezotronics, and data acquisition hardware from National Instruments. The acceleration data is then processed using a method called *Covariance-Driven Stochastic Subspace Identification*. From this method the natural frequencies, mode shapes and damping ratios are extracted. These parameters are then compared to the results from numerical models and engineering assumptions that were made during the planning of the respective buildings. An evaluation of the maximum accelerations and displacements is also performed. Finally, a numerical model of Moholt 50|50 is created in Abaqus/CAE in order to investigate how a numerical model for this type of structure predicts dynamic behaviour.

Results obtained from the measurements show that the engineers responsible for predicting the dynamic behaviour of Treet were satisfactory close to actual properties, although the natural frequencies seem to be consistently higher due to non-structural effects. The measured dynamic properties at Moholt 50|50 were close to the natural frequencies and mode shapes predicted by the numerical model. However, it is unknown whether the responsible engineers predicted the same results. Also, the damping ratios at Moholt are highly uncertain due to the excitation system not coinciding well with the white noise assumption used for *Operational Modal Analysis*.

RESPONSIBLE TEACHER: Kjell Arne Malo

SUPERVISORS: Kjell Arne Malo and Ole Øiseth

CARRIED OUT AT: Department of Structural Engineering, NTNU

MASTEROPPGAVE 2016

for

Magnus Fjeld Olsen og Ola Hansen

Måling av vibrasjoner og karlegging av dynamiske egenskaper i høye trehus

Measuring vibrations and assessing dynamic properties of tall timber buildings

Høye trehus er i vinden for tiden, da det anses å ligge både økonomiske og miljømessige gevinster i å benytte tre som hovedbæresystem. Dette er under forutsetning at særskilte utfordringer knyttet til høye trehus blir håndtert. En av disse utfordringene kommer i form av komfortkriterier angående høye akselerasjoner i toppetasjene. For å kunne temme akselerasjonene som kan oppstå, under for eksempel sterk vind, er det essensielt å ha god kunnskap om de dynamiske egenskapene som ligger til grunn for prosjekteringen.

I denne masteroppgaven skal de dynamiske egenskapene i to høye trehus kartlegges. For å finne fram til disse, skal nytt og nøyaktig måleutstyr tas i bruk. Måleutstyret skal programmeres til å samle inn akselerasjonsdata. Videre skal målingene analyseres for å kartlegge de dynamiske egenskapene ved hjelp av analyseverktøyet Operational Modal Analysis.

Forslag til gjennomføring av oppgaven:

1. Kandidatene setter seg inn i funksjonaliteten til måleutstyret.
2. Kandidatene setter seg inn i bruk av nødvendig programmeringsverktøy (LabVIEW) for å programmere utstyret.
3. Kandidatene benytter Treet og Moholt 50|50 som måleobjekter.
4. Kandidatene setter seg inn i nødvendig teori for å analysere måledata.
5. Kandidatene benytter måledata for å kartlegge de dynamiske egenskapene til måleobjektene.
6. Kandidatene sammenfatter og lager en konklusjon der resultater fra målingene sammenlignes med antakelser foretatt i prosjekteringen av byggene.

Etter samråd med veiledere kan kandidatene konsentrere sitt arbeide til spesielle deler av oppgaven, eller trekke inn andre aspekter.

Besvarelsen organiseres i henhold til gjeldende retningslinjer.

Veiledere: Kjell Arne Malo og Ole Øiseth

Besvarelsen skal leveres til Institutt for konstruksjonsteknikk innen 10. juni 2016.

NTNU, juni, 2016

Magnus Fjeld Olsen og Ola Hansen
Kandidater

Preface

This master thesis is the end of the 5-year study programme Master of Science in Civil Engineering. It is carried out at the Department of Structural Engineering, under the Faculty of Engineering Science and Technology at the Norwegian University of Science and Technology in Trondheim. The work presented in this thesis is a result of 20 weeks work during the spring semester of 2016, corresponding to 30 credits.

This master thesis is initiated by the Department of Structural Engineering at NTNU, and is a contribution to research regarding the dynamic properties of tall timber buildings. The work was split into three main parts; measurement preparations, performing measurements and evaluating results. A lot of time was spent in the initial phase learning how the data acquisition hardware and software worked, with special weight on LabVIEW programming. After measurement data was acquired, a lot of time was spent on understanding the fundamentals of *Operational Modal Analysis* and utilizing *Covariance-Driven Stochastic Subspace Identification* to extract modal parameters from the measured data.

We are very grateful for the support from supervisor Kjell Arne Malo and associate professor Ole Øiseth, both at the Department of Structural Engineering, NTNU.

We would also like to thank PhD-candidates Knut Andreas Kvåle and Gunnstein Frøseth for being helpful throughout the process, and Knut Andreas Kvåle for providing some of the necessary MatLab scripts.

Finally we give our thanks to Bjørn Strickert Schjølberg and the rest of the Lab Engineers at the Department of Structural Engineering for technical help with the equipment.

Trondheim, 10th of June, 2016


Magnus Fjeld Olsen


Ola Hansen

Abstract

The main goal behind this thesis is to evaluate the dynamic properties of the worlds tallest timber building, *Treet*, in Bergen. The dynamic properties will be extracted from recorded acceleration time series. Measurements will also be acquired and evaluated for *Moholt 50/50*, a new student housing project initiated by Studentsamskipnaden i Trondheim.

Acceleration measurements are performed using accelerometers from Kistler, PCB Piezotronics, and data acquisition hardware from National Instruments. The acceleration data is then processed using a method called *Covariance-Driven Stochastic Subspace Identification*. From this method the natural frequencies, mode shapes and damping ratios are extracted. These parameters are then compared to the results from numerical models and engineering assumptions that were made during the planning of the respective buildings. An evaluation of the maximum accelerations and displacements is also performed. Finally, a numerical model of Moholt 50|50 is created in Abaqus/CAE in order to investigate how a numerical model for this type of structure predicts dynamic behaviour.

Results obtained from the measurements show that the engineers responsible for predicting the dynamic behaviour of Treet were satisfactory close to actual properties, although the natural frequencies seem to be consistently higher due to non-structural effects. The measured dynamic properties at Moholt 50|50 were close to the natural frequencies and mode shapes predicted by the numerical model. However, it is unknown whether the responsible engineers predicted the same results. Also, the damping ratios at Moholt are highly uncertain due to the excitation system not coinciding well with the white noise assumption used for *Operational Modal Analysis*.

Sammendrag

Hovedmålet med denne oppgaven er å evaluere de dynamiske egenskapene til verdens høyeste trehus, *Treet*, i Bergen. Egenskapene vil bli hentet ut fra målte akselerasjoner i huset. Den samme prosedyren vil også brukes til å evaluere Moholt 50|50, det nye studentboligprosjektet til Studentsamskipnaden i Trondheim.

Akselerasjonsmålingene vil bli utført med akselerometere laget av Kistler og PCB Piezotronics og med datainnsamlingsutsyr fra National Instruments. Akselerasjonsdata vil deretter bli behandlet ved å bruke en metode som kalles *Covariance-Driven Stochastic Subspace Identification*. Fra denne metoden vil egenfrekvensene, modformene og modal dempning bli identifisert. Disse parametrene vil deretter bli sammenlignet med resultatene fra numeriske modeller og antakelser gjort under prosjekteringen av de respektive byggene. I tillegg vil en vurdering av maksimale akselerasjoner og forskyvninger bli utført. Til slutt vil en numerisk modell av Moholt 50|50 bli laget i Abaqus / CAE som et sammenligningsgrunnlag for resultatene.

Resultatene fra målingene viser at ingeniørene bak Treet var tilfredsstillende nær de faktiske dynamiske egenskapene i prosjekteringen, selv om de naturlige frekvensene ser ut til å være konsekvent høyere på grunn av effekter fra ikke-strukturelle elementer. De målte dynamiske egenskapene til Moholt 50|50 var nære egenfrekvensene og modformene til den numeriske modellen. Det er imidlertid ukjent om ingeniørene bak Moholt 50|50 fikk samme resultat i prosjekteringen. Dessverre er ikke resultatene fra Moholt gode nok til å gi sikre estimater på modal dempning i husene siden lasten ikke passer godt med antakelsen om hvit støy gjort for *Operational Modal Analysis*.

Contents

Preface	v
Abstract	vi
Sammendrag	viii
List of Abbreviations	xxii
1 Introduction	1
1.1 Background	1
1.2 Scope of present work	2
1.3 Case One: Moholt 50 50	2
1.4 Case Two: Treet	3
2 Timber Structures	5
2.1 Timber as a construction material	5
2.1.1 Glued Laminated Timber	6
2.1.2 Cross Laminated Timber	7
2.2 Tall timber buildings	7
2.3 Dynamic properties	8
3 Theory	9
3.1 Structural Dynamics	9
3.2 Time Domain	10
3.3 State-Space Model	11
3.4 Complex Mode Shapes	13
3.4.1 Argand Diagram	14
3.5 Frequency Domain	15
3.5.1 Fourier Transform	15
3.5.2 Auto Power Spectral Density	16
3.5.3 Cross Power Spectral Density	16
3.5.4 Welch's Estimate	17
3.6 Operational Modal Analysis	20
3.6.1 The white noise input assumption	20
3.7 Discrete State-Space Model	22
3.8 Covariance-Driven Stochastic Subspace Identification	25
3.8.1 User inputs for Cov-SSI	25

CONTENTS

3.8.2	Initial data handling	25
3.8.3	Identifying the state matrices \mathbb{C} , \mathbb{G} and \mathbb{A}	27
3.8.4	Extracting Modal Parameters	28
3.8.5	Summary of Cov-SSI	29
3.9	Stabilization Diagram	30
4	Measurement Methods	33
4.1	Hardware	34
4.2	Software	36
4.3	Software and hardware communication	36
4.4	Configuring the CompactRIO	37
4.4.1	Scan Engine	37
4.4.2	FPGA	38
4.4.3	Expansion Chassis	39
4.5	LabVIEW programming	39
4.5.1	Gathering Data	40
4.5.2	Creating and saving files	40
4.5.3	Run programs at startup	40
4.5.4	First-In First-Out mechanisms	41
4.5.5	Filtering and downsampling	41
4.5.6	Aliasing	42
5	Numerical model of Moholt 50 50	45
5.1	Materials	46
5.2	Elements	47
5.3	Assembly	47
5.4	Results	48
5.4.1	Mode 1	49
5.4.2	Mode 2	50
5.4.3	Mode 3	51
5.5	Accelerations and the Serviceability Limit State (SLS)	52
5.6	Discussion regarding accuracy of model	52
6	Measurements	55
6.1	LabVIEW Preparations	55
6.1.1	Bergen Day 1 and Moholt One	55
6.1.2	Bergen Day 2 and Moholt Two	56
6.2	Layouts	57
6.2.1	Moholt	57
6.2.2	Bergen	58
6.3	Measurement Conditions	59
6.3.1	Moholt One	60
6.3.2	Moholt Two	60

6.3.3	Bergen Day 1	60
6.3.4	Bergen Day 2	60
6.4	Evaluating accuracy	61
7	Results	63
7.1	Moholt	65
7.1.1	Stabilization Diagram	65
7.1.2	Auto Power Spectral Densities	66
7.1.3	Natural Frequencies	67
7.1.4	Damping	67
7.1.5	Mode shapes	68
7.1.6	Maximum acceleration and displacements	68
7.2	Bergen	70
7.2.1	Stabilization Diagram	70
7.2.2	Auto Power Spectral Densities	70
7.2.3	Natural Frequencies	71
7.2.4	Damping	71
7.2.5	Mode shapes	72
7.2.6	Maximum acceleration and displacements	72
8	Discussion	73
8.1	Moholt 50 50	73
8.1.1	Natural Frequencies	74
8.1.2	Mode shapes	74
8.1.3	Damping	75
8.2	Treet	76
8.2.1	Natural Frequencies	77
8.2.2	Mode shapes	78
8.2.3	Damping	79
8.3	Uncertainties	80
9	Conclusions	81
9.1	Further Work	81
A	Moholt 50 50	87
A.1	System Layouts	87
A.1.1	Moholt One System Layout Specifics	89
A.1.2	Moholt Two System Layout Specifics	90
A.2	Moholt One Results	92
A.2.1	Method 1 - Results	92
A.2.2	Method 2 - Results	96
A.3	Moholt Two Results	104
A.3.1	Excitation Method 1	104

CONTENTS

A.3.2	Excitation Method 2, Activity on Construction Site	108
A.3.3	Excitation Method 2, Without Construction Activity on Site . .	115
B	Treet	125
B.1	System Layouts	126
B.1.1	Day 1	126
B.1.2	Day 2, FPGA	127
B.1.3	Day 2, Scan mode	127
B.2	Results	128
B.2.1	Day 1	130
B.2.2	Day 2, Scan Mode Results	137
B.2.3	Day 2, FPGA Results	145
C	Evaluation of Time Series	155
C.1	Moholt One, Method 2	155
C.2	Bergen Day 1	156
C.3	Bergen Day 2, Scan Mode	158
C.4	Bergen Day 2, FPGA	159
C.5	Evaluation of Max. Acc. and Max. Dyn. Displ. Estimates	160
D	Hardware	163
D.1	Accelerometer Power Inputs and Outputs	163
D.2	Cables	163
E	Digital Appendix	165
E.1	Memory stick	165

List of Figures

- 1 Introduction**
- 1.1 Moholt 50|50 2
- 1.2 Treet on the first day 3

- 2 Timber Structures**
- 2.1 Glulam Connection 6
- 2.2 Cross laminated timber 7
- 2.3 Comparison between Treet and Burj Khalifa 8

- 3 Theory**
- 3.1 Complex plots of 2DOF system mode shapes 14
- 3.2 Power spectra of periodic and non-periodic expansions 18
- 3.3 Hanning window applied to a non-periodic sement 19
- 3.4 Combined System 21
- 3.5 Stabilization Diagram example 31

- 4 Measurement Methods**
- 4.1 CompactRIO 33
- 4.2 Kistler accelerometer 35
- 4.3 Channel inputs in Scan Mode 37
- 4.4 VI on FPGA target 38
- 4.5 Labview project with cRIO and modules 39
- 4.6 Creation of a TDMS file with 2D array data 40
- 4.7 RT FIFO structure 41
- 4.8 Continuous Lowpass Butterworth filter 41
- 4.9 Downsampling 42
- 4.10 Aliasing in the time domain, [35] 42
- 4.11 Effects of aliasing for filtered and unfiltered signal 43

LIST OF FIGURES

5	Numerical model of Moholt 50 50	
5.1	One story of Moholt 50 50	45
5.2	120mm CLT at Moholt 50 50	46
5.3	Assembly of Moholt 50 50	47
5.4	Mode 1	49
5.5	Mode 2	50
5.6	Mode 3	51
6	Measurements	
6.1	Continuous Butterworth Lowpass Filter with downsampling	56
6.2	FPGA host VI	56
6.3	System layout of Moholt 50 50	58
6.4	Coordinate system used to present the results from Treet	59
7	Results	
7.1	Chosen values for one mode	64
7.2	Stabilization diagram from Moholt Two	65
7.3	APSD plots from Moholt Two	66
7.4	Stabilization Diagram of data obtained using FPGA	70
7.5	APSD of all channels using FPGA on Day 2 in Bergen	71
7.6	Modes shapes of Treet	72
8	Discussion	
8.1	Natural Frequencies of Numerical Model and from Measurements	74
8.2	Damping estimates without construction activity	75
8.3	Natural Frequencies of Numerical Models and from Measurements	77
8.4	Measured Natural Frequencies	78
8.5	Damping ratios of Treet from measurements	79
9	Conclusions	
9.1	Proposed 300 meters tall timber skyscraper	82
A	Moholt 50 50	
A.1	Moholt 50 50 Layout	88
A.2	Position and direction of each vector entry in the detected mode shapes in the global coordinate system	90
A.3	Two first two hours of overnight recording during Moholt Two	91
A.4	Position and direction of each vector entry in the detected mode shapes in the global coordinate system	92
A.5	Acceleration time series of the Kistler accelerometers	93

LIST OF FIGURES

A.6	Acceleration time series of the PCB accelerometers	94
A.7	Displacement time series of the Kistler accelerometers	94
A.8	Displacement time series of the PCB accelerometers	95
A.9	APSD Moholt One	95
A.10	Peaks considered non-physical with respect to structural behaviour. . .	96
A.11	Scatter of Damping Estimates	98
A.12	Mode 1	99
A.13	Mode 2	99
A.14	Mode 3	100
A.15	Auto Power Spectral Density of channel 1 and 2	100
A.16	Acceleration time series of the Kistler accelerometer	102
A.17	Acceleration time series of the PCB accelerometers	102
A.18	Dynamic displacement time series of the Kistler accelerometers	103
A.19	Dynamic displacement time series of the PCB accelerometers	103
A.20	APSDs for Moholt Two, Method 1	104
A.21	Peak acceleration time series of Moholt Two, Method 1	106
A.22	Peak dynamic displacement time series of Moholt Two, Method 1	107
A.23	Scatter of Damping Estimates from Moholt Two, Method 2 with Construction Activity	109
A.24	Argand Diagram of Mode 1	110
A.25	Argand Diagram of Mode 2	111
A.26	Argand Diagram of Mode 3	111
A.27	Argand Diagram of Mode 4	112
A.28	APSD of each Channel from Moholt Two, Method 2 with Construction Activity	113
A.29	Stabilization diagram from Moholt Two, Method 2 with Construction Activity	113
A.30	Acceleration time series in X-direction	114
A.31	Dynamic Displacement time series in Z-direction	115
A.32	Scatter of Damping Estimates from Moholt Two, Method 2 without Construction Activity	117
A.33	Argand Diagram of Mode 1	118
A.34	Argand Diagram of Mode 2	119
A.35	Argand Diagram of Mode 4	119
A.36	Argand Diagram of Mode 5	120
A.37	APSDs of Channels 3 and 4	121
A.38	Stabilization Diagram of Moholt Two, Method 2 without Construction Work	122
A.39	Acceleration time series in Channel 3	123
A.40	Dynamic Displacement time series in Channel 2	123

B Treet

LIST OF FIGURES

B.1	Coordinate system used to present the results from Treet	126
B.2	Bending Mode in Z-direction	129
B.3	Bending Mode in X-direction	129
B.4	Torsional Mode	130
B.5	Scatter of Damping Estimates	131
B.6	Argand Diagram of Mode 1	132
B.7	Argand Diagram of Mode 2	133
B.8	Argand Diagram of Mode 2	133
B.9	APSD of all Channels	134
B.10	PCB time series in Channel 1	134
B.11	Stabilization diagram of Day 1	135
B.12	Acceleration time series of each channel during Day 1	136
B.13	Dynamic displacement time series of each channel during Day 1	137
B.14	Scatter of Damping Estimates	138
B.15	Argand Diagram of Mode 1	140
B.16	Argand Diagram of Mode 2	140
B.17	Argand Diagram of Mode 3	141
B.18	Argand Diagram of Mode 4	141
B.19	Argand Diagram of Mode 5	142
B.21	Stabilization diagram of data obtained using Scan Mode	143
B.22	Acceleration time series of each channel. Day 2, scan mode.	144
B.23	Dynamic Displacement time series of each channel. Day 2, scan mode.	145
B.24	Scatter of Damping Estimates	146
B.25	Argand Diagram of Mode 1	148
B.26	Argand Diagram of Mode 2	148
B.27	Argand Diagram of Mode 3	149
B.28	Argand Diagram of Mode 4	149
B.29	Argand Diagram of Mode 5	150
B.30	APSD of all channels	151
B.31	Stabilization diagram of data obtained using FPGA	151
B.32	Acceleration time series of each channel Day 2	152
B.33	Dynamic displacement time series of each channel Day 2	153
C.1	Comparison of detected frequency at different variation in δt	156
C.2	Value of Tick Count in micro seconds	158
C.3	Value of δt for every point being sent from the timed loop into the FIFO	158
C.4	Value of Tick Count in micro seconds	159
C.5	Value of δt for every 280th point being sent into the FIFO	159
C.6	Value of δt for every 280th point being sent into the FIFO	160

List of Tables

- 2 Timber Structures**
- 2.1 Strength comparison between concrete, steel and timber 6

- 5 Numerical model of Moholt 50|50**
- 5.1 Material properties of CLT. Elastic moduli are given in MPa. 46
- 5.2 Mode shapes and frequencies for mode 1 to 6 48
- 5.3 Estimated maximum accelerations at Moholt 50|50 52

- 7 Results**
- 7.1 Natural Frequencies of the detected modes at Moholt 50|50 67
- 7.2 Damping ratios from Moholt Two 67
- 7.3 Detected mode shapes at Moholt 50|50 68
- 7.4 Maximum accelerations and displacements of Moholt 50|50 with construction activity 68
- 7.6 Maximum accelerations and displacements from four people shaking Moholt 50|50 69
- 7.5 Maximum accelerations and displacements of Moholt 50|50 without construction activity 69
- 7.7 Natural Frequencies of the detected modes at Treet, using FPGA . . . 71
- 7.8 Damping Ratios from Treet, using FPGA 71
- 7.9 Relative lengths of each mode shape 72

- 8 Discussion**
- 8.1 Previously estimated and obtained natural frequencies and damping ratios 76

- 9 Conclusions**

- A Moholt 50|50**
- A.1 Relation between measurement files and local coordinate systems . . . 89

LIST OF TABLES

A.2	File names and inputs of Moholt Two	90
A.3	Relations between measurement files and local coordinate systems . . .	91
A.4	Max. Acc. and Max. Dyn. Displ. from Moholt One, Method 1	93
A.5	Limits on frequency and damping for Moholt One	97
A.6	Natural Frequencies detected during Moholt One	97
A.7	Damping ratios for Moholt One	97
A.8	Relative lengths of each eigenvector	98
A.9	Complex entries of each eigenvector	98
A.10	Peak accelerations of each channel during Moholt One, Method 2 . . .	101
A.11	Maximum detected peak acceleration and dynamic displacements . . .	105
A.12	Limits on frequency and damping for Moholt Two, Method 2 with Construction Activity	108
A.13	Natural Frequencies from Moholt Two, Method 2 with Construction Activity	108
A.14	Damping Ratios from Moholt Two, Method 2 with Construction Activity	108
A.15	Relative lengths of each mode shape entry	110
A.16	Complex representation of each Mode Shape	110
A.17	Max. Acc. and Max. Dyn. Displ. from Moholt Two, Method 2 with Construction Activity	114
A.18	Limits on frequency and damping for Moholt Two, Method 2 without Construction Activity	115
A.19	Natural Frequencies from Moholt Two, Method 2 without Construction Activity	116
A.20	Damping estimates from Moholt Two, Method 2 without Construction Activity	117
A.21	Max. Acc. and Max. Dyn. Displ. from Moholt Two, Method 2 without Construction Activity	122
B	Treet	
B.1	Relation between measurement files and local coordinate systems, Day 1	127
B.2	Relation between measurement files and local coordinate systems, Day 2, FPGA	127
B.3	Relation between measurement files and local coordinate systems, Day 2, scan mode	128
B.4	Limits on frequency and damping for Bergen Day 1	130
B.5	Natural Frequencies from Bergen Day 1	131
B.6	Damping Ratios from Bergen Day 1	131
B.7	Relative lengths of each eigenvector	132
B.8	Complex entries of each eigenvector	132
B.9	Max. Acc. and Max. Dyn. Displ. in all channels from Bergen Day 1 . .	135
B.10	Limits on frequency and damping for Bergen Day 2 using scan mode .	137
B.11	Detected Natural Frequencies using Scan Mode	138

LIST OF TABLES

B.12	Detected Natural Frequencies using Scan Mode	138
B.13	Lengths of each eigenvector entry	139
B.14	Complex eigenvector entries	139
B.15	Max. Acc. and Max. Dyn. Displ. from Bergen Day 2, scan mode . . .	143
B.16	Limits on frequency and damping for Bergen Day 2, FPGA	145
B.17	Natural Frequencies from Bergen Day 2, FPGA	146
B.18	Damping Ratios from Bergen Day 2, FPGA	146
B.19	Relative lengths of each eigenvector	147
B.20	Complex entries of each eigenvector	147
B.21	Max. Acc. and Max. Dyn. Displ. of each channel Bergen Day 2, FPGA	152
D.1	Accelerometer information	163
D.2	Cable Lengths	163

LIST OF TABLES

List of Abbreviations

AC Alternating Current

APSD Auto Power Spectral Density

bpm Beats Per Minute

Cov-SSI Covariance driven Stochastic Subspace Identification

CPSD Cross Power Spectral Density

cRIO Compact Reconfigurable Input/Output

DC Direct Current

FFT Fast Fourier Transform

FIFO First In, First Out

FPGA Field-Programmable Gate Array

IEPE Integrated Electronic PiezoElectric

Kistler Kistler accelerometer

NI National Instruments

OMA Operational Modal Analysis

PCB PCB Accelerometer

SID System Identification

SiT Studentersamskipnaden i Trondheim

VI Virtual Instrument

ZOH Zero Order Hold

LIST OF TABLES

Chapter 1

Introduction

In the world today, everything must evolve to become more environmentally friendly as the problems of climate change increases [26]. Therefore, alternatives to the conventional materials in high-rise buildings must be considered. Usually, high-rise buildings are built of steel and concrete, while timber is mostly used in low-rise residential buildings. However, manufacturing of steel and concrete has a high carbon footprint and replacing those materials with timber will have a large positive effect on the CO₂-emissions during the entire life-cycle of a building [13].

1.1 Background

There are several reasons why timber is rarely used for high-rise buildings. First of all, there are only a handful really tall timber structures in the world. Therefore, little empirical data exist to support the numerical models predicting structural behaviour. This makes building tall with timber a risky investment and makes it harder to do research. Therefore, only limited data is available regarding the dynamic properties of timber as a construction material. A lot of the engineering design is done by making assumptions and qualified guesses [25]. In order to achieve a better understanding of those properties, a combination of numerical models and actual buildings need to be researched [45].

Previously, research regarding the feasibility of timber residential buildings has revealed issues concerning accelerations at the top floors [45, 24]. This is a problem that needs to be solved if taller timber residential buildings are going to become a reality.

1.2 Scope of present work

In this master thesis the experimental work will be measurements of accelerations on two types of tall timber buildings in Norway, *Moholt 50|50* in Trondheim and *Treet* in Bergen. The measurement data will then be processed in Matlab to extract the dynamic properties of the buildings. Two numerical models of *Treet* already exist [16, 24], while another model of *Moholt 50|50* has been created as a part of this thesis. They will all be used as reference when discussing results from the analyses of the measurement data, and the results from previous measurements. It will be emphasized how well the numerical models correspond to reality, as the accuracy of numerical models is very important when considering the feasibility of new concepts. More accurate models may also increase the willingness by investors to initiate construction of new conceptual timber buildings as well as large scale projects using timber.

The dynamic properties that will be extracted include natural frequencies, mode shapes and damping ratios. The extracted modal parameters may be used by engineers to better predict the behaviour of different structural timber elements and systems.

Obtaining quality measurements can be challenging, and a big part of this thesis involves setting up the equipment and software needed to overcome these challenges. In the report, the process of obtaining quality data will be explained shortly. A full explanation is included in the digital Appendix.

1.3 Case One: Moholt 50|50

The first structures that will be investigated are the new student housing towers at Moholt. The main reason for investigating Moholt 50|50 is to learn how different types of timber structures behave dynamically. A part of the reason for performing the first measurements is to achieve a better understanding of how the equipment works and how relevant data can be extracted. The towers at Moholt 50|50 are 9 storeys tall, where the ground floor is made out of concrete and the entire structural system in the upper floors are made out of Cross Laminated Timber (CLT) [41].



Figure 1.1: Moholt 50|50

Moholt 50|50 is built by Veidekke as the main contractor for Studentsamskipnaden i Trondheim (SiT). The architects are MDH and Arne Henriksen arkitekter, and the engineering of the structural system was performed by Høyer Finseth in collaboration with an Austrian company. The residential towers will be finished by the end of summer this year (2016).

1.4 Case Two: Treet

The second building that will be investigated is the residential building Treet. It was finished on the 9th of December 2015 in Damsgårdssundet, Bergen. It is, as of now, the tallest timber building in the world [44]. It is 14 stories tall and has a total height of 51 meters. The residential building was commissioned by Bergen og Omegn Boligbyggelag (BOB). The project was a collaboration between BOB, the architects Artec, the consulting engineers at SWECO, producers of building modules Kodumanja from Estonia, and the Norwegian timber-processing group Moelven.



Figure 1.2: Treet on the first day

The residential apartments of the building are prefabricated modules placed inside a substructure, and they are stacked upon each other in stacks of four [24, 45]. The substructure consists of an external truss system made of Glued Laminated Timber (glulam). The fifth and ninth floors are so-called power stories that strengthens the structure and are connected directly to the residential modules on those stories. On top of the power stories, there are concrete slabs that support the next stack of four residential modules [24].

Previously, a team of researchers from the University of Cambridge in England have measured vibrations of Treet [37]. The measurements were performed during the last phase of construction on a day with almost no wind [25]. However, they were able to get some results that will be a part of the discussion.

1 INTRODUCTION

Chapter 2

Timber Structures

Timber buildings have been around for thousands of years, and have been relatively affordable for most people. Timber is easy to use, as both whole logs and simple planks can be used as construction materials. Furthermore, durable connections can be made quite easily and the low weight makes it possible to build nearly everywhere [23, 48]. However, the structures that can be built with traditional timber products are limited. The invention of Glued Laminated Timber and Cross Laminated Timber has provided an opportunity for larger structures to be made out of timber.

2.1 Timber as a construction material

Timber is composed of fibres of cellulose held together by lignin, and the fibres are usually aligned with the lengthwise direction of the tree or branch. Thus, it is a natural composite. The strength in the direction parallel to the fibres is larger than the strength orthogonal to the fibres. Therefore, timber is an orthotropic material [32].

The elastic modulus of timber is significantly lower compared to concrete and steel. However, timber has a much lower density than both concrete and steel. Therefore, the specific strength, which is defined as the Young's Modulus divided by the density, is higher than for concrete and steel. In table 2.1 a comparison between ordinary construction steel (S355), ordinary concrete (B35) and timber along the fibre direction (strength grade C24) is illustrated [32].

2 TIMBER STRUCTURES

Material	Density (kg/m^3)	Young's Modulus (MPa)	Specific strength
Concrete	2500	35000	14
Steel	7800	210000	27
Timber	350	11000	31

Table 2.1: Strength comparison between concrete, steel and timber

It can be seen from the figure that the stiffness of the timber is 30% of the stiffness of the concrete and only 5% of the stiffness of steel. However, the specific strength is much higher for timber than concrete, and a bit higher than the specific strength of steel.

2.1.1 Glued Laminated Timber

Glued Laminated Timber is a product composed by layers of laminations glued together and compressed. This makes it a highly versatile product, as it can be formed into many different shapes and sizes. Both curved beams and beams with varying cross-section can be made without too much work or waste [27].



Figure 2.1: Glulam Connection

Glulam beams can be made with the same or varying strength in each lamination over the cross-section. In addition to the strength grade of the timber, the strength of glulam products is also determined by the strength of the glue. The modulus of elasticity can be between 8400 and 14200 MPa, and the density is between 370 and 490 kg/m^3 [27, 31].

2.1.2 Cross Laminated Timber

Cross Laminated Timber is made in nearly the same way as glulam, except that that the laminations are placed orthogonal to each other. This gives high strength in two directions, but the highest one-directional strength will not be the same as for glulam. This makes CLT highly effective for walls and floors, while glulam is more effective as beams [10].



Figure 2.2: Cross laminated timber

CLT panels can be made, with the same or varying strength grade in the laminations. Strength is a result of the timber and glue used, and the panels may be equally strong in both directions or have different strength in each direction. The strength in the different directions will also vary with the amount of laminations in each direction. CLT elements are usually built up by 5 or 7 laminations, but the number can vary from 3 to 9 [42].

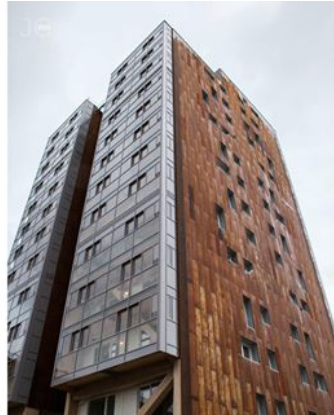
2.2 Tall timber buildings

If the height of the tallest timber buildings is compared to the height of the tallest concrete and steel buildings, the height of the timber buildings is vanishingly small. The tallest building in the world is the Burj Khalifa with its 828m [47]. That is about 16 times taller than Treet, which only has a height of 51 meters.

For timber buildings, the issues related to high-rise buildings become significant for

2 TIMBER STRUCTURES

much lower heights. This makes constructing tall structures with timber more complicated compared to other more conventional materials. A dynamic problem that might occur is large accelerations in the top floors. Acceleration is not a problem of stability or Ultimate Limit State (ULS), but rather a problem of comfort or Servicability Limit State (SLS) [45, 24].



(a) Treet



(b) Burj Khalifa

Figure 2.3: Comparison between Treet and Burj Khalifa

2.3 Dynamic properties

The acceleration problem in timber buildings occurs because of the inherent low mass of wood. The low stiffness to mass ratio of timber will make it easier to overcome static problems. When a structure is set in motion by time-variant forces, such as wind loads, one type of counteracting forces are the inertia forces. Due to the low mass of timber, the inertia forces are relatively small. However, the dynamic problems might be somewhat reduced with high damping. The damping of tall timber buildings is unfortunately highly uncertain and it would not be conservative to assume high damping. Hopefully, this is one of the properties of timber that this thesis might help to uncover.

Chapter 3

Theory

In this thesis, only linear structural dynamics is considered, and it is assumed that the reader has basic knowledge on the topic. Important relationships, equations and assumptions relevant to the theoretical background of the thesis will be stated. It is also assumed that the reader has basic knowledge about statistics.

3.1 Structural Dynamics

Dynamic response of a structure happens generally when a structure experiences loading that varies over time. In practice, every structure exhibits dynamic behaviour. The distribution and intensities of most loads vary somewhat over time, hence the deformation of the structure varies as well. However, it is usually implied that structural dynamics deals with structures oscillating in space due to external loading varying over time.

In a dynamic problem, external forces are balanced by internal forces due to stiffness resisting displacement, damping forces, and inertial forces from mass experiencing acceleration. It is possible to set up a dynamic equation of equilibrium in both the time domain as well as the frequency domain. In linear structural dynamics, the structural response is often described by the response of several *vibration modes*. Each *mode* has a natural frequency, damping ratio and mode shape.

3.2 Time Domain

In the time domain, the dynamic equation of equilibrium for a multi degree of freedom (MDOF) system can be described by the following set of differential equations:

$$M\ddot{U}(t) + C\dot{U}(t) + KU(t) = P(t) \quad (3.1)$$

Where M, C, K, are the mass, damping and stiffness matrices, respectively. U and P denotes the variation of displacement and loading at time t at each DOF, respectively. $\dot{U}(t)$ are the velocities and $\ddot{U}(t)$ are the accelerations at each DOF.

This differential equation is assumed to have a solution on the form:

$$U(t) = qe^{\lambda t} \quad (3.2)$$

where q is the amplitude of each DOF.

Substituting equation (3.2) into (3.1) and assuming an unloaded system gives the characteristic equation:

$$(\lambda^2 M + \lambda C + K)q = 0 \quad (3.3)$$

Tall timber structures typically react to dynamic loading by an oscillating response. This happens when the system is underdamped. For most practical situations, one of the solutions to the differential equations is then a complex conjugate pair [22]:

$$\lambda_j = -\omega_n \xi \pm i\omega_n \sqrt{1 - \xi^2} \quad (3.4)$$

where ω_n is the natural frequency and ξ is the modal damping ratio of mode n.

The natural frequency, damped natural frequency and damping ratio may be extracted the following way:

$$\omega_n = |\lambda| \quad (3.5)$$

$$\omega_d = \text{Im}(\lambda) \quad (3.6)$$

$$\xi = -\frac{\text{Re}(\lambda)}{|\lambda|} \quad (3.7)$$

3.3. STATE-SPACE MODEL

The mode shapes are usually estimated under the assumption that the damping is zero. The solution to $U(t)$ becomes:

$$U(t) = qe^{i\omega t} \quad (3.8)$$

and the homogeneous part of the differential equation after dividing by the harmonic term may be written:

$$-\omega^2 M + K = 0 \quad (3.9)$$

where ω^2 is a diagonal matrix containing the natural frequencies of the structure. Equation (3.9) may be recognized as the eigenvalue problem:

$$(K - \omega_n^2 M)\phi_n = 0 \quad (3.10)$$

where the eigenvector ϕ_n is the mode shape with natural frequency ω_n .

If damping is not neglected, estimating mode shapes is no longer as straight forward. The eigenvalue problem is then a *second order eigenvalue problem* where both λ and λ^2 are present. Equation (3.1) may be written on a state-space formulation, where eigenvalues and eigenvectors in complex conjugate pairs are extracted by solving the eigenvalue problem of the so-called *state matrix*. The *observable part* of the system eigenvectors are then the complex mode shapes.

3.3 State-Space Model

A state-space model is used to transform a second order differential equation into two first order differential equations [?]. In structural dynamics, equation (3.1) is transformed into a state equation and an observation equation.

The state equation is found by factorizing $P(t)$ into the matrix \bar{B} describing the location of inputs and $p(t)$ describing their variation in time:

$$M\ddot{U}(t) + C\dot{U}(t) + KU(t) = \bar{B}p(t) \quad (3.11)$$

Next, the state vector is introduced:

$$s(t) = \begin{Bmatrix} U(t) \\ \dot{U}(t) \end{Bmatrix} = \begin{Bmatrix} qe^{\lambda t} \\ \lambda qe^{\lambda t} \end{Bmatrix} \quad (3.12)$$

3 THEORY

and its derivative:

$$\dot{s}(t) = \begin{Bmatrix} \dot{U}(t) \\ \ddot{U}(t) \end{Bmatrix} = \lambda s(t) \quad (3.13)$$

If equation (3.11) is pre-multiplied by M^{-1} , $s(t)$ is substituted for $U(t)$ and $\dot{U}(t)$ and everything but $\ddot{U}(t)$ is moved to the right hand side:

$$\ddot{U}(t) = \begin{bmatrix} -M^{-1}K & -M^{-1}C \end{bmatrix} s(t) + M^{-1}\bar{B}p(t) \quad (3.14)$$

Using the identity matrix I , $\dot{U}(t)$ may be written:

$$\dot{U}(t) = \begin{bmatrix} \mathbf{0} & I \end{bmatrix} s(t) \quad (3.15)$$

Substituting equation (3.15) and (3.14) into (3.13):

$$\dot{s}(t) = \begin{Bmatrix} \dot{U}(t) \\ \ddot{U}(t) \end{Bmatrix} = \underbrace{\begin{bmatrix} \mathbf{0} & I \\ -M^{-1}K & -M^{-1}C \end{bmatrix}}_{A_c - \text{state matrix}} s(t) + \underbrace{\begin{bmatrix} \mathbf{0} \\ M^{-1}\bar{B} \end{bmatrix}}_{B_c - \text{input influence matrix}} p(t) \quad (3.16)$$

And the state equation may be written on the form:

$$\dot{s}(t) = A_c s(t) + B_c p(t) \quad (3.17)$$

The observation equation describes the system response that can be observed. If the system acceleration, speed and displacements are measured at l locations, the observation equation is simply:

$$U_l(t) = C_a \ddot{U}(t) + C_v \dot{U}(t) + C_d U(t) \quad (3.18)$$

Where C_a , C_v and C_d are the matrices describing the sensor locations of accelerations, velocities and displacements, respectively. If equation (3.14) is substituted into (3.18):

$$U_l(t) = \begin{bmatrix} C_v & -C_a M^{-1}C \end{bmatrix} \dot{U}(t) + \begin{bmatrix} C_d & -C_a M^{-1}K \end{bmatrix} U(t) + C_a M^{-1}\bar{B}p(t) \quad (3.19)$$

Rewritten:

$$U_l(t) = \underbrace{\begin{bmatrix} C_d - C_a M^{-1} K & C_v - C_a M^{-1} C \end{bmatrix}}_{C_c} s(t) + \underbrace{C_a M^{-1} \bar{B}}_{D_c} p(t) \quad (3.20)$$

And the observation equation may be written on the following continuous-time format:

$$U(t) = C_c s(t) + D_c p(t) \quad (3.21)$$

where C_c is the *output influence matrix* and D_c is the *direct transmission matrix* [35].

3.4 Complex Mode Shapes

If equation (3.2) is substituted into equation (3.17), the forcing term is left out and the state equation is divided by the state vector on both sides, it can be written on the form:

$$A_c = \lambda \quad (3.22)$$

where λ is a $2N \times 2N$ diagonal matrix. If the structure is classically damped, λ contains N complex conjugated pairs [22]. Equation (3.22) may be recognized as the eigenvalue problem:

$$(A_c - \lambda)\Psi = 0 \quad (3.23)$$

where Ψ is a $2N \times 2N$ matrix containing the complex eigenvectors of the state matrix A_c . The physical mode shapes are buried in Ψ and are identified by pre-multiplying Ψ by the output influence matrix [36]:

$$\Phi = C_c \Psi \quad (3.24)$$

When the structure is classically damped, the mode shapes in Φ will appear in complex conjugate pairs.

3.4.1 Argand Diagram

An Argand Diagram is a plot displaying a complex number as a vector in the complex plane. A mode with N DOFs can be described as N vectors rotating counter-clockwise in the complex plane with an angular frequency ω_n corresponding to the natural frequency of mode n . The vector of DOF_j will have an initial position $a_j + ib_j$ in the Argand Diagram. Mode shapes extracted from the eigenvalue problem come out for an arbitrary time instant, meaning the placement in the Argand Diagram is for an arbitrary time instant. The lengths $\sqrt{a_j^2 + (b_j)^2}$ of each DOF is their maximum relative magnitudes when hitting the real axis. If two DOFs are on opposite sides (rotated 180°), they are in opposite phase and will hit the real axis at the same time. If different DOFs are neither in phase or in opposite phase, they will hit the real axis at different times. The mode shape is then *phase shifted*. Phase shifted mode shapes occur typically for structures that are non-classically damped, that is, when the equations of motion do not fully decouple [22].

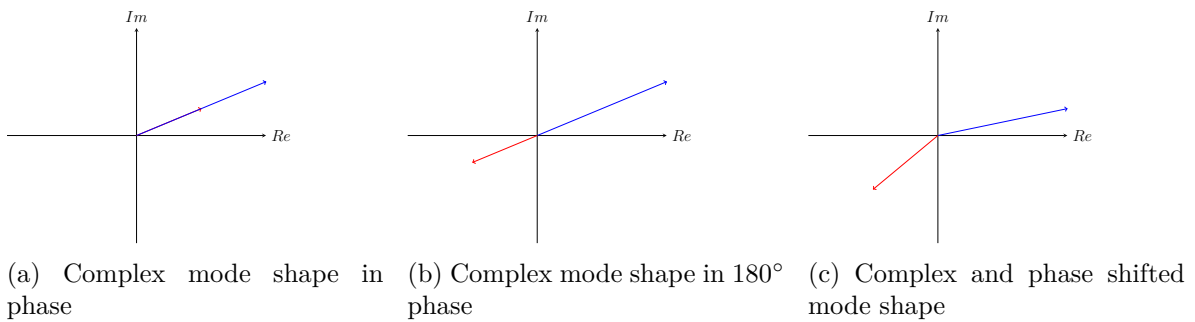


Figure 3.1: Complex plots of 2DOF system mode shapes

Adapted from Rönquist 2010 [39], modes that are phase shifted more than $\pm 10^\circ$ on the same or opposite side in the Argand Diagram are not considered distinct mode shapes.

3.5 Frequency Domain

If the fourier transform, explained in Subsection 3.5.1, is applied to both sides of equation (3.1), the dynamic equation of equilibrium becomes:

$$[-\omega^2 M + i\omega C + K]U(\omega) = P(\omega) \quad (3.25)$$

where $U(\omega)$ is the fourier transform of $U(t)$ and $P(\omega)$ is the fourier transform of $P(t)$. Further, the frequency response function (FRF) is introduced:

$$H(\omega)^{-1} = [-\omega^2 M + i\omega C + K] \quad (3.26)$$

Rearranging 3.25, it can be seen that the FRF represents the ratio between the response $U(\omega)$ and the input $P(\omega)$.

$$H(\omega) = \frac{U(\omega)}{P(\omega)} \quad (3.27)$$

3.5.1 Fourier Transform

A signal $U(t)$ in the time domain can be described as a sum of harmonic components. The fourier transform is used to extract the phase and amplitude of each component at its own frequency. The fourier transform is given by [21]:

$$X(\omega) = \mathfrak{F}(U(t)) = \frac{1}{2\pi} \int_{-\infty}^{\infty} U(t)e^{-i\omega t} dt \quad (3.28)$$

The transform is linear and works both ways. The inverse fourier transform is given by:

$$U(t) = \mathfrak{F}^{-1}(X(\omega)) = \int_{-\infty}^{\infty} X(\omega)e^{i\omega t} d\omega \quad (3.29)$$

In the real world, a time signal is never of infinite length, but is rather a discrete set of points at different amplitudes along the time axis. Therefore, a discrete fourier transform (DFT) can be utilized [46]:

$$X_k = \sum_{k=0}^{N-1} U_k e^{-2\pi i \frac{k}{N}} \quad (3.30)$$

3 THEORY

This operation requires N operations for every harmonic component $k = 0, 1, \dots, N - 1$, resulting in N^2 operations. For more efficient calculations, a family of computer algorithms called *fast fourier transforms* (FFT) are introduced. The resulting number of operations is reduced to $N \log(N)$ operations [21].

3.5.2 Auto Power Spectral Density

Subsections 3.5.2 and 3.5.3 are adapted from Strømme, 2010 [43]. When transforming a signal to the frequency domain, each frequency component $X_k(\omega)$ is usually complex valued. An easy way to determine how important a frequency component is to the entire signal in the time domain, is to take the auto power spectral density (APSD) $S(\omega)_{XX}$ of the signal:

$$S(\omega)_{XX} = \sum_{k=0}^{N-1} S(\omega_k)_{X_k X_k} \quad (3.31)$$

where:

$$S(\omega_k)_{X_k X_k} = \frac{E[X_k]E[X_k]}{\Delta\omega} = \frac{\sigma_{X_k, X_k}^2}{\Delta\omega} \quad (3.32)$$

and the variance of the signal is:

$$\sigma_{XX}^2 = \sum_{k=0}^{N-1} S(\omega)_{XX} \Delta\omega \quad (3.33)$$

3.5.3 Cross Power Spectral Density

The cross power spectral density (CPSD) $S(\omega)_{XY}$ is a representation of the covariance between two time signals X and Y:

$$S(\omega)_{XY} = \sum_{k=0}^{N-1} S(\omega_k)_{X_k Y_k} \quad (3.34)$$

where:

$$S(\omega_k)_{X_k Y_k} = \frac{E[X_k]E[Y_k]}{\Delta\omega} = \frac{\sigma_{X_k, Y_k}^2}{\Delta\omega} \quad (3.35)$$

and the covariance between the two signals is:

$$\sigma_{XY}^2 = \sum_{k=0}^{N-1} S(\omega)_{XY} \Delta\omega \quad (3.36)$$

It may be of interest to calculate spectral densities of signals with an introduced time lag of m time steps such that $\tau = m\Delta t$:

$$S(\omega, \tau)_{XY} = \sum_{k=0}^{N-1} S(\omega_k, \tau)_{X_k Y_k} \quad (3.37)$$

where:

$$S(\omega_k, \tau)_{X_k Y_k} = \frac{E[X_k(t)]E[Y_k(t + \tau)]}{\Delta\omega} = \frac{\sigma_{\tau, X_k, Y_k}^2}{\Delta\omega} \quad (3.38)$$

By setting $\tau = 0$, Equation (3.37) becomes the CPSD in Equation (3.34), and by setting both $\tau = 0$ and $X = Y$, Equation (3.37) becomes the APSD in Equation (3.31).

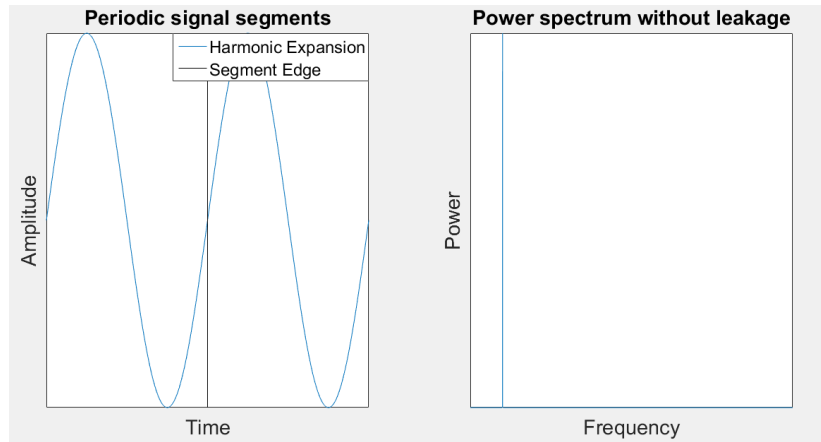
3.5.4 Welch's Estimate

When the power spectrum of a time series is calculated, it may contain a lot of noise. Welch's estimate is a way to reduce the noise in the power spectrum. The method splits a signal into M segments of N samples and computes the power spectrum of each segment.

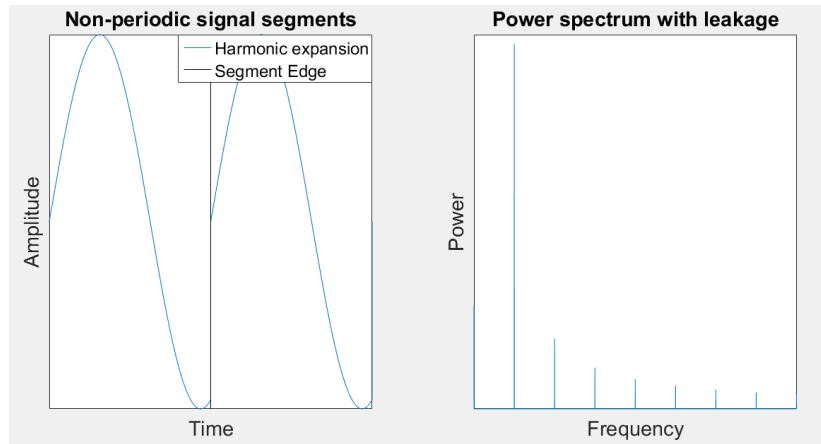
$$s_m = \frac{1}{N} U^*(\omega)^T U(\omega) \quad (3.39)$$

If the signal was continuous and periodic, the segments should be split between every period in order to avoid discontinuities that will be introduced by the Fourier transform when it attempts to periodically expand the segment. This is referred to as spectral leakage, and will simply generate other frequency components that are not really present in the signal. Figure 3.2 shows the consequences of a Fourier transform for a periodic and non-periodic expansion.

3 THEORY



(a) Exactly one signal period harmonically expanded and the corresponding power spectrum



(b) Less than one signal period harmonically expanded and the corresponding power spectrum

Figure 3.2: Power spectra of periodic and non-periodic expansions

The periodicity of a measured signal is hard to identify, both due to the unknown nature of the signal as well as measurement noise. By nature, a measured signal is non-periodic. When a segment is repeated, the harmonic expansion in the fourier transform becomes discontinuous. In order to reduce the consequences of discontinuities at the edges of a signal segment, windowing functions are introduced. Windowing functions are used to weigh a signal segment. They are typically zero at the edges and increase in value towards the middle. This is a simple remedy to make each segment become periodic.

$$U_w(t) = w(t)U(t) \tag{3.40}$$

Figure 3.3 shows how a *Hanning window* removes the discontinuity at the edges of the segment and makes the harmonic expansion periodic.

3.5. FREQUENCY DOMAIN

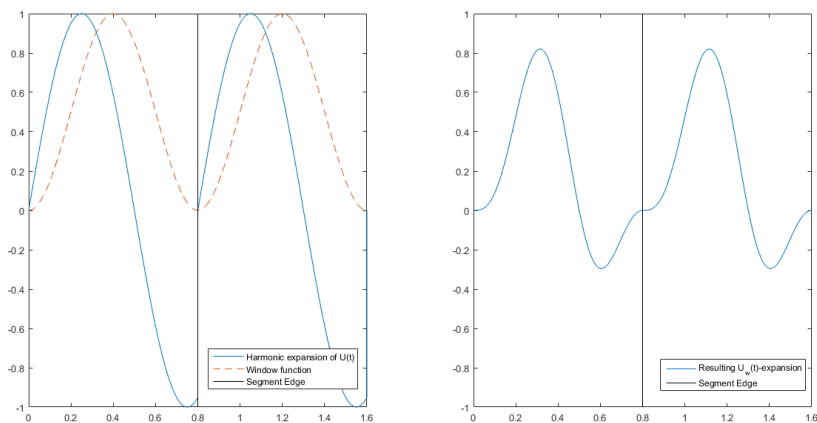


Figure 3.3: Hanning window applied to a non-periodic segment

Because of the low amplitudes at the edges of each windowed segment, the Fourier amplitudes will not be properly weighted by the signal amplitudes. Therefore, Welch's estimate introduces an overlap between segments such that more of the frequency content is conserved. The overlap allows the zeroed edges of one segment to contribute to the power spectrum of the next segment. The final power spectrum of the entire time series is the average of all the calculated power spectra of each segment.

3.6 Operational Modal Analysis

Operational Modal Analysis (OMA) is a group of techniques used to obtain the modal quantities of a system. A system transforms input, typically dynamic loading, to output, typically accelerations, velocities and displacements. When a system is known, it is possible to find output from input and vice versa. When the input and system is known, finding the output is called a forward problem. However, in practical situations, neither the exact characteristics of the input nor the system is known. OMA is a discipline that only uses output data for modal identification [35].

In order to properly identify the modal properties of a system, three assumptions need to be made:

- *System Linearity*: When a unique system input produces a system output (a forward problem), the same output will be able to work back the characteristics of the unique input. In other words, the system works both ways.
- *System Stationarity*: The dynamic properties of the system are constant, i.e. the mass, damping and stiffness matrices.
- *System Observability*: The only equipment used to identify all modal parameters are the sensors. They are only able to report what happens at each of their respective locations. Sensors must therefore be placed carefully to be able to pick up the modal information of interest. For example, the second mode of a simply supported beam will not be detected by a sensor layout of just one sensor placed at midspan.

3.6.1 The white noise input assumption

It is most common to use accelerometer recordings to identify the system characteristics. If the loading has its power evenly distributed over all frequencies, it is referred to as white noise input $N(\omega)$. $P(\omega)$ in equation 3.27 suggests that the output is a constant multiplied by the system $H(\omega)$, thus the structural system is automatically identified.

Inputs such as construction work, earthquakes or wind will not be white noise, but have different power at different frequencies. Therefore, the combined system is usually divided into an excitation system $H_e(\omega)$ and a structural system $H_s(\omega)$.

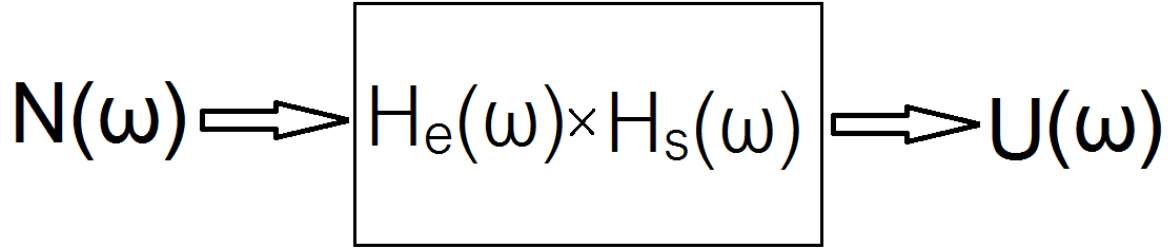


Figure 3.4: Combined System

The structural response is then assumed to come from white noise which is transformed to the input force $P(\omega)$ by $H_e(\omega)$ causing a structural response $U(\omega)$ when transformed by $H_s(\omega)$. Equation 3.27 may be rewritten as:

$$U(\omega) = N(\omega)H_e(\omega)H_s(\omega) \quad (3.41)$$

where:

$$P(\omega) = N(\omega)H_e(\omega) \quad (3.42)$$

and:

$$U(\omega) = P(\omega)H_s(\omega) \quad (3.43)$$

Measured data contains information about both the structural system as well as the excitation system. While the distinct frequency content of an input signal may vary throughout a time series, the structural system is assumed to have constant properties throughout a recording. The excitation system will therefore typically give more broad-banded contributions to the system Power Spectral Densities than the structural system. Therefore, $H_s(\omega)$ is distinguished from $H_e(\omega)$ by being more narrow banded in the frequency domain [35].

3.7 Discrete State-Space Model

The discrete state-space model can be used in OMA to extract dynamic properties of a structure through observations of acceleration. Measurements are obtained in discrete time, and the state-space model must therefore be converted to a discrete-time format. Time instant k may be represented by the sampling period δt such that:

$$t_k = k\delta t \quad (3.44)$$

The discrete state equations are:

$$s_{k+1} = \mathbb{A}s_k + \mathbb{B}p_k \quad (3.45)$$

and:

$$U_k = \mathbb{C}s_k + \mathbb{D}p_k \quad (3.46)$$

where equations (3.45) and (3.46) represent the discrete form of the state equation and observation equation, respectively.

Under the assumption that the input is constant over the period δt , generally referred to as Zero Order Hold (ZOH), it is possible to convert the state matrices in continuous-time to discrete-time through the following relations [35]:

$$\mathbb{A} = e^{A_c \Delta t} \quad (3.47a)$$

$$\mathbb{B} = (\mathbb{A} - I)A_c^{-1}B_c \quad (3.47b)$$

$$\mathbb{C} = C_c \quad (3.47c)$$

$$\mathbb{D} = D_c \quad (3.47d)$$

Where:

- \mathbb{A} : The discrete state matrix. It transforms a system from state s_k to state s_{k+1}
- \mathbb{B} : Input matrix from equation 3.17 on discrete form
- \mathbb{C} : The discrete output matrix. When multiplied with the state vector, it becomes the observable part of the system response.
- \mathbb{D} : The direct transmission matrix.

The ZOH assumption provides simple relations between continuous-time and discrete-time, and does not change C_c and D_c .

The discrete state-space model in equations (3.45) and (3.46) is a deterministic model, meaning the outcome is pre-determined and will always give the same output given the

3.7. DISCRETE STATE-SPACE MODEL

same input and initial conditions. In reality, both the input and output of a system will contain random disturbances. The system has a stochastic behaviour, and this is incorporated by introducing stochastic variables to the state-space model. Recording exactly the same oscillation two times will practically always give two different time series due to stochastic noise influencing the actual system output. Process noise w_k is added to the state equation, and takes disturbances and model inaccuracies into account. Measurement noise v_k is added to the observation equation, and takes measurement noise into account:

$$s_{k+1} = \mathbb{A}s_k + \mathbb{B}p_k + w_k \quad (3.48)$$

$$U_k = \mathbb{C}s_k + \mathbb{D}p_k + v_k \quad (3.49)$$

When performing OMA, the only available data are usually time series containing a lot of noise. The system input p_k is not known, and has to be baked into w_k and v_k . w_k and v_k are now the only processes causing system response, and this is described through a discrete-time stochastic state-space model:

$$s_{k+1} = \mathbb{A}s_k + w_k \quad (3.50)$$

$$U_k = \mathbb{C}s_k + v_k \quad (3.51)$$

The reason for deriving the *stochastic* state-space model in this thesis is to present the background for a group of techniques in OMA called *Stochastic Subspace Identification* (SSI). These techniques use large output time series, often accelerations \ddot{U} , and transforms the data into \mathbb{A} and \mathbb{C} . A very important assumption for the SSI techniques is that w and v are zero mean white noise stochastic processes. Under this assumption, their covariance matrices are:

$$E \left[\begin{array}{c} \left\{ w_p \right\}^T \\ \left\{ v_p \right\} \end{array} \quad \begin{array}{c} \left\{ w_q \right\} \\ \left\{ v_q \right\} \end{array} \right] = \begin{bmatrix} Q^{ww} & S^{wv} \\ (S^{wv})^T & R^{vv} \end{bmatrix} \quad (3.52)$$

when $p = q$ and

$\mathbf{0}$ when $p \neq q$

Where p and q denote two arbitrary time instants of w and v .

Under the assumption of w_k and v_k being white noise processes, U_k will also be a *zero mean Gaussian process* [35]. The covariance matrix of the output and the output shifted i time instants ahead is given by:

$$R_i = E \left[\begin{array}{cc} U_{k+i} & U_k^T \end{array} \right] \quad (3.53)$$

3 THEORY

And the covariance matrix of the state vector is given by:

$$\Sigma = E \left[\begin{array}{cc} s_k & s_k^T \end{array} \right] \quad (3.54)$$

The state vector is uncorrelated with the process and measurement noise:

$$E \left[\begin{array}{cc} s_k & w_k^T \end{array} \right] = \mathbf{0} \quad (3.55a)$$

$$E \left[\begin{array}{cc} s_k & v_k^T \end{array} \right] = \mathbf{0} \quad (3.55b)$$

The previous assumptions allow for a mathematical manipulation of equations (3.50) and (3.51) that leads to the following relations [35]:

$$\Sigma = \mathbb{A}\Sigma\mathbb{A}^T + Q^{ww} \quad (3.56)$$

$$R_{i=0} = \mathbb{C}\Sigma\mathbb{C}^T + R^{vv} \quad (3.57)$$

$$G = \mathbb{A}\Sigma\mathbb{C}^T + S^{rw} \quad (3.58)$$

$$R_i = \mathbb{C}\mathbb{A}^{i-1}G \quad (3.59)$$

where G is the covariance matrix of the state vector one time step ahead of the response vector:

$$G = E \left[\begin{array}{cc} s_{k+1} & U_k^T \end{array} \right] \quad (3.60)$$

In reality, they will not be white noise processes, but have some frequency components dominating more than others. This will occur as *poles* of \mathbb{A} alongside the eigenvalues of the system at hand.

3.8 Covariance-Driven Stochastic Subspace Identification

Covariance-Driven Stochastic Subspace Identification (Cov-SSI) attempts to identify the stochastic state-space model of a system from output-only data. The method uses correlation over different time lags within and between the measurement channels to produce different estimates of \mathbb{A} , \mathbb{C} and G for the system at hand. The estimates for \mathbb{A} and \mathbb{C} are used to extract modal parameters [36].

3.8.1 User inputs for Cov-SSI

One of the user inputs is the output data matrix Y . It contains every output value for each channel along the time axis. If there are l channels, and each channel contains N data points, the dimension of Y is $N * l$.

Another user input is the system order. A system of order n is only possible to identify if the observability and controllability matrices are of rank n . These matrices will be presented later in this section. The order of a system is in most practical cases unknown due to input and output noise, and is usually overestimated to ensure detection of all the structural modes buried within the output data. This overestimation causes the occurrence of mathematical poles alongside the poles related to the physical system. To distinguish between physical and non-physical poles, stabilization diagrams are used. They will be presented in Section 3.9.

The estimated system order n_{est} has to be larger than the system order n , or all the physical modes that should be present in the frequency band of the stabilization diagram will not be present. Increasing n_{est} greatly increases the computational time, and if n_{est} is too large, it becomes difficult to detect the system poles in between all the mathematical poles.

3.8.2 Initial data handling

First of all, the correlation matrices for a time lag j is calculated the following way:

$$R_j = \frac{1}{N-j} Y_{1:N-j}^T Y_{j:N} \quad (3.61)$$

where $Y_{1:N-j}$ is the data matrix with the j last rows removed, and $Y_{j:N}$ is the data matrix with the j first rows removed. Hence, R_j has dimensions $l * l$. Then, all the

3 THEORY

correlation matrices from a single step time lag up to i time lags are gathered into the block Toeplitz matrix:

$$T_{1|i} = \begin{bmatrix} R_i & R_{i-1} & \cdots & R_1 \\ R_{i+1} & R_i & \cdots & R_2 \\ \vdots & \vdots & \ddots & \vdots \\ R_{2i-1} & R_{2i-2} & \cdots & R_i \end{bmatrix} \quad (3.62)$$

And the one lag shifted Toeplitz matrix is:

$$T_{2|i+1} = \begin{bmatrix} R_{i+1} & R_i & \cdots & R_2 \\ R_{i+2} & R_{i+1} & \cdots & R_3 \\ \vdots & \vdots & \ddots & \vdots \\ R_{2i} & R_{2i-1} & \cdots & R_{i+1} \end{bmatrix} \quad (3.63)$$

There are $i * i$ correlation matrices, thus $T_{1|i}$ has dimensions $li * li$. For a successful identification of a system of order n , the Toeplitz matrix has to be $n * n$. Thus, the number of block rows i has to at least fulfil the criterion:

$$l * i \geq n \quad (3.64)$$

As the system order is usually unknown, a rough estimate of the system order could be the number of peaks in the APSD matrix within the relevant frequency band. The minimum number of block rows needed is then:

$$i_{min} = \frac{n_{est}}{l} \quad (3.65)$$

In real life applications, structures may have a complicated nature and the number of modes within a frequency band is not always known. The minimum number of block rows should be higher than equation (3.65) suggests. This will generally improve the results.

$$i_{min} = x \frac{n_{est}}{l} \quad (3.66)$$

The variable x should be chosen by the user, and what defines a suitable choice of x will depend upon the problem.

3.8. COVARIANCE-DRIVEN STOCHASTIC SUBSPACE IDENTIFICATION

3.8.3 Identifying the state matrices \mathbb{C} , \mathbb{G} and \mathbb{A}

Given the factorization in equation 3.59, the block Toepliz matrix may be factorized into the observability matrix O_i and the reversed controllability matrix Γ_i :

$$T_{1|i} = O_i \Gamma_i \quad (3.67)$$

where the observability matrix is given by:

$$O_i = \begin{bmatrix} \mathbb{C} \\ \mathbb{C}\mathbb{A} \\ \vdots \\ \mathbb{C}\mathbb{A}^{i-1} \end{bmatrix} \quad (3.68)$$

and the reversed controllability matrix is given by:

$$\Gamma_i = [\mathbb{A}^{i-1}G \quad \dots \quad \mathbb{A}G \quad G] \quad (3.69)$$

The observability matrix and reversed controllability matrix will have dimensions $(li) * n$ and $n * (li)$, respectively. From the factorization, the output influence matrix \mathbb{C} will be recognized in the l first rows of the observability matrix. The next state output covariance matrix G will be the l last columns in the reversed controllability matrix.

Next, the *Singular Value Decomposition* (SVD) of the block Toepliz matrix is calculated. It decomposes $T_{1|i}$ into the unitary matrices \mathbb{U} and \mathbb{V} and the diagonal matrix S . S holds the *importance*, or singular values, of each vector in \mathbb{U} and \mathbb{V} to the system arranged in descending order. It is further decomposed into S_1 holding the non-zero singular values and $S_2 = \mathbf{0}$ holding the zero singular values [35]:

$$T_{1|i} = \mathbb{U}S\mathbb{V}^T = \begin{bmatrix} U_1 & U_2 \end{bmatrix} \begin{bmatrix} S_1 & \mathbf{0} \\ \mathbf{0} & S_2 \end{bmatrix} \begin{bmatrix} V_1^T \\ V_2^T \end{bmatrix} \quad (3.70)$$

If the zero eigenvalues and corresponding singular vectors U_2 and V_2 are left out, the block Toepliz matrix may be written on the form:

$$T_{1|i} = O_i \Gamma_i = \mathbb{U}_1 S_1 \mathbb{V}_1^T \quad (3.71)$$

Using the identity matrix I , Equation (3.71) may be split into two parts to identify the observability and controllability matrices [35]:

$$O_i = \mathbb{U}_1 S_1^{1/2} I \quad (3.72)$$

$$\Gamma_i = I^{-1}S_1^{1/2}\mathbb{V}_1^T \quad (3.73)$$

I^{-1} has been used to indicate that this is just one of infinitely many options for a non-singular matrix that allows the separation of O_i and Γ_i up to a similarity transform [35].

Factorizing the one-lag shifted Toeplitz matrix using Equation (3.59):

$$T_{2|i+1} = O_i\mathbb{A}\Gamma_i \quad (3.74)$$

Substituting Equations (3.72) and (3.73) into (3.74) and solve for \mathbb{A} provides the $n * n$ state matrix from the measured data in Y :

$$\mathbb{A} = S_1^{-1/2}\mathbb{U}_1^T T_{2|i+1} \mathbb{V}_1 S_1^{-1/2} \quad (3.75)$$

3.8.4 Extracting Modal Parameters

Under the previous assumptions, the discrete state-space matrix \mathbb{A} and the output influence matrix \mathbb{C} are now known. They can be used to extract modal parameters from the identified state-space similar to what was done in Section 3.4.

Solving the eigenvalue problem for \mathbb{A} will identify the system eigenvectors Ψ and eigenvalues μ in the diagonal matrix \mathbb{M} .

$$\mathbb{A} = \Psi\mathbb{M}\Psi^{-1} \quad (3.76)$$

The physical mode shapes are obtained in a similar way to what was stated in Equation (3.24) by the following relation:

$$\Phi = \mathbb{C}\Psi \quad (3.77)$$

where $\mathbb{C} = C_c$ under the assumption of ZOH.

The natural frequency, damped natural frequency and modal damping ratio are obtained similarly to Equations (3.5) through (3.7). The state-space model used to identify the eigenvalues μ operates in discrete-time. In order to identify the modal parameters of each mode, the eigenvalues μ must be transformed to continuous-time. The connection between the state matrix in discrete- and continuous-time is given by Equation (3.47a). The eigenvalues in continuous-time become:

$$\lambda = \frac{\ln(\mu)}{\Delta t} \quad (3.78)$$

3.8. COVARIANCE-DRIVEN STOCHASTIC SUBSPACE IDENTIFICATION

For mode number m , the natural frequency, damped natural frequency and damping ratio are:

$$\omega_{n,m} = |\lambda_m| \tag{3.79}$$

$$\omega_{d,m} = \text{Im}(\lambda_m) \tag{3.80}$$

$$\xi_m = -\frac{\text{Re}(\lambda_m)}{|\lambda_m|} \tag{3.81}$$

Each λ_m is one system pole that comes from one version of \mathbb{A} created for a specific system order n . The process is further repeated for all system orders up to the maximum order defined by the user. Some of the estimates for λ_m will be related to the physical behaviour of the structure and some will be mathematical poles arising from the overestimation of the system order. In order to determine whether the eigenvalues describe physical dynamic properties of a structure or not, stabilization diagrams are used.

3.8.5 Summary of Cov-SSI

The process of performing a Cov-SSI analysis might be summarized in the following eight steps:

- Step 1 - Estimate system order. One way to do this is to just use a suitably large number for i in $n_{est} = i * l$. Alternatively, trace the number of peaks in the APSDs of the signal, and overestimate the system order with the user defined parameter x in Equation (3.66).
- Step 2 - Initial calculations: Establish the Toeplitz Matrix and the One Lag-shifted Toeplitz matrix
- Step 3 - Perform a singular value decomposition on the Toeplitz Matrix.
- Step 4 - Calculate SVD of the Toeplitz matrix.

Steps 5 through 8 can for efficiency be calculated for every second order $n = 2, 4, \dots, n_{est}$. This is because the eigenvalues and eigenvectors usually appear in complex conjugated pairs.

- Step 5 - Extract \mathbb{C} from O , and \mathbb{A} using Equation (3.75).
- Step 6 - Calculate eigenvalues and eigenvectors of each of the state matrix estimates \mathbb{A} .
- Step 7 - Convert the eigenvalues of \mathbb{A} into continuous-time eigenvalues.
- Step 8 - Extract modal parameters

3.9 Stabilization Diagram

A stabilization diagram plots information buried within the eigenvalues λ_m of \mathbb{A} . It is most common to extract the natural frequency of a pole through Equation (3.79) and report detected frequencies at different system orders. Since the system order is rarely known, it is usually overestimated. Measured data usually contains a lot of noise, the computation procedure will have numerical inaccuracies, and the model describing the system may not be accurate. Transforming measured data into a mathematical model will therefore not only produce poles that are connected to the physical properties of the system. It will also produce mathematical poles containing non-physical information. The mathematical poles tend to vary more than the physical poles over different system orders [35]. Stabilization criteria are introduced to separate mathematical poles from physical poles. They may for instance set requirements for the variation of frequency and damping from one order to the next:

$$\frac{|\omega(n) - \omega(n+1)|}{\omega(n)} < a \quad (3.82)$$

$$\frac{|\xi(n) - \xi(n+1)|}{\xi(n)} < b \quad (3.83)$$

where a and b are user defined criteria.

3.9. STABILIZATION DIAGRAM

Equation (3.82) is usually set to a strict criterion, as the estimates for natural frequencies tends to exhibit little variation at different orders. However, for lightly damped structures, the variation in damping estimates may be large when measured in percentage. Figure 3.5 below shows an example of black stable poles fulfilling the criteria $a = 1\%$ and $b = 5\%$ together with red unstable poles. The poles aligned in the dominant vertical lines are likely to represent physical modes of the system.

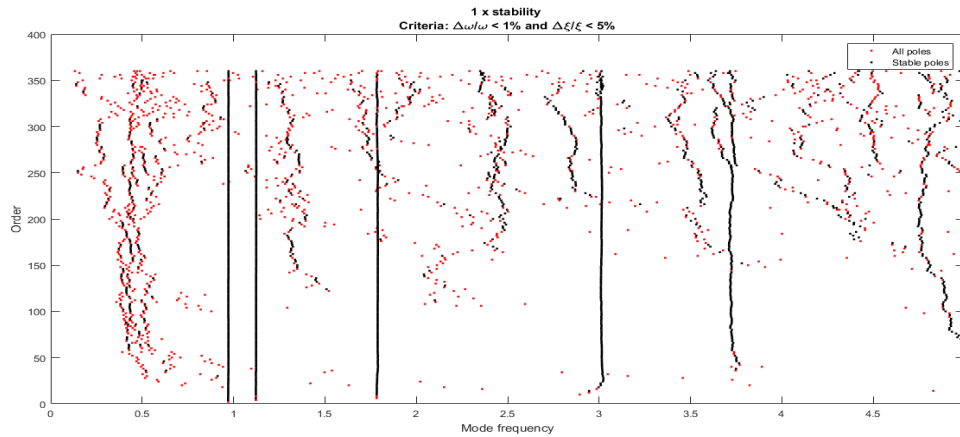


Figure 3.5: Stabilization Diagram example

3 THEORY

Chapter 4

Measurement Methods

The measurements performed at Moholt and in Bergen required accelerometers to be set up at relevant locations. No previous hardware or software set-up was available, so a lot of time was spent making the equipment ready for use. At the Department of Structural Engineering, there was an interest in learning how this type of equipment can be utilized for future projects. Preparing for measurements included installing software and learning LabVIEW programming, as well as configuring hardware.

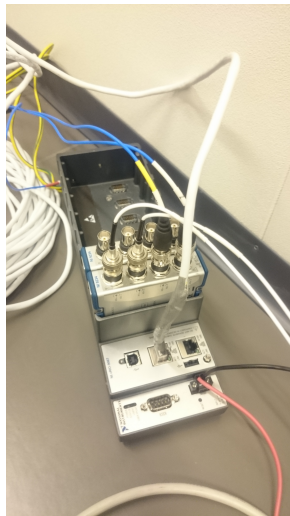


Figure 4.1: CompactRIO

4.1 Hardware

The following hardware was used to measure accelerations:

- NI 9067 CompactRIO Chassis (cRIO)
 - Kistler K-Beam Triaxial MEMS Capacitive AC Accelerometer, model 8395A2DOATTA00 (Kistler)
 - PCB Piezotronics accelerometer, model 356A16 (PCB)
 - NI 9234 dynamic signal acquisition module
 - Data and power cables
 - Coaxial extension cables
 - NI 9144 EtherCAT slave chassis
 - Ethernet cable
 - USB A to B cable
- Power supply set to 24V
- Computer with LabVIEW installed
- Special screws needed to mount the accelerometers to the structure.
- In addition some practical tools were needed; such as a drill, screwdrivers and tape.

The accelerometers were connected to the acquisition modules through coaxial cables specially made for minimizing noise. On both days at Moholt, coaxial extension cables were used as well [34], since only the cRIO chassis was available at the time. The acquisition modules were mounted directly to the chassis. The chassis and the Kistler accelerometers were both powered separately with a 24V power source[20, 29] while the modules and PCB accelerometers [33, 28] were powered through the chassis. The modules have four channels. Each channel is able to acquire data from one accelerometer in one direction. In order to communicate with the chassis, a computer connected by a USB cable was used. It is also possible to communicate either with an Ethernet cable or over the internet. Both communications were considered at some point, but they were found unnecessary for this thesis. In order to properly acquire the torsional mode shapes each accelerometer was placed as far away from the expected torsional centre as possible, on opposing sides.



Figure 4.2: Kistler accelerometer

The two types of accelerometers work in two different ways; the Kistlers oscillate around zero [20], while the PCBs starts to oscillate around a non-zero value [33]. The PCBs are after a couple of seconds automatically de-trended until they oscillate around zero. In post-processing of the data, the mean value was subtracted from each channel as a simple form of de-trending. The two types have different preferred frequencies where they exhibit optimal measurement accuracy; the Kistlers can sense acceleration successfully down to 0Hz, while the PCBs can only sense accurately down to 0.5Hz. This minimum value for the PCBs is a bit close to the 1Hz component expected from some of the measurements, and this may affect the amount of noise in the results. When the time series were watched during a recording, only noise could be seen with the naked eye, unless some local effect, like a door shutting nearby, caused a large spike in the amplitude.

The output from the accelerometers is in volts and therefore has to be converted into meters per second squared. The PCBs and the Kistlers have different constant scaling factors; the PCBs have a scaling factor of $98,1m/s^2/V$ [33] while the Kistlers have a scaling factor of $4,905m/s^2/V$ [20].

4.2 Software

For data acquisition, the software used to create *Virtual Instruments* (VIs) was LabVIEW 2015 made by National Instruments (NI). VIs are subroutines created in LabVIEW for controlling the data flow inside the cRIO. There is also a lot of different toolkits and functions that can be installed in LabVIEW that may be relevant for different applications. For acceleration measurements and signal processing, the most important software used is:

- Labview 32- or 64-bit (32-bit needed for FPGA)
- NI MAX
- Driver for CompactRIO-9067
- EtherCAT driver version corresponding to LabVIEW version

The included software is the minimum needed to make measurements with a cRIO and a slave chassis.

4.3 Software and hardware communication

How the different parts of the equipment communicate with each other is a highly important part of choosing the most accurate and efficient programming. Acceleration data is obtained when voltages are induced inside the accelerometers. This is an analog signal that is sent via a coaxial cable into the modules converting the analog signal into digital samples of data. This data is further processed by VIs on the Real-Time Target (the cRIO). A Real-Time Target is defined as having sufficient speed to run programs and acquire data in a way that is perceived as immediate. The processed data is then written to files on a local or external storage unit.

4.4 Configuring the CompactRIO

After installing the software and drivers for LabVIEW and cRIO, the cRIO target was imported into a LabVIEW project. At this point either *Scan Engine* or *FPGA* was chosen depending on the requirements for the VI in question. The Scan Engine and FPGA are two different ways of gathering and processing data.

4.4.1 Scan Engine

Scan Engine is the mode in which LabVIEW automatically uses a built-in function for side-stepping FPGA and it is possible to access the input and output modules directly in the VI. It can be set to an acquisition rate of up to 1kHz, and the modules are automatically timed and synchronized. Since the maximum acquisition rate is sufficiently higher than the relevant frequencies of structural dynamics, the scan engine is a suitable choice as long as aliasing effects (explained in Subsection 4.5.6) and sampling rates are under control. However, it is not certain what rate the modules convert the analogue signal into digital samples when using Scan Engine. This reduces controllability in regards to aliasing. One advantage of using Scan Engine, is that it utilizes the Real-Time processor on the Real-Time Target. Compiling VIs and controlling every data point becomes remarkably simple. For instance, it is easy to timestamp every single data point in order to keep track of the sampling rate.



Figure 4.3: Channel inputs in Scan Mode

During the two trips to Bergen, scan mode VIs were used to acquire data from 8 channels simultaneously. However, the VIs on the two different trips were very different. The first two VIs used a for loop to acquire an array of data. This for loop was supposed to run every millisecond and save all the data in the array every n^{th} iteration. On the second trip a VI using two separate loops was used; one timed loop synchronized to scan engine and one while loop. The timed loop was used to acquire data and send it through a FIFO (explained in Subsection 4.5.4) to the while loop which saved the data to disk. This method was chosen as it separates the two processes into two loops that can run at different speeds. This is highly recommended to avoid loss of data points [17].

4.4.2 FPGA

Field-Programmable Gate Array (FPGA) is, in the context of data acquisition using a cRIO, a silicon-chip inside the cRIO that is reprogrammable. It provides higher performance and stability than the Scan Engine, and is useful for rapid input/output processing. The maximum sampling rate can be up to 51.2kHz for the NI 9234 modules. Possible sampling rates for FPGA are given in Equation (4.1), and it can be seen that $n=31$ give the lowest possible sampling rate at approximately 1652Hz. FPGA is however more cumbersome and complicated than the Scan Engine and it is not possible to store data directly. In order to store data, the FPGA VI communicates via a FIFO to a VI on the Real-Time target. Although this makes the programming a bit more expensive and the compilation of the code takes typically several minutes, the end result is worth it as the FPGA produces a much more stable sampling rate and therefore also cleaner and more accurate results. In the FPGA VI, no solution on how to timestamp every data point was developed. Therefore, every 280th point was timestamped in the real-time host VI.

$$f_s = \frac{13.1072 * 10^6}{256 * n}, n = 1, 2, \dots, 31 \quad (4.1)$$

On the second trip to Bergen a simple form of FPGA programming was used to acquire data. This VI used a for loop within a while loop in FPGA, where the for loop included the FIFO which read the data channel by channel. The FPGA settings and module start-up was set before the while loop and then the data was acquired within the while loop. The sampling rate was set to 1652Hz. The reason behind setting it as low as possible was to make the output files more manageable. Also, the frequencies of interest is a lot lower than the sampling frequency so it does not affect the results. On the Real-Time target a while loop was used to extract the data from the FIFO and store it. Before the while loop, the FPGA target was specified and start-up commands were sent to the FPGA VI.

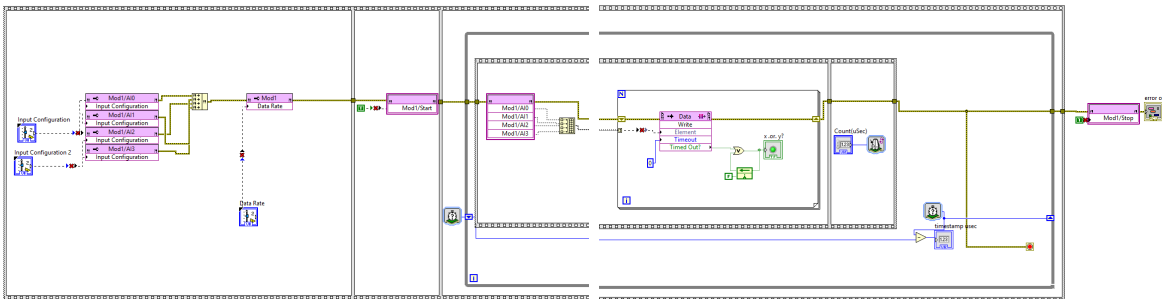


Figure 4.4: VI on FPGA target

4.4.3 Expansion Chassis

When evaluating the dynamic properties of the buildings, a set of accelerometers in different parts of the building was needed in order to acquire mode shapes. These accelerometers were set so far apart from each other that using coaxial extension cables would have been needed. This could possibly produce a lot of noise. It was therefore decided that a slave chassis should be used. The slave chassis was connected to the cRIO with an Ethernet cable. In the limited time available between the first and second trip to Bergen, no FPGA VI utilizing both the cRIO and the slave chassis was made. Therefore, the slave chassis was only used in scan mode [18].

4.5 LabVIEW programming

In this section, proposed methods for utilizing LabVIEW, in a number of different ways, are discussed. These methods are only proposed solutions that have been shown to work, but may not be the best solutions. The solutions are based upon the solutions proposed by NI [17].

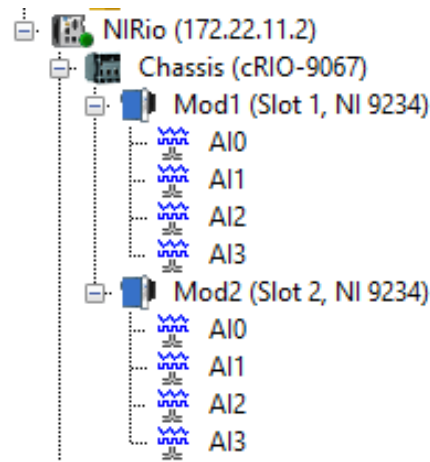


Figure 4.5: Labview project with cRIO and modules

When developing the programs, several forms of error detection have been used; indicators, waveform charts, and waveform graphs at strategic points. Most of these functions were removed in the final program however, as they may affect the performance.

4.5.1 Gathering Data

When the cRIO is connected in the right manner, some form of loop is needed to acquire more than one point of data. The loop that should be chosen depends on the form in which data is required to be collected. The most important thing to get right when acquiring data is to synchronize the different channels and have a controlled sampling. In scan mode, the synchronization was done automatically by the scan engine, while in FPGA the synchronization was done manually by starting all channels at the same time. Keeping track of the sampling rate was done by timestamping as many points as possible.

4.5.2 Creating and saving files

There are several ways to write data into files in LabVIEW. The way chosen is to use the tdms functions. Tdms is a binary file type that can either be opened in Excel or in Matlab. The tdms-format is the preferred format for instruments made by NI, as they have made it specifically for the purpose of data acquisition. Excel is limited in the number of datapoints it is able to open, a Matlab code was used for reading the data from the longer time series.

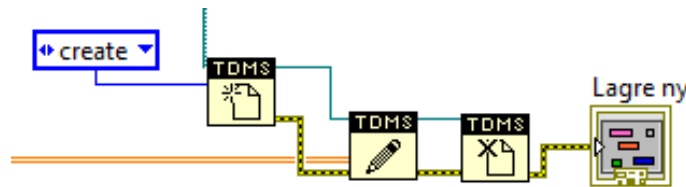


Figure 4.6: Creation of a TDMS file with 2D array data

4.5.3 Run programs at startup

For a VI to run independently of a computer, it has to start when the cRIO is turned on. This functionality allows the cRIO to take measurements over longer periods of time without constant supervision. This method was used at Moholt for over night recordings.

4.5.4 First-In First-Out mechanisms

First-In First-Out mechanisms (FIFOs) use rapidly accessible memory to store data temporarily, and require an input and an output. On the input side, the FIFO writes data in a certain order. On the output side, the FIFO reads data in the order it was written. This makes it possible to move data easily within a VI or between VIs. When acquiring data, having control of the sampling rate is essential. When data is written to a file, the time spent is of a more arbitrary nature. Therefore, the FIFO acts as a buffer between the input and output and ensures that data is sampled evenly without data loss.

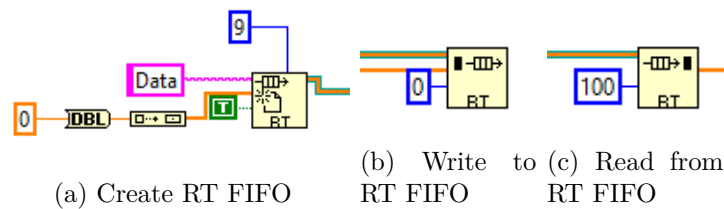


Figure 4.7: RT FIFO structure

4.5.5 Filtering and downsampling

There are several ways to filter the data with respect to the frequency content of the signal. A filter can be applied to an entire channel in a measurement file or applied to a continuous stream of data. In the scan mode VIs, a point-by-point butterworth filter was set to filter out frequency content above 80% of the *Nyquist frequency* in order to avoid *aliasing* [35]. The filter was placed inside the timed loop in scan mode. Otherwise, downsampling could not have been done before the FIFO and that might have slowed down the FIFO.

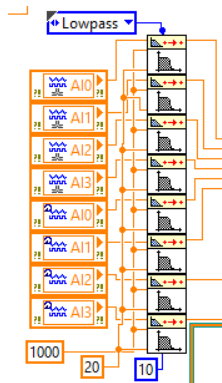


Figure 4.8: Continuous Lowpass Butterworth filter

4 MEASUREMENT METHODS

After the data had been filtered it was downsampled. The reason for doing this was to make the FIFO and data logging more efficient and therefore avoid problems regarding sampling rate. The downsampling was performed by only letting every n 'th point pass through the FIFO, where n is called the *downsampling factor*.

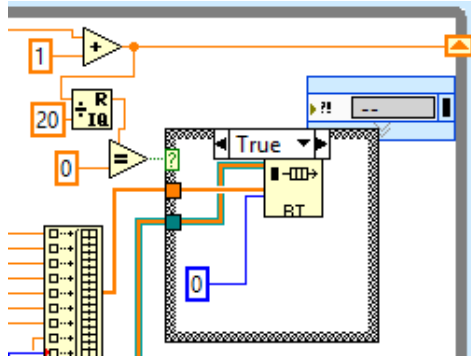


Figure 4.9: Downsampling

4.5.6 Aliasing

Aliasing occurs when data is acquired at a sampling frequency lower than twice the highest frequency of the harmonic components in the signal, or when unfiltered data is downsampled [35]. The effect causes *folding*, which means that frequency content above half the sampling rate will appear in the area underneath half the sampling rate in the APSD of the signal. The same effect in the time domain is shown in Figure 4.10. Therefore, the data has to be filtered before downsampling. This means filtering out the frequencies above of half the desired frequency. This frequency $f_{sampling}/2$ is called the Nyquist frequency. Filters in the time domain are not able to completely remove all the frequency components outside the cut-off frequency. Therefore, the cut-off frequency of a lowpass filter is typically set to 80% of the Nyquist frequency.

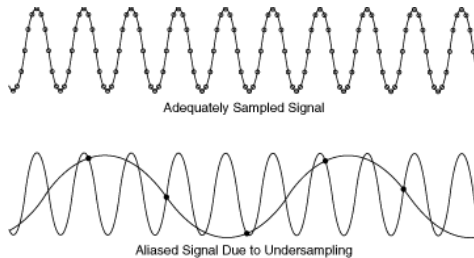


Figure 4.10: Aliasing in the time domain, [35]

4.5. LABVIEW PROGRAMMING

Below is an example showing the effects of aliasing in the frequency domain when a 1000Hz signal containing 15,70,80 and 90Hz components is downsampled to 50 Hz. As can be seen the frequency components of 70,80 and 90 Hz are folded down into the area below the Nyquist frequency of 25Hz. This is because when downsampling an unfiltered signal the picked-out data points generate spurious frequency components. Each of the spurious frequency components equal to $|n * f_{sampling} - f_{component}|$ [35], where n is the integer that causes $n * f_{sampling}$ to be closest to $f_{component}$. The effect was also tested with a 10th order lowpass butterworth filter set to a cut-off frequency of 20Hz. It can be seen that this causes the spurious frequency components to disappear while the component at 15Hz is still present. This shows that the filters used in the data processing have the desired effect.

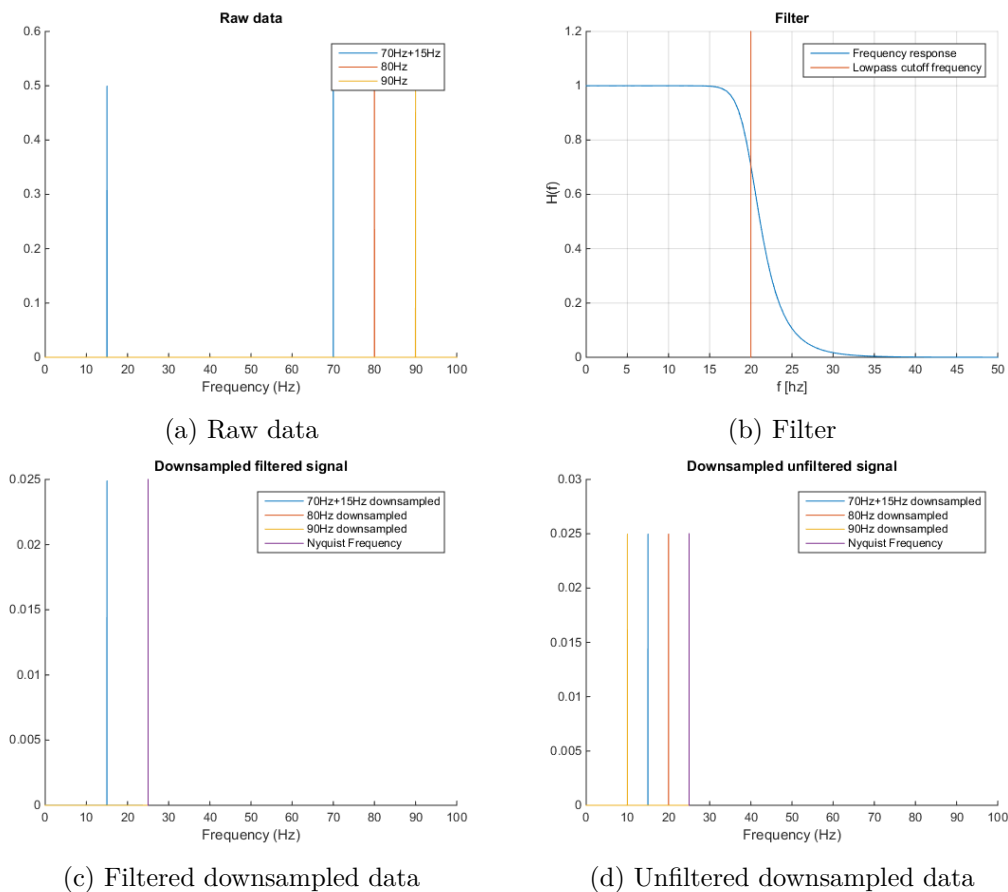


Figure 4.11: Effects of aliasing for filtered and unfiltered signal

4 MEASUREMENT METHODS

Chapter 5

Numerical model of Moholt 50|50

The need for a numerical model of Moholt 50|50 was made evident late in the process because it was not possible to acquire a model in the time available. Therefore, a quick model was made in Abaqus/CAE to indicate what should be expected from the measured results. It was also a way to check how accurate an easy-made model can predict the real-life behaviour of CLT buildings. All modelling in Abaqus was based on the proposed solutions and explanations of functions from SIMULIA [40].

The model consist of CLT walls, floors and roofs. Three glulam beams in each story were neglected when they were shown to contribute little to the global system. They only caused spurious local bending modes. Any non-structural elements that may have an effect on the behaviour of the building were also neglected.

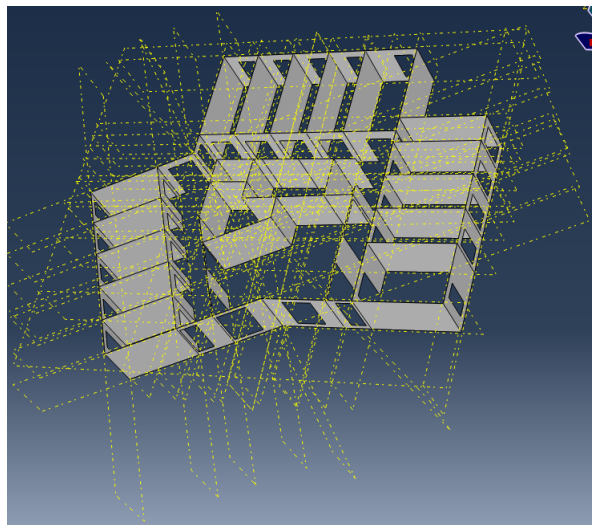


Figure 5.1: One story of Moholt 50|50

5.1 Materials

Two materials needed to be defined in order to make the model; regular CLT elements and CLT elements with the added weight of 70mm concrete. The regular CLT in the walls was modelled with a density of $480\text{kg}/\text{m}^3$ while a higher density was used for the 140mm thick CLT floors in order to account for the mass of a 70mm layer of concrete. This meant that the total density of the floors were $1730\text{kg}/\text{m}^3$. The floors were assumed stiff compared to the rest of the building. Both materials stiffness were modelled with engineering constants [15].

E1	E2	E3	ν_{12}	ν_{13}	ν_{23}	G12	G13	G23
8730	4730	500	0.35	0.35	0.2	540	94.9	747

Table 5.1: Material properties of CLT. Elastic moduli are given in MPa.



Figure 5.2: 120mm CLT at Moholt 50|50

5.2 Elements

All CLT parts were modelled using S4R shell elements. The elements were chosen automatically by Abaqus and deemed suitable.

5.3 Assembly

The building was modelled with 8 equal stories stacked on top of each other and connected together by the walls on each floor. All connections inside each story were modelled as rigid. Between each floor the connections were modelled as rigid in one simulation and hinged in another. The first eigenfrequency estimates were just 2.3% different from each other, and there was no significant change in the mode shapes. Therefore, only the results for hinged connections are presented.

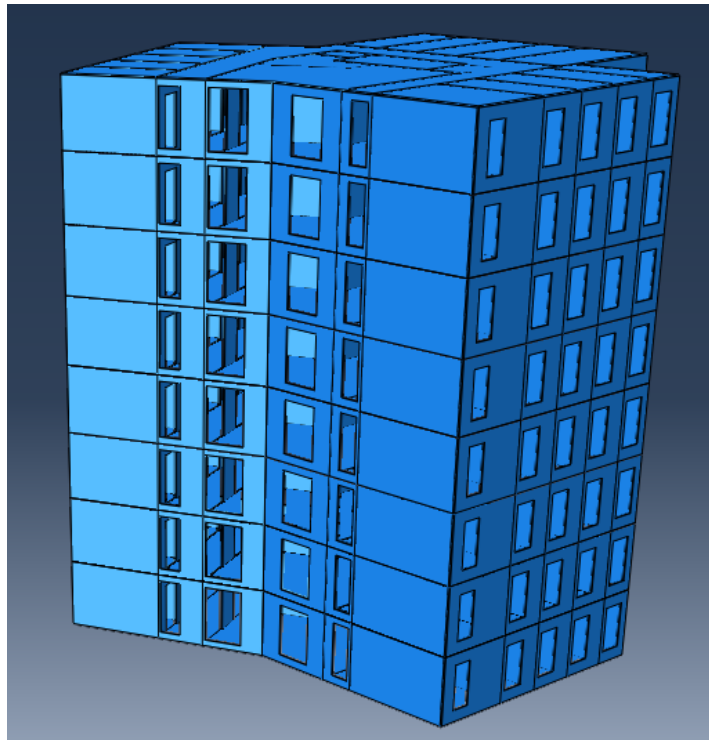


Figure 5.3: Assembly of Moholt 50|50

5.4 Results

Extracting the dynamic properties of the model required a job containing a step that extracted natural frequencies and mode shapes. The step used a *Lanczos eigenvalue solver* to extract the relevant data.

Modes 1-6 are presented in the table below with their respective natural frequencies and relative displacements at each of the planned accelerometer locations. Also, mode 1-3 is presented mode by mode with figures and explanations since these modes are considered most important for the dynamic response of Moholt 50|50. The coordinate system and directions used to describe the mode shapes are defined in Figure 6.3.

Mode	1	2	3	4	5	6
X (West)	0.023	0.661	-0.638	-0.088	0.504	1.000
Z (West)	1.000	-0.615	-0.511	1.000	-0.403	0.091
X (East)	-0.104	1.000	-0.244	-0.323	0.870	0.780
Z (East)	0.516	0.685	1.000	0.099	1.000	-0.737
Natural Frequency	2.2634	2.4857	2.6792	7.1502	7.7340	8.6943

Table 5.2: Mode shapes and frequencies for mode 1 to 6

5.4.1 Mode 1

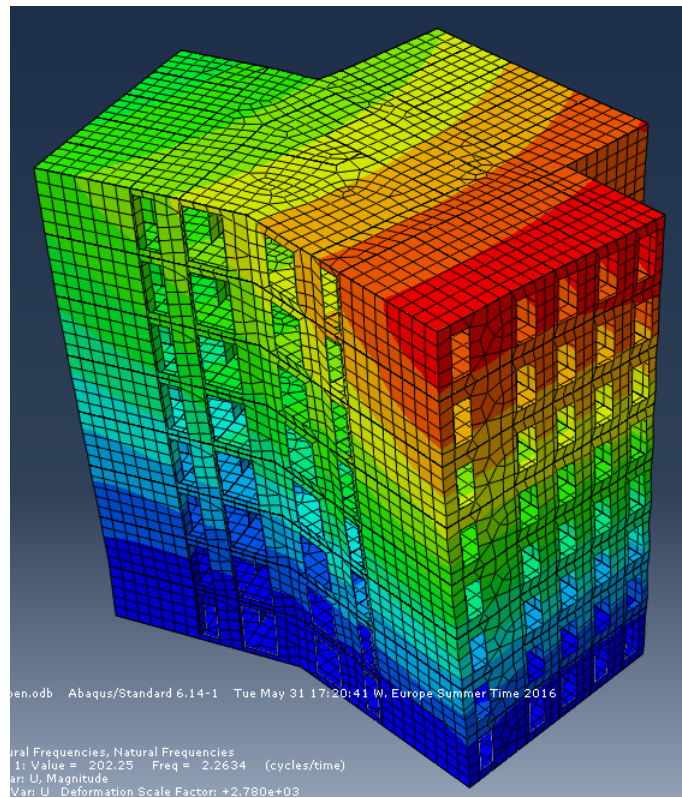


Figure 5.4: Mode 1

Mode 1 is mainly a cantilever type bending mode approximately in the global Z-direction. The natural frequency is 2.2634Hz. As can be seen from the figure, the mode exhibits some torsional effects. This is probably caused by the unsymmetrical shape of the building.

5.4.2 Mode 2

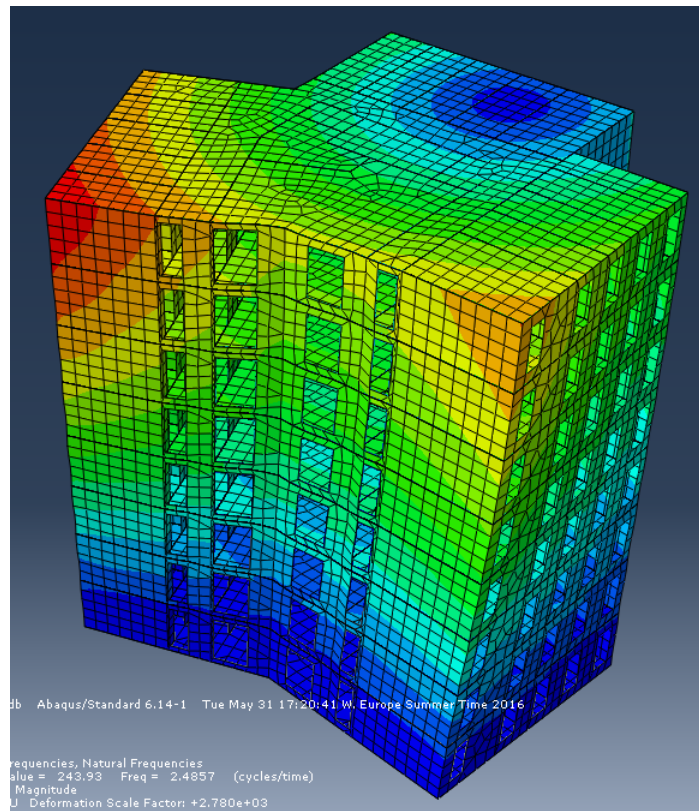


Figure 5.5: Mode 2

Mode 2 is mainly a torsional mode rotating around a local axis in the Y-direction centred in the southern protruding part. The natural frequency is 2.4857Hz. This mode also seems to be effected by the unsymmetrical shape of the building.

5.4.3 Mode 3

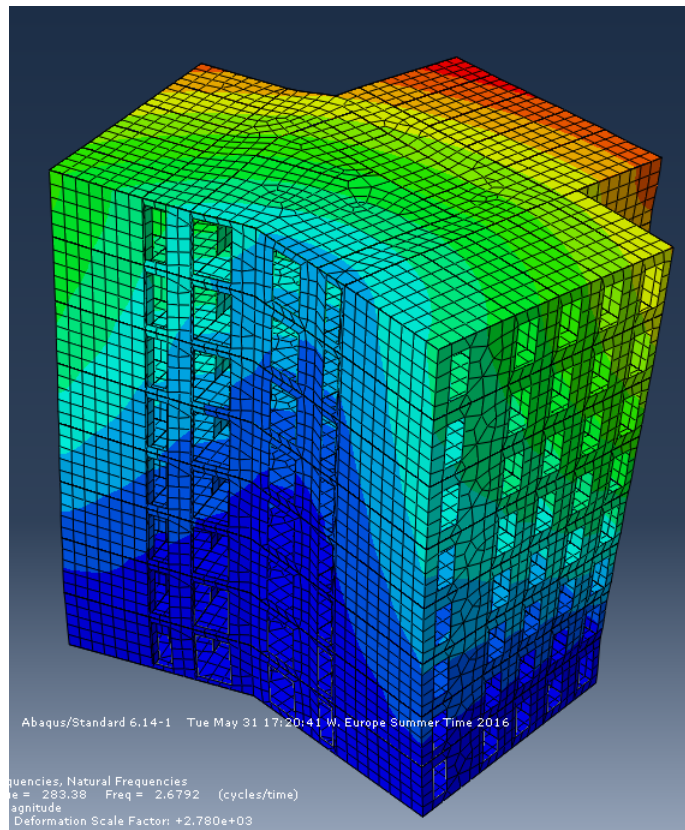


Figure 5.6: Mode 3

Mode 3 is a torsional mode rotating around a local axis in the Y-direction centred just outside the 25° kink in the front facade. The natural frequency is 2.6792Hz. Similar to the other modes, it exhibits large torsional behaviour. This seems to be present in higher order modes as well.

5.5 Accelerations and the Serviceability Limit State (SLS)

From a combination of the geometry and mass properties of the numerical model, frequencies and damping from the measured results can be used for an estimate regarding the maximum expected accelerations. A MatLab script based on a script made by Ingunn Utne [45] and the wind standard [30] was used to calculate the accelerations. The wind field properties were assumed similar to the wind field properties at Treet in Bergen, as it is situated in the same terrain category. The reference wind speed is the same for Trondheim and Bergen, $26m/s$. The calculations were only performed for mode 1, which is the mode most similar to a cantilever bending mode. In the table below, the maximum calculated accelerations and the requirements at the relevant frequencies from ISO10137 [19] are presented.

Direction	Acceleration (m/s^2)	Frequency (Hz)	Damping	ISO10137 (m/s^2)
Z	0.0397	2.183	2	0.0437

Table 5.3: Estimated maximum accelerations at Moholt 50|50

It can be seen from the table that the maximum calculated accelerations fulfil the requirements stated by ISO10137. Furthermore, the calculated accelerations are below the limit for nausea at $0.098m/s^2$ stated by Boggs [12].

5.6 Discussion regarding accuracy of model

Some inaccuracy may arise because all walls are modelled as rigidly connected to each other. This will be stiffer than the actual connections. However, it is expected that the complexity of the structure makes the dynamic behaviour largely unaffected by the stiffness of the joints [45]. There may also be certain connections that are disrupted by sound-proofing materials in the actual building [25]. However, too little information regarding this was available and the effects are unknown for the time being.

All the CLT values for the engineering constants are taken from experiments performed on small CLT plates and from these experiments homogenized values are extracted. This is to a certain degree an inaccurate way to represent the material, since the thicknesses and number of laminations of the CLT elements in the model are different from each other. It is expected that the homogenized elastic values should be different for differences in the number of laminations and their respective thickness. However, modelling the material properties that way was regarded as too cumbersome for the purpose of the model.

5.6. DISCUSSION REGARDING ACCURACY OF MODEL

Regarding the maximum acceleration calculations, there are some inaccuracies. The number of towers placed at Moholt 50|50 makes the nature of the wind field at the site highly uncertain. In addition the geometric properties used as input in the calculations seem apply for rectangular buildings, while the towers at Moholt 50|50 are Y-shaped. The natural frequencies are the ones extracted from the measurements and they are believed to be accurate. By contrast, the damping ratios are believed to be highly inaccurate. The assumed modal damping ratio at 2% is considered conservative considering that experiments by Reynolds et al., 2015 [38] and Ceccotti et al., 2013 [14] indicate much higher damping. Finally, the weight and stiffness is only composed of the structural system and not any non-structural elements. It is uncertain how this affects the dynamic properties.

The results from the model are not expected to be completely accurate and may have been better if more time had been available. However, the model was deemed acceptable as the dynamic properties of the model coincide well with the measured dynamic properties.

Chapter 6

Measurements

The measurements at Moholt were taken at two equivalent towers on two separate days. They were performed on towers that were in different parts of the construction phase. This is expected to produce some differences in the results, but the towers should have largely the same dynamic properties. In Bergen, the building was already finished. Therefore, between the two measurement days it is not expected to be significant differences in the results. However, Reynolds 2015 et al., [37] suggest that the damping estimates are somewhat dependent on load amplitudes.

6.1 LabVIEW Preparations

Prior to every measurement, LabVIEW VIs were made and tested in the lab. The VIs for Moholt One and Bergen Day 1 were mostly the same with some small differences. The same is true for Moholt Two and Bergen Day 2.

6.1.1 Bergen Day 1 and Moholt One

Two different LabVIEW VIs were made for obtaining data, one for acquiring data at 1000Hz and one for acquiring filtered and downsampled data. Both VIs used the LabVIEW Scan Engine set to a sampling rate of 1000 Hz. The data was monitored using waveform charts and graphs. No timestamps were acquired.

The first VI was made with a for loop that was supposed to acquire one data point each channel every millisecond and then saved after 2000 iterations. The second VI had the same loop as the first, except that the data was filtered before the for loop was finished. After the loop was finished the data was transposed and downsampled in a channel by channel for loop. The data was downsampled to 50Hz after filtering at 20Hz corresponding to 80% of the Nyquist frequency.

6 MEASUREMENTS

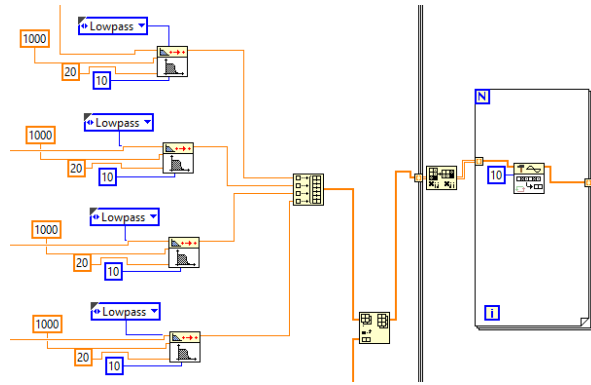


Figure 6.1: Continuous Butterworth Lowpass Filter with downsampling

The VI used during daytime at Moholt One was identical to the first VI used during Bergen Day 1. However, another VI was made with the same basic layout. It was configured to run independently and save time series in one hour intervals. This VI was used to gather data over a weekend.

6.1.2 Bergen Day 2 and Moholt Two

Two different VIs were made for Bergen Day 2; one was designed for FPGA to acquire data from 4 channels and the other for scan mode acquiring data from 8 channels. Both VIs had timestamps that effectively extended the measurement files by one channel.

The FPGA VI was a very simple program that acquired data at 1652Hz and sent it to the real-time target using a FPGA FIFO. The FIFO recorded 280 points from each channel before releasing it in the Real-Time VI. The data was then timestamped by the number of micro seconds μs between each FIFO reading, and further logged on to a tdms file.

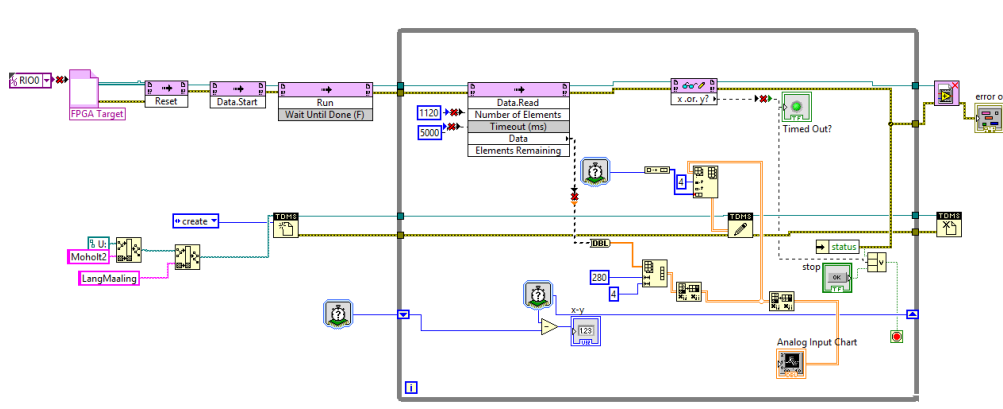


Figure 6.2: FPGA host VI

The scan mode VI was constructed with a timed loop and a while loop running simultaneously, where the timed loop acquired the data and the while loop logged the data. In the timed loop, before the data was sent to the while loop through a FIFO, the data was filtered with a lowpass cut-off set to 20Hz and downsampled from 1000Hz to 50Hz.

At Moholt Two, an FPGA VI similar to the one used during Bergen Day 2 was used. The only difference was that it was configured to run independently on the cRIO overnight.

6.2 Layouts

The layout of the measurement system was largely the same on the two trips to the respective locations. However, some small changes were done to comply with restrictions regarding either equipment or availability. Details for each system layout are given in Appendices A and B.

6.2.1 Moholt

During Moholt One the layout consisted of two accelerometers in both the 9th and the 7th floor. They were placed as far away from each other as possible along the facade that has a 25 degree kink. The accelerometers were fastened on the inside of the outside walls. The sensors were mounted to the structural system by resting on a wood screw and further fastened using electrician tape.

During Moholt Two the same layout as Moholt One was used, but only in the 9th floor. This time the screws worked as they were supposed to. During the over-night recording, the western accelerometer experienced an extreme peak acceleration about one hour into the recording. The next morning, the accelerometer had rotated approximately 135° about its local Z-axis, off-setting its local X-axis.

6 MEASUREMENTS

Figure 6.3 shows the local coordinate system of each accelerometer and the global coordinate system used to present the results.

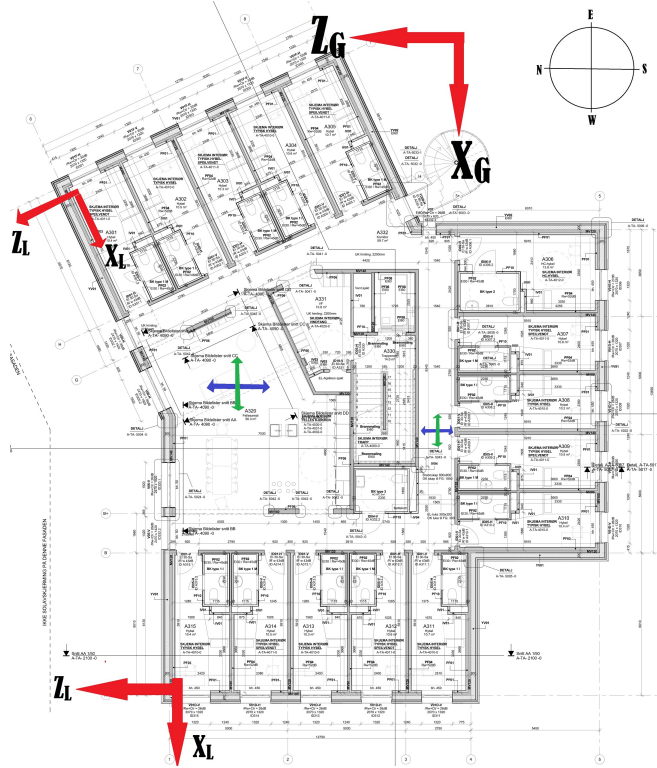


Figure 6.3: System layout of Moholt 50|50

The following relations are used to transform data from the eastern accelerometer into the global coordinate system:

$$X_G = X_L \cdot \cos(25^\circ) + Z_L \cdot \sin(25^\circ) \quad (6.1)$$

$$Z_G = Z_L \cdot \cos(25^\circ) - X_L \cdot \sin(25^\circ) \quad (6.2)$$

6.2.2 Bergen

The setup during Bergen Day 1 consisted of two accelerometers in both the 9th and the 13th floor. They were placed as far away from each other as possible while still being at the same height in each floor. The cRIO was placed on the 13th floor while the expansion chassis was placed on the 9th floor. They were connected to each other with an Ethernet cable. On both floors a PCB accelerometer was placed in the north-western end of the building and a Kistler accelerometer in the south-eastern end of

6.3. MEASUREMENT CONDITIONS

the building. They were all screwed to glulam columns, which are part of the main structural system.

The accelerometer setup during Bergen Day 2 was largely the same as for Day 1, except that half of the measurements were only performed on the 13th floor. This was because the FPGA VI was limited to using only the cRIO. During the FPGA measurements, only the Kistler accelerometers were used to carry out the measurements. This was chosen because the Kistler accelerometers seem to produce less low-frequency noise than the PCBs. During the measurements using scan mode, the setup was the same as for Bergen Day 1.

Figure 6.4 is created using a snapshot from google maps [4].

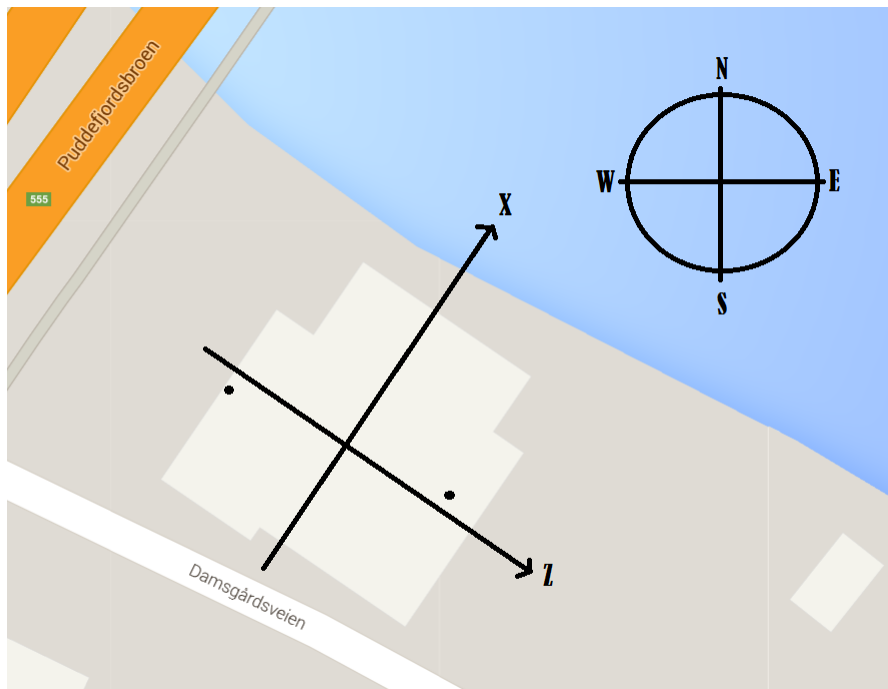


Figure 6.4: Coordinate system used to present the results from Treet

6.3 Measurement Conditions

The evaluation of measurements conditions were based on personal experiences, weather data and looking at the scatter of results extracted from Cov-SSI. It can be seen from the results that when the load amplitude is either low or not close to the white noise assumption for OMA, the extracted dynamic properties are more uncertain. Weather data during each measurement was extracted from *yr.no* or *eKlima.no*, and can be found in the digital appendix.

6.3.1 Moholt One

The first set of measurements on Moholt 50|50 were taken on the 11th of March and in segments from the 11th to the 14th. During the 11th, activity at the construction site was the dominating load input for the longer measurements. Shorter measurements were performed during the day, having four people shaking simultaneously at a certain frequency. See Chapter 7 for details. During the weekend, the dominant load input was wind, but unfortunately the wind speeds were too low to produce any clear results.

6.3.2 Moholt Two

The set of measurements on Moholt 50|50 were taken between the 24th and the 25th of May. The load inputs were basically the same as on the first trip with large inputs from construction activity and low wind speeds. However, better VIs were able to provide better results. Time series were recorded for two input directions at two locations indicated by the blue and green arrows in Figure 6.3.

6.3.3 Bergen Day 1

The first trip to Bergen was made on the 18th of April to the 19th of April, and the measurements were taken on the 19th. It was a windy day with recorded mean wind speeds up to $9.0m/s$ and gusts up to $14.7m/s$ at the closest meteorological station [49]. The main wind direction was from the north-west. Although the effects of wind were not noticeable inside the building, there was enough wind to produce clear results. It was not experienced that there was any other activity in the building or surroundings that effected the results in any significant way.

6.3.4 Bergen Day 2

The second trip to Bergen was made from the 1st of May to the 2nd of May, and the measurements were done on the 2nd. This day was even more windy than the the first trip, with recorded wind speed averages of around $10m/s$ and gusts of up to $18m/s$ [50]. The wind direction was the opposite direction of the first trip, and came from south-east. Similar to the first day, it was not experienced that there were any other activity in the building or surroundings that effected the results in any significant way.

6.4 Evaluating accuracy

The second set of measurements at both Moholt and in Bergen has been considered accurate. The reasoning behind this is provided in Appendix C. However, there were problems with the first set of measurements at both places. For the first trip to Bergen, a thorough evaluation of the accuracy of the results has been performed. This evaluation is provided in Appendix C.2, and the conclusion is that results are usable, but noisy. The results from the first trip to Moholt exhibited similar but larger difficulties. Therefore only the accelerations excited by the four people shaking the upper floor are included in the report. For more details, see Appendix C.1. The problematic measurements of Bergen Day 1 provide some interesting results and will therefore be presented in Appendix B.2.1.

6 MEASUREMENTS

Chapter 7

Results

The results presented in this chapter are chosen from a larger set of data that is presented in Appendix A and B. First, stabilization diagrams for the time series considered most successful are presented. Then, plots of the APSDs show the power of different harmonic components for representative time series recorded on each building.

Next, the detected natural frequencies from the APSDs and stabilization diagrams are presented. The natural frequencies and damping ratios from Cov-SSI are presented statistically by a mean value and a standard deviation of a selection of the data underlying the stabilization diagrams.

The modal numbering along vertical alignment of poles in the stabilization diagram might not seem systematic. A set of restrictions is applied to the data from Cov-SSI in an attempt to identify each physical mode. The first restriction is that only the orders containing poles considered stable, and therefore also physical, are included. The second restriction is that those results in the stable orders that deviate too much in terms of natural frequency are not included. This creates a rectangular window like the one in Figure 7.1. In an attempt to remove the last non-physical poles inside the window a damping criterion is introduced as the non-physical poles tend to exhibit damping ratios that are either abnormally large or small, sometimes even negative. The mean value and the standard deviation of natural frequencies and damping ratios buried within the remaining poles are the presented results.

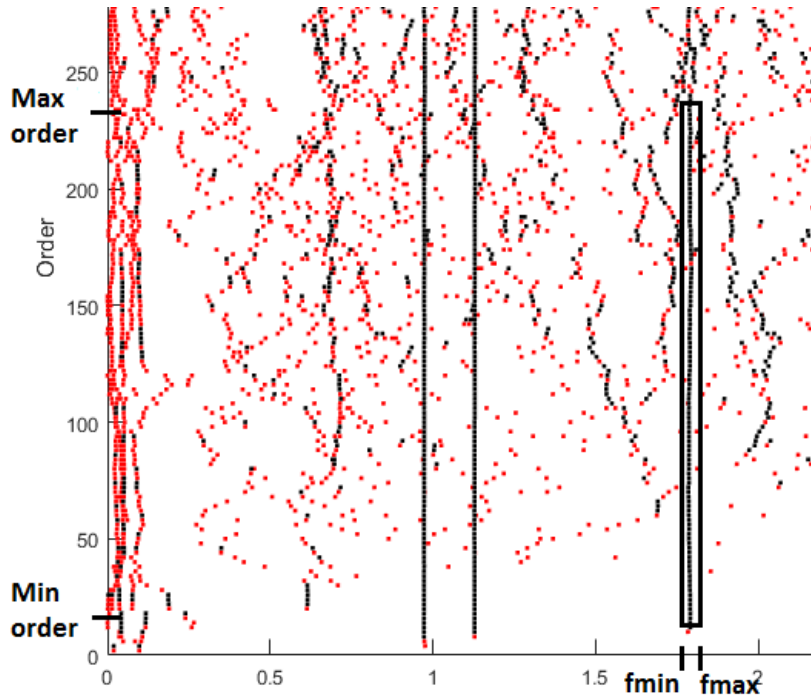


Figure 7.1: Chosen values for one mode

The mode shapes are extracted from one of the poles, fulfilling the previous restrictions, that is considered representative. They are presented by the relative acceleration magnitudes between each accelerometer in each mode.

In order to identify peak accelerations, the time series have been lowpass filtered with a 10^{th} order butterworth filter set to just above the highest natural frequency considered important for the structural response. Dynamic displacements have been obtained by twice integrating each acceleration time series. After each integration, the resulting time series were highpass filtered with a 5^{th} order butterworth filter in order to remove non-physical low frequency components arising from the numerical integration. The peak values considered representative for the structural response are pointed out using bold text.

Downsampling has been performed using MatLab's *resample*-function with a built-in anti-aliasing filter [7]. Lowpass and highpass butterworth filters are used in MatLab, and are applied to the time series using MatLab's *butter*- and *filtfilt*-functions [6, 9]. The FFTs of the time series have been calculated using MatLab's *fft*-function and the frequency axis has been appropriately organized using MatLab's *fftshift*-function [2, 3]. When Welch's Estimate has been used to calculate APSDs, MatLab's *cpsd*-function has been utilized [8].

7.1 Moholt

The results from Moholt One were not accurate, since the time series exhibited problems with the sampling rate. However, some results regarding maximum accelerations have been included. The results from Moholt Two are believed to be accurate, but with disturbances from construction work.

The accelerometer recordings were obtained for two types of structure excitation. Excitation type one consisted of people on the top floor, guided by a metronome in order to simultaneously step from side to side at different frequencies. The second excitation type was caused by environmental loads.

7.1.1 Stabilization Diagram

The following stabilization diagram is based upon data converted into the global coordinate system using equations 6.1 and 6.2. The measurement data has been downsampled from 1652Hz to 59Hz. 70 blockrows have been used to establish the corresponding Toeplitz matrix of the system. Figure 7.2 shows a stabilization diagram of Moholt Two when there was ongoing construction activity:

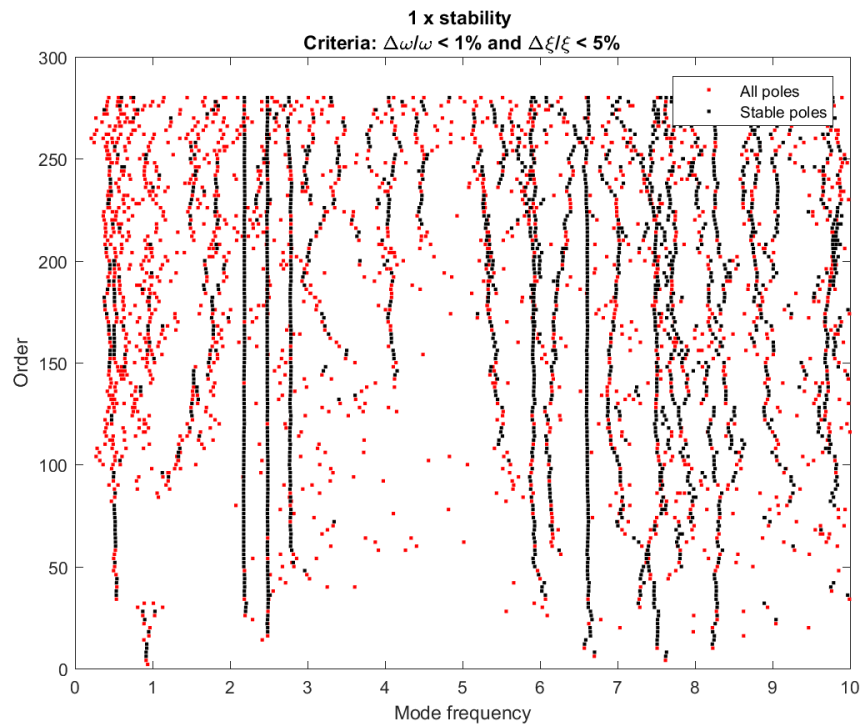
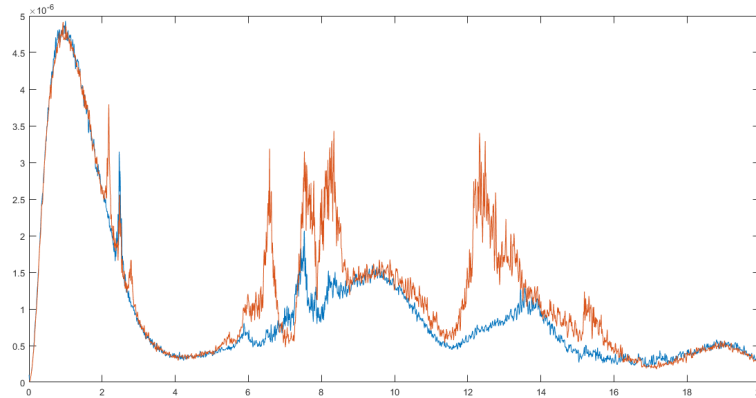


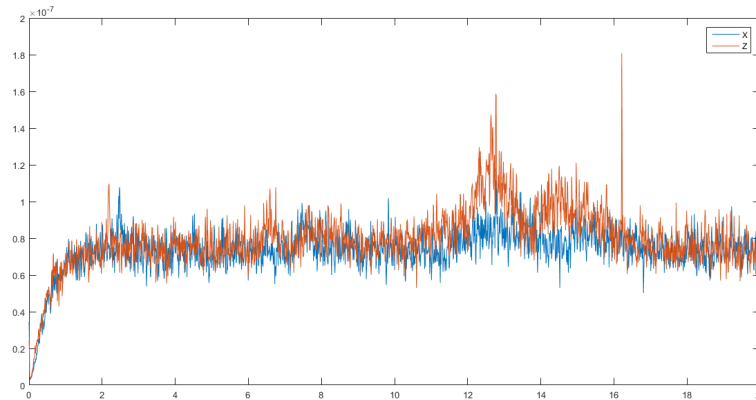
Figure 7.2: Stabilization diagram from Moholt Two

7.1.2 Auto Power Spectral Densities

Recorded time series, with and without construction activity, were downsampled to 59Hz. Then, Welch's Estimate was calculated weighting 60 segments with Hanning windows and 50% overlap.



(a) APSD with construction activity



(b) APSD without construction activity

Figure 7.3: APSD plots from Moholt Two

The APSDs without construction activity do not show the broad banded peaks at 0 to 3Hz and 6 to 11.5Hz that were observed with activity on site in Figure 7.3a. This could indicate that they were detected input frequencies from construction activity around the building. This assumption is made because they are not the narrow banded peaks that are expected from a structure with constant properties.

7.1.3 Natural Frequencies

Mode	f_n from APSD	Mean f_n from Cov-SSI	σ_{f_n}
1	2.183	2.183	4.33e-3
2	2.466	2.483	2.85e-3
3	2.796	2.779	7.76e-3
4	6.582	6.609	7.57e-3

Table 7.1: Natural Frequencies of the detected modes at Moholt 50|50

7.1.4 Damping

Table 7.2 show damping ratios at Moholt 50|50 with (left) and without (right) construction activity:

Mode	ξ , with act.	σ_ξ	ξ , without act.	σ_ξ
1	1.50	1.13e-1	2.68	3.31e-1
2	1.48	9.31e-2	2.88	7.96e-1
3	2.05	3.44e-1	-	-
4	2.26	9.41e-2	2.41	1.05e-1
5	-	-	2.96	2.59e-1

Table 7.2: Damping ratios from Moholt Two

7 RESULTS

7.1.5 Mode shapes

The modes are described by the relative response amplitudes at each accelerometer in the top floor in the global coordinate system.

Entry	Mode 1	Mode 2	Mode 3	Mode 4
1	-0.256	-0.856	-0.183	-0.359
2	-0.910	0.612	1.000	1.000
3	-0.243	-1.000	-0.391	-0.211
4	-1.000	-0.216	-0.901	-0.750

Table 7.3: Detected mode shapes at Moholt 50|50

- Mode 1 is mainly a translational mode along Z-direction.
- Mode 2 is mainly a translational mode in the X-direction with torsional centre towards south-east of the building.
- Mode 3 is mainly a torsional mode with torsional centre approximately at the kink of the facade.
- Mode 4 is mainly a torsional mode with torsional centre a little bit further east than mode 3. It is also expected that this mode has inflection points further down in the building.

7.1.6 Maximum acceleration and displacements

Construction activity

The cut-off of the lowpass filter was set to 3.75Hz and the cut-off of the highpass filter was set to 0.4Hz.

Channel	Max. Acc [mm/s^2]	Max. Displ [mm]
1	5,20	0,0425
2	5,12	0,0500
3	136,86	4,6633
4	696,19	8,4633

Table 7.4: Maximum accelerations and displacements of Moholt 50|50 with construction activity

Channels 3 and 4 are not considered representative for the structural response because they exhibit extreme peak values that are likely to occur because work was performed inside the building during the recording.

No construction activity

The cut-off of the lowpass filter was set to 3.75Hz and the cut-off of the highpass filter was set to 0.218Hz.

The maximum detected acceleration is about half the maximum detected acceleration when there was activity on the site, and the maximum dynamic displacement obtained through numerical integration is larger than when there was activity on site. Even after the signal has been filtered, some of the power within the selected frequency band will come from measurement noise. A more thorough discussion is presented in Appendix C.5.

Four people shaking at a set frequency

At Moholt One, time series were recorded of four people trying to excite the building at an approximate input frequency of 2.5Hz. They were situated in the middle of the floor indicated by the northern green and blue cross in Figure 6.3 and the results provided here are from the time series with the largest response amplitudes.

For this measurement, the lowpass cut-off was set to 3.75Hz and the highpass cutoff was set to 0.4Hz.

Channel	Max. Acc. [mm/s^2]	Max. Displ. [mm]
1	60,9663	0,5946
2	28,1048	0,4263
3	46,1013	0,4441
4	23,8152	0,2836
5	103,1025	1,2003
6	57,6193	0,7025
7	51,8827	0,4016
8	22,6078	0,2191

Table 7.6: Maximum accelerations and displacements from four people shaking Moholt 50|50

It is noticed that the highest detected acceleration amplitude exceeds the criterion stated by Boggs, 1997 [12].

Channel	Max. Acc. [mm/s^2]	Max. Dyn. Displ. [mm]
1	1,757	0,0728
2	2,360	0,0990
3	2,594	0,0756
4	2,135	0,1188

Table 7.5: Maximum accelerations and displacements of Moholt 50|50 without construction activity

7.2 Bergen

The results from Bergen Day 1 are, because of the aforementioned problems, not as accurate as hoped. However, some results were extracted with an estimated mean sampling rate. The results from Bergen 2 are considered to be the most accurate, as there were no problems regarding the sampling rate or load inputs from other factors than wind. The complete set of results from Bergen Day 1 and Day 2 are found in Appendix B, while a short presentation of the measurements considered most accurate are presented here. These results are from the first FPGA time series on Day 2.

7.2.1 Stabilization Diagram

The following stabilization diagram has been created after resampling each channel from 1652Hz down to 59Hz. 90 blockrows have been used to establish the Toeplitz matrix of the system.

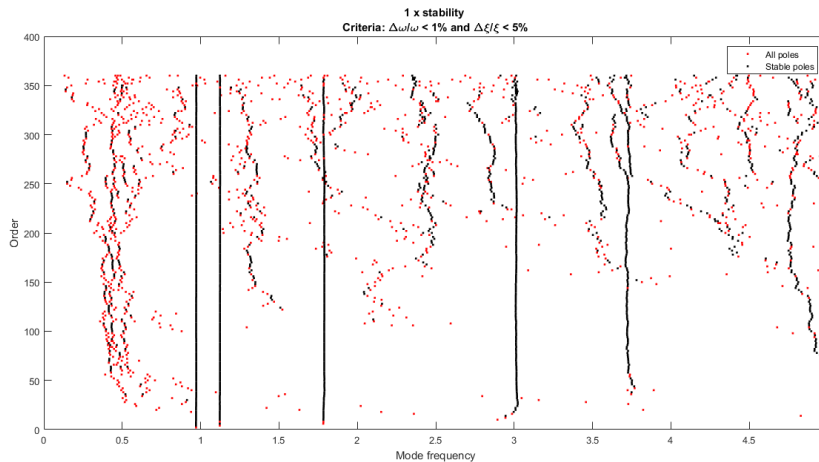


Figure 7.4: Stabilization Diagram of data obtained using FPGA

7.2.2 Auto Power Spectral Densities

In order to calculate the APSDs, the measurement file was downsampled to 59Hz. Then, Welch's Estimate was calculated weighting 40 segments with Hanning windows and 50% overlap.

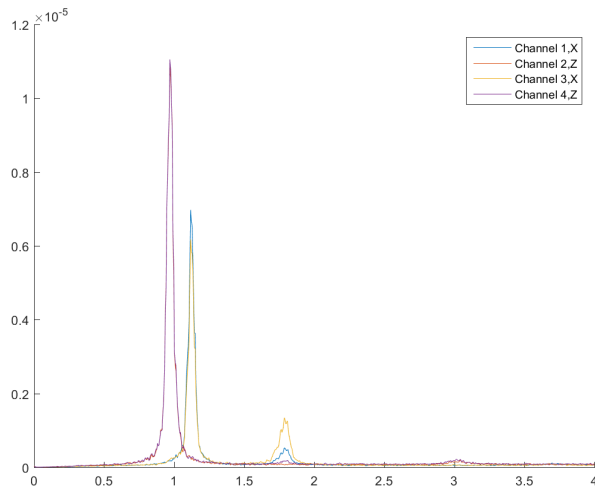


Figure 7.5: APSD of all channels using FPGA on Day 2 in Bergen

7.2.3 Natural Frequencies

Mode	f_n from APSD	Mean f_n	σ_{f_n}
1	0.975	0.972	7.57e-5
2	1.13	1.12	2.92e-4
3	1.80	1.79	4.49e-4
4	(3.01)	3.01	1.78e-3
5	Unclear	3.72	4.94e-3

Table 7.7: Natural Frequencies of the detected modes at Treet, using FPGA

7.2.4 Damping

Mode	Mean ξ	σ_{ξ}
1	1.84	7.85e-3
2	1.61	1.68e-2
3	1.98	4.93e-2
4	2.28	5.74e-2
5	2.45	9.26e-2

Table 7.8: Damping Ratios from Treet, using FPGA

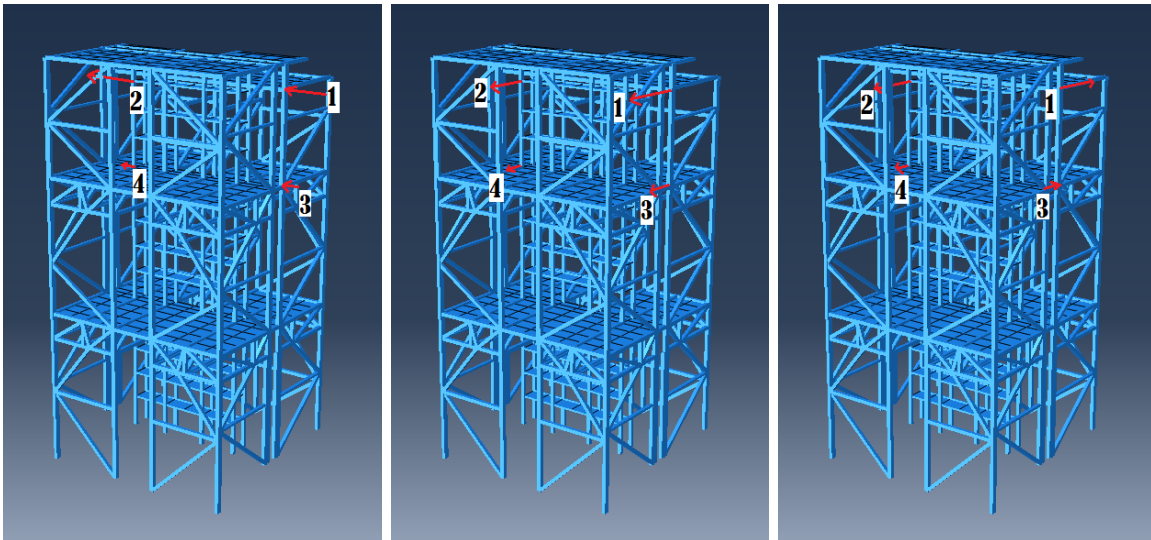
7 RESULTS

7.2.5 Mode shapes

Due to small response magnitudes orthogonal to the dominant directions in each mode, they have been left out of Table 7.9. The mode shapes exhibit little phase shift, and can be represented using only real values. See Appendix B.2.3 for details.

	Mode 1	Mode 2	Mode 3	Mode 4	Mode 5
Entry	Z	X	Torsion	Z	X
1	0.995	1.000	-0.615	0.950	1.000
2	1.000	0.944	1.000	1.000	0.901

Table 7.9: Relative lengths of each mode shape



(a) Bending Mode in Z-direction (b) Bending Mode in X-direction (c) Torsional Mode

Figure 7.6: Modes shapes of Treet

7.2.6 Maximum acceleration and displacements

The lowpass filter was set to 3.5Hz and the highpass filter was set to 10% of the first detected natural frequency at 0.0972Hz.

Channel	Max. Acc. [mm/s^2]	Max. Dyn. Displ. [mm]
1	6,973	0,2131
2	7,748	0,3221
3	7,365	0,2500
4	8,228	0,3349

Chapter 8

Discussion

The time series acquired from both Moholt and Bergen were processed with Cov-SSI to uncover the dynamic properties of the buildings. Numerical models have been created to investigate their respective feasibilities. The numerical models and results from the measurements will be compared and discussed in this chapter.

8.1 Moholt 50|50

Measurements performed at Moholt were all recorded with limited excitation from wind. The most stable results come from time series where construction work was the dominating input on the system. This has somewhat affected the results, but it is assumed that the natural frequencies and mode shapes are realistic. However, the resulting damping estimates are highly uncertain. The results from the measurements are represented by the values believed to be most accurate. For an in-depth review of the results, see Appendices A.3 and A.2.

8.1.1 Natural Frequencies

Figure 8.1 shows the detected natural frequencies from measurements and estimated natural frequencies from the numerical model:

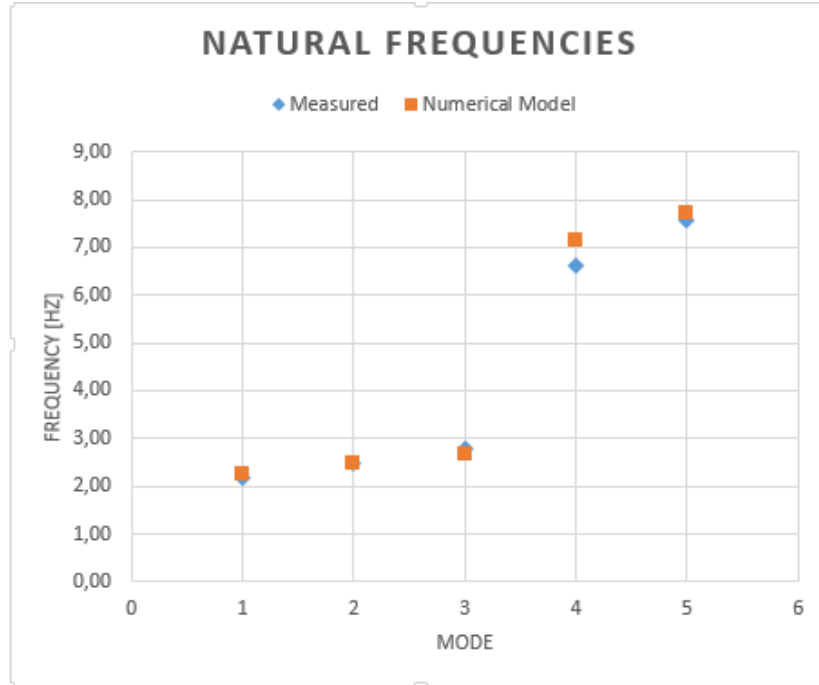


Figure 8.1: Natural Frequencies of Numerical Model and from Measurements

The actual natural frequencies at Moholt 50|50 generally seem to match closely with the results from the numerical model. This is somewhat unexpected as the model has some inaccuracies due to the limited time available to produce it. Mode 4 deviates the most from the measured results, while mode 5 deviates less. This could indicate that the accuracy is due to some degree of luck, rather than being a representation of the actual real life behaviour of the structure.

8.1.2 Mode shapes

The mode shapes extracted from the measurements agree with the mode shapes from the numerical model to some degree. The relative magnitudes seem very different, but this is merely because of a slight shift in the torsional centres of the modes. It is expected that slight shifts of the torsional centres might occur when non-structural components are present in the measurements while being neglected by the numerical model.

8.1.3 Damping

Figure 8.2 shows the detected damping ratios for time series recorded with and without construction activity:

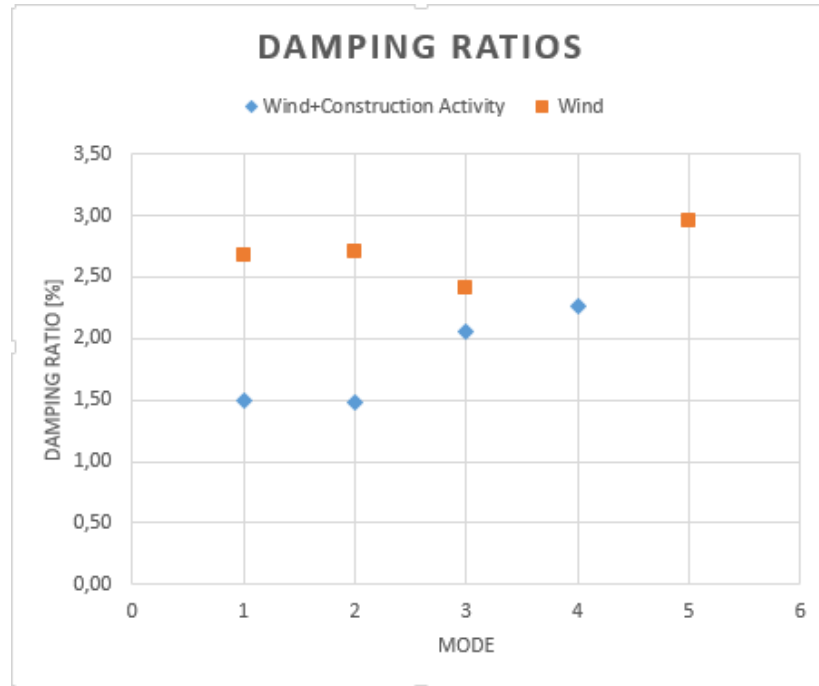


Figure 8.2: Damping estimates without construction activity

Damping estimates for Moholt 50|50 have been ambiguous, as the measurements were performed at a time where there was little to no wind. Most of the system excitation was measured when there was activity on the construction site. The resulting damping estimates may have been affected by the frequency content of construction work, which is not similar to the white noise input assumption made for OMA. It is unfortunately unknown how this affects the estimates. The exact damping will therefore be unknown until measurements are carried out with wind as the dominating input. However, the actual damping is expected to be higher based on previous experiments on tall CLT buildings by Reynolds et al., 2015 [38] and Ceccotti et al., 2013 [14]. Their experiments were performed on buildings with less height and different excitation amplitudes. Therefore, the results are probably not directly comparable.

8.2 Treet

Two different numerical models of Treet are used for discussion, one by SWECO [24] in Autodesk Robot and one made at NTNU in Abaqus [16]. The assumed damping ratios were set to 1.9 in SWECO's model and 1.5 in the NTNU model. The results from the measurements are represented by the values believed to be most accurate. For an in-depth review of the results see Appendix B.

Measurements have been performed on three different occasions; one time by a team from Cambridge [37] during the construction phase, and the two times presented in this thesis.

Table 8.1 shows previous modelled natural frequencies by SWECO and NTNU [24, 16], as well as the natural frequencies and damping ratios obtained by Reynolds et al., 2015 [37].

Mode	f_n SWECO	f_n NTNU	f_n Cambridge	ξ Cambridge [%]
1	0.75	0.7731	1.02-1.03	1.6-2.4
2	0.89	1.0823	1.17-1.19	1.1-1.6
3	-	1.5923	1.86-1.89	0.7-1.4

Table 8.1: Previously estimated and obtained natural frequencies and damping ratios

8.2.1 Natural Frequencies

Figure 8.3 shows the detected natural frequencies along with the estimated natural frequencies by NTNU and SWECO.

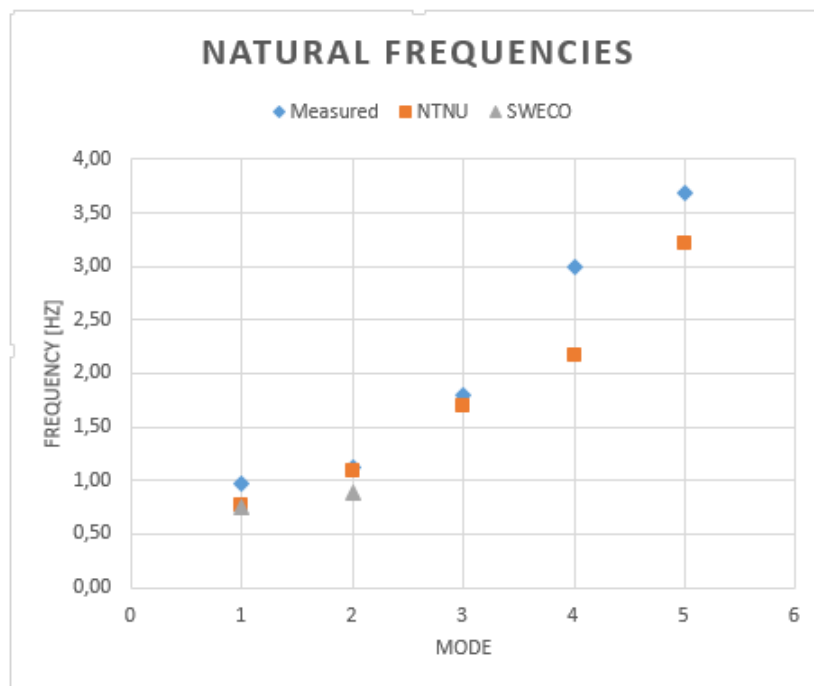


Figure 8.3: Natural Frequencies of Numerical Models and from Measurements

Figure 8.3 shows that the measured natural frequencies are higher than the model in all 5 first modes. Part of the reason for this is possibly that non-structural elements contribute to the stiffness of the building and shifts the natural frequencies upwards. The shift seems likely, because the model does not account for all the non-structural effects. The shift was also expected by the engineers who designed the building [25]. The effect is slightly larger in the bending modes in the Z-direction, and makes sense when considering that the numerical model is not as tied together in the Z-direction as in reality due to the non-structural elements [16].

Figure 8.4 shows the detected natural frequencies in this thesis and the average of the natural frequencies measured by Reynolds et al., 2015 [37].

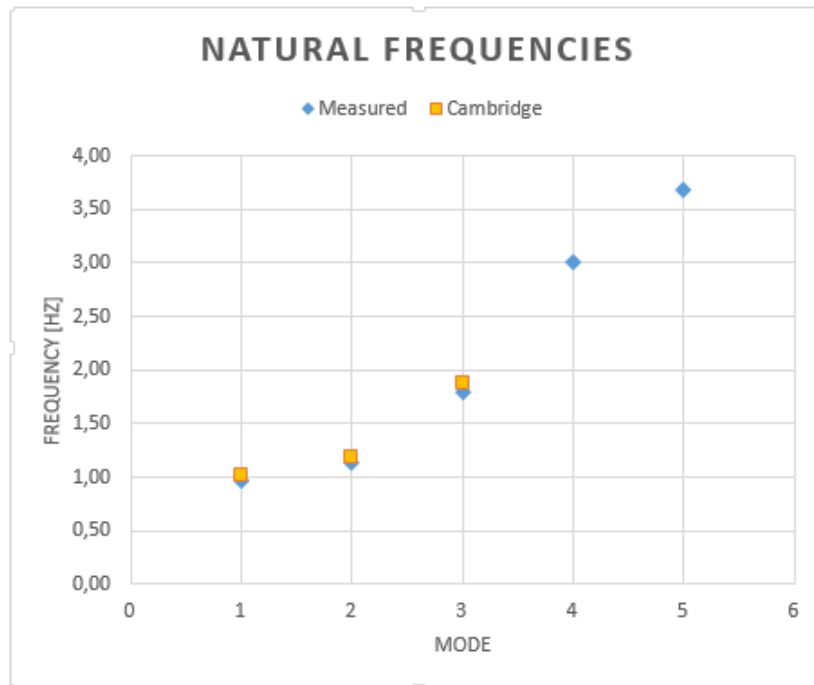


Figure 8.4: Measured Natural Frequencies

The resulting natural frequencies from measurements by the team from Cambridge are on average a bit higher and more uncertain than the results from the measurements in this thesis. The uncertainty is reasonable because the wind excitation was low on their day of measurements.

8.2.2 Mode shapes

The mode shapes obtained from the measurements in this thesis coincide well with the predicted mode shapes from the numerical models [24, 16]. This indicates that the building behaves mostly as predicted.

8.2.3 Damping

Figure 8.5 shows a comparison between the measured damping ratios from Reynolds et al., 2015 [37] and the damping ratios obtained in this thesis using scan mode and FPGA:

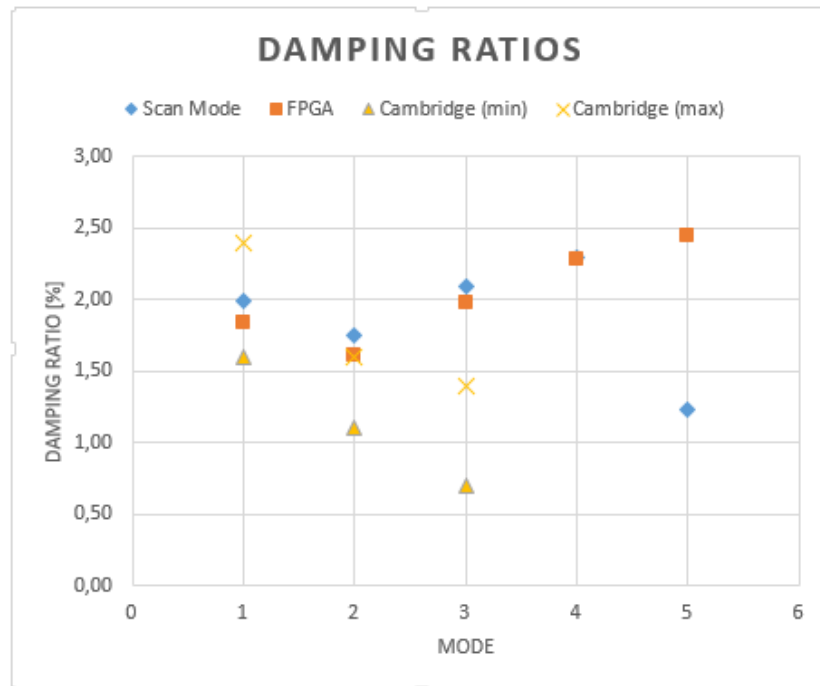


Figure 8.5: Damping ratios of Treet from measurements

The damping ratios are generally higher compared to the estimates from Reynolds et al., except the estimates for mode 1 that fall within their measured interval. Damping estimates within this thesis are likely to better represent reality because the wind excitation was significantly higher [25].

The damping used in SWECOs model was assumed to be 1.9% and was a highly uncertain parameter. The number 1.9 was based upon damping ratios for timber bridges. Engineering judgement led to using the same damping ratio in Treet. Results from the measurements carried out in this thesis show that for mode 1, the actual value is lower, but close, at 1.84%. In mode 2, the damping is lower at about 1.61% while it increases again to mode 3 at 1.98%. The sudden drop in damping ratio for mode 5 from scan mode is considered non-physical. This is because FPGA utilizes the equipment in a more accurate way than scan mode and it is assumed that ξ_5 is indeed physical for FPGA.

8.3 Uncertainties

There are some uncertainties in the measurements that may somewhat affect the results, but it is assumed that the results are sufficiently accurate. On the first day of measurements in Bergen and Moholt the sampling rate was highly uncertain, while the second measurements performed, using FPGA, at both Treet and Moholt 50|50 seemed to have stable sampling rates. However, no way to timestamp every data point on the writing end of the FIFO was found. Instead, every 280th sample was timestamped in the host VI. By nature, it is expected that jitter occurs on the reading end of the FIFO. On average, the time between every 280th sample was stable. See Appendix B.2.3 for details.

While the Cov-SSI is an accurate way of converting the acceleration data into dynamic properties, there are some variables within the method that may affect the results. Lengths of each time series affect the accuracy and scatter of the results, and the lengths chosen for each analysis have empirically been shown to provide sufficiently accurate results. The natural frequencies estimates seem to exhibit little variation for different number of blockrows, while the damping estimates are more sensitive. The number of blockrows chosen for each measurement are chosen through an iterative process in order to produce the clearest stabilization diagrams.

Another uncertainty is the equipment; both the accelerometers and the wires introduce some noise in the results. Also, the PCB accelerometers have fluctuating low-frequency components. This is likely from to occur from the IEPE power source, and it produces high energy noise between 0 and 0.5Hz. However, these frequency components are much lower than any of relevant natural frequencies. In general, the PCBs exhibited a lot more noise than the Kistlers. Both accelerometer models exhibited measurement noise that increased response amplitudes within the considered frequency bands. See Appendix C.5 for more details.

The way the accelerometers were fastened to the structural system may somewhat have affected the results. The orientation of each accelerometer might not have been perfectly aligned because they were mounted by eye. This will affect the resulting mode shapes, but the effect is assumed to be minimal and the resulting mode shapes are assumed to be sufficiently accurate. In addition, this does not significantly affect the resulting natural frequencies and damping ratios.

At Moholt, the structural response was mainly due to construction work and not wind. This makes the results more uncertain as the load input is not comparable to the fundamental white noise input assumption made by Cov-SSI.

Chapter 9

Conclusions

The overall feedback of the measurements and results presented in this thesis shows that numerical models predict the structural behaviour sufficiently well. However, the numerical models can not be completely accurate when estimating dynamic properties, such as the natural frequencies of the buildings. This seems to be the case because non-structural effects are difficult to incorporate in the numerical models, while they seem to contribute to the overall structural behaviour.

Measuring vibrations the way it is proposed in this thesis has proven to provide a lot of information regarding the structural behaviour of tall timber buildings. However, it is important to be in complete control of the data flow all the way from induced voltages to the digital numbers that are logged to disk. Going into depth of the theory behind OMA has been important in order to interpret and evaluate the results. The work has been very interesting and will hopefully be helpful in further research regarding the dynamic properties of tall timber buildings.

9.1 Further Work

It is expected that the positive development in timber structures will continue over the years to come. A big challenge will be to convince investors to build both more and taller with timber. A project at the department for timber structures at NTNU is currently under way, and aims to produce a design basis for mass production timber buildings between 5 to 10 stories [25]. A similar methodology to what has been presented in this thesis can be used to evaluate those buildings in the future.

It will be interesting to see if someone else would get the same results as the ones presented in this thesis. The results here are believed to be accurate, but more measurements at different levels of wind excitation will be of interest. This applies both to Moholt 50|50 and Treet, but it will be especially interesting at Moholt 50|50 as it

9 CONCLUSIONS

has only been measured at low levels of wind excitation. Also, it might be interesting, if possible, to measure the acceleration response in the residential modules in Treet. In addition to Moholt 50|50 and Treet, a number of different tall timber buildings in Norway and around the world are planned for the future, with heights exceeding that of Treet. Measuring vibrations at these new buildings will contribute to better understand the dynamic properties of tall timber buildings. It would also be interesting to further develop the equipment to be placed at structures over longer time periods, where internet communication with the Real-Time target is utilized. Measurements for different wind conditions will be easier to achieve if planning according to something as arbitrary as the weather could be circumvented.

At the moment, a large timber skyscraper is being planned in London, England [11]. It is planned to be 300 meters tall, and all the main structural components will possibly be made out of timber. This size of timber structures have never been seen before, and it will therefore be a building that is going to be extremely relevant to investigate, if it is ever realized. Especially, it will be interesting to see how well it performs regarding the acceleration problems that seem to be something like an Achilles heel for tall timber buildings.



Figure 9.1: Proposed 300 meters tall timber skyscraper

Bibliography

- [1] Discrete fourier transform in matlab. <http://se.mathworks.com/help/matlab/math/discrete-fourier-transform-dft.html>. Accessed: 14-05-2016.
- [2] Fft in matlab. <http://se.mathworks.com/help/matlab/ref/fft.html>. Accessed: 08-06-2016.
- [3] Fft-shift in matlab. <http://se.mathworks.com/help/matlab/ref/fftshift.html>. Accessed: 08-06-2016.
- [4] Google maps. <https://www.google.no/maps/>. Accessed: 04-06-2016.
- [5] Hanning window in matlab. <http://se.mathworks.com/help/signal/ref/hann.html>. Accessed: 25-05-2016.
- [6] Matlab's built-in butterworth filter design. <http://se.mathworks.com/help/signal/ref/butter.html>. Accessed: 27-05-2016.
- [7] Resample function with built-in anti-aliasing filter in matlab. <http://se.mathworks.com/help/signal/ref/resample.html>.
- [8] Welch's method in matlab. <http://se.mathworks.com/help/signal/ref/cpsd.html>. Accessed: 25-05-2016.
- [9] Zero-phase digital filtering in matlab. <http://se.mathworks.com/help/signal/ref/filtfilt.html>. Accessed: 08-06-2016.
- [10] Jarle Aarstad, Geir Glasø, and Aasmund Bunkholt. Massivtre. *FOKUS på tre*, 43, 2007.
- [11] PLP architecture. Plp architecture. <http://www.plparchitecture.com>. Accessed: 2016-06-08.
- [12] Daryl Boggs. Acceleration indexes for human comfort in tall buildings—peak or rms. *CTBUH monograph*, 1997.
- [13] Andrew H Buchanan and S Bry Levine. Wood-based building materials and atmospheric carbon emissions. *Environmental Science & Policy*, 2(6):427–437, 1999.

BIBLIOGRAPHY

- [14] Ario Ceccotti, Carmen Sandhaas, Minoru Okabe, Motoi Yasumura, Chikahiro Minowa, and Naohito Kawai. Sofie project–3d shaking table test on a seven-storey full-scale cross-laminated timber building. *Earthquake Engineering & Structural Dynamics*, 42(13):2003–2021, 2013.
- [15] Daniel Gsell, Glauco Feltrin, Sandy Schubert, Rene Steiger, and Masoud Motavalli. Cross-laminated timber plates: evaluation and verification of homogenized elastic properties. *Journal of Structural Engineering*, 133(1):132–138, 2007.
- [16] Ola Hansen. Dynamic properties of the worlds tallest timber building. Semester project, 2015.
- [17] National Instruments. Getting started with compactrio - logging data to disk. <http://www.ni.com/tutorial/11198/en/>. Accessed: 2016-05-23.
- [18] National Instruments. Setting up ethercat on ni programmable automation controllers. <http://www.ni.com/white-paper/10555/en/>. Accessed: 2016-05-23.
- [19] ISO ISO. 10137: Bases for design of structures-serviceability of buildings and walkways against vibrations. *International Standard Organisation (ISO)*, 2007.
- [20] Kistler. *K-Beam® Accelerometer Capacitive MEMS, Triaxial Accelerometer Type 8395A...* Accessed: 2016-05-23.
- [21] Erwin Kreyszig. *Advanced engineering mathematics*. John Wiley & Sons, 2010.
- [22] Gerard Lallement and Daniel J Inman. A tutorial on complex eigenvalues. In *PROCEEDINGS-SPIE THE INTERNATIONAL SOCIETY FOR OPTICAL ENGINEERING*, pages 490–490. SPIE INTERNATIONAL SOCIETY FOR OPTICAL, 1995.
- [23] Knut Einar Larsen and Nils Marstein. Conservation of historic timber structures. an ecological approach. 2016.
- [24] KA Malo, RB Abrahamsen, and MA Bjertnæs. Some structural design issues of the 14-storey timber framed building “treet” in norway. *European Journal of Wood and Wood Products*, 74(3):407–424, 2016.
- [25] Kjell Arne Malo. Personal Communication.
- [26] Gerard A Meehl, Thomas F Stocker, William D Collins, Pierre Friedlingstein, Amadou T Gaye, Jonathan M Gregory, Akio Kitoh, Reto Knutti, James M Murphy, Akira Noda, et al. Global climate projections. *Climate change*, 3495:747–845, 2007.
- [27] Russell C Moody and Roland Hernandez. Glued-laminated timber. *Forest Product Laboratory. USDA Forest Service. Madison, Winconsin*, 1997.

- [28] National Instruments. *NI 9234 Data Sheet*. Accessed: 2016-05-23.
- [29] National Instruments. *SPECIFICATIONS NI cRIO-9067 Embedded Real-Time Controller with Reconfigurable FPGA for C Series Modules*. Accessed: 2016-05-23.
- [30] Standard Norge. Ns-en 1991-1-4: 2005+ na: 2009: Eurokode 1: Laster på konstruksjoner, del 1-4: Allmenne laster, vindlaster, 2009.
- [31] Standard Norge. Ns-en 14080:2013: Trekonstruksjoner - limtre og limt laminert heltre - krav, 2013.
- [32] A Øvrum and E Skaug. Konstruksjonsvirke. *FOKUS på tre*, 43, 2007.
- [33] PCB Piezotronics. *Model 356A16 Platinum Stock Products; Triaxial, high sensitivity, ceramic shear ICP® Installation and Operating Manual*, rev. b edition. Accessed: 2016-05-23.
- [34] PCB Piezotronics. Introduction to piezoelectric accelerometers. http://www.pcb.com/techsupport/tech_accel. Accessed: 2016-05-26.
- [35] Carlo Rainieri and Giovanni Fabbrocino. Operational modal analysis of civil engineering structures. Technical report, Springer, 2014.
- [36] Edwin Reynders, Rik Pintelon, and Guido De Roeck. Uncertainty bounds on modal parameters obtained from stochastic subspace identification. *Mechanical Systems and Signal Processing*, 22(4):948–969, 2008.
- [37] Thomas Reynolds, Rob Foster, and Michael Ramage. Dynamic properties of treet. Technical report, University of Cambridge, 12 2015.
- [38] Thomas Reynolds, Richard Harris, Wen-Shao Chang, Julie Bregulla, and Jonathan Bawcombe. Ambient vibration tests of a cross-laminated timber building. *Proceedings of the Institution of Civil Engineers-Construction Materials*, 168(3):121–131, 2015.
- [39] A. Rönnquist. *Pedestrian induced lateral vibrations of slender footbridges*, 2005.
- [40] Dassault Systèmes Simulia. Abaqus/cae user’s manual. *Providence, RI*, 2007.
- [41] SiT. Studentsamskipnaden i Trondheim. Brochure, 2014.
- [42] Cameron Stauder. Cross-laminated timber. *An analysis of the Austrian industry and ideas for fostering its development in America. Itävalta: Fachhochschule salzburg: university of applied sciences. Saatavissa: http://www.marshallplan.at/images/papers_scholarship/2013/StauderCameron_2013.pdf. Hakupäivä*, 4:2015, 2013.

BIBLIOGRAPHY

- [43] Einar Strømmen. *Theory of bridge aerodynamics*. Springer Science & Business Media, 2010.
- [44] Sweco. Verdens høyeste trehus: Et innovativt og bærekraftig bygg. <http://www.sweco.no/prosjekt-container/verdens-hoyeste-trehus-et-innovativt-og-barekraftig-bygg/>. Accessed: 2016-05-22.
- [45] Ingunn Utne. Numerical models for dynamic properties of a 14 storey timber building. Master's thesis, NTNU, Norway, 2012.
- [46] Joachim Von Zur Gathen and Jürgen Gerhard. *Modern computer algebra*. Cambridge university press, 2013.
- [47] Wikipedia. Burj khalifa. https://en.m.wikipedia.org/wiki/Burj_Khalifa. Accessed: 2016-05-22.
- [48] Wikipedia. Timber framing. https://en.wikipedia.org/wiki/Timber_framing. Accessed: 2016-05-19.
- [49] yr.no. yr.no - bergen - været som var - datosøk. <http://www.yr.no/sted/Norge/Hordaland/Bergen/Bergen/almanakk.html?dato=2016-04-19>. Accessed: 2016-05-23.
- [50] yr.no. yr.no - bergen - været som var - datosøk. <http://www.yr.no/sted/Norge/Hordaland/Bergen/Bergen/almanakk.html?dato=2016-05-02>. Accessed: 2016-05-23.

Appendix A

Moholt 50|50

In this chapter, the measurement layouts, results obtained from the time series and discussion of some key aspects is included.

Moholt 50|50 is an ongoing project initiated by Studentsamskibnaden i Trondheim (SiT). It is the largest project in Norway where the main structural systems are made out of CLT. Five nine-storey towers will include 632 student dorms and some business areas in the ground floors [41].

In this thesis, accelerations were measured over two operations, "Moholt One" and "Moholt Two". Moholt One was performed with little knowledge about measuring vibrations, and gave mostly qualitative results along with motivation for a second visit to Moholt 50|50. Moholt Two gave better results due to better weather conditions and better measurement files.

The accelerometer recordings were obtained for two methods of structure excitation. Method One brought people to the top floor. They were asked to step from side to side at different frequencies using a metronome. One stepping period lasted one beat. Within a beat, each person stepped from one side to the other and back. When the input frequency was getting closer to a natural frequency of the structure, it was possible to feel the entire structure shaking. The second method acquired longer time series, where environmental loads were the dominating input force.

The measurement files were too big to include into the digital appendix, and were given to supervising professor Kjell Arne Malo on a memory stick [25].

A.1 System Layouts

The presentation of results are related to the global axis system on the right in figure A.1. Not all accelerometers were aligned with this global coordinate system. Depending

on the orientation of each accelerometer during each recording, the raw data of each channel has to be scaled by -1 or 1 . The scaling factors for each channel for Moholt One and Moholt Two can be found in tables A.1 and A.3 respectively. Due to the 25° kink in the facade where the measurements were taken, the time series on the eastern side have been decomposed into time series following the global coordinate system. After the latter scaling factors have been applied, accelerations in the global coordinate system for the eastern accelerometers can be obtained through the following relationships:

$$X_G = X_L \cdot \cos(25^\circ) + Z_L \cdot \sin(25^\circ) \quad (\text{A.1})$$

$$Z_G = Z_L \cdot \cos(25^\circ) - X_L \cdot \sin(25^\circ) \quad (\text{A.2})$$

Figure A.1 shows the local coordinate systems of the raw data, input positions and directions for excitation Method 1, and the global coordinate system used to present the results.

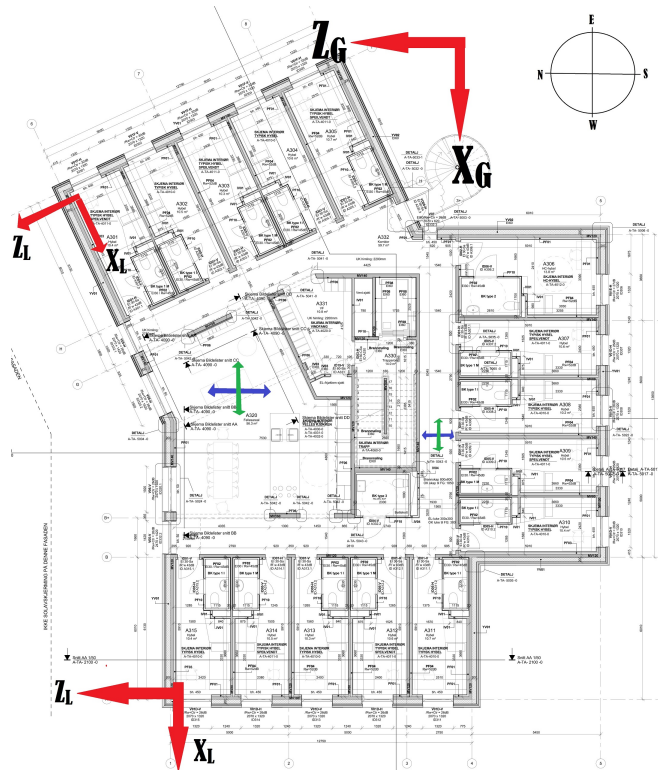


Figure A.1: Moholt 50|50 Layout

This was done to ensure a better representation of the mode shapes. Raw data following the local coordinate system of each accelerometer can be found in the digital appendix.

A.1. SYSTEM LAYOUTS

The green and blue crosses indicate the input positions and directions for excitation Method 1.

On both operations, the cables reaching out to the western accelerometers were 10m coaxial cables from the accelerometer manufacturers. The eastern accelerometers used 10m coaxial cables from their manufacturer+20m home made coaxial extension cables.

A.1.1 Moholt One System Layout Specifics

The given access on the construction site allowed for the accelerometers to be mounted close to the ceiling in the 9th floor and close to the floor in the 7th floor. During Moholt One, voltages were directly converted into m/s^2 inside the VI. The sampling rate was originally set to 1000Hz in scan mode. The measurement file used for method 1 and method 2 are *150bpm-andregang.tdms* and *MoholtEnvironmental1.tdms* respectively. Table A.1 relates the measured data for each accelerometer at their respective positions to the local coordinate systems in Figure A.1:

Floor	Channel	Direction	Scaling Factor	Sensor Position	Accelerometer
9	1	Z	-1	E	Kistler
9	2	X	1	E	Kistler
7	3	Z	-1	E	Kistler
7	4	X	1	E	Kistler
7	5	X	1	W	PCB
7	6	Z	-1	W	PCB
9	7	X	-1	W	PCB
9	8	Z	-1	W	PCB

Table A.1: Relation between measurement files and local coordinate systems

The PCB accelerometers only utilized cables from their producers, while the Kistlers utilized cables from their producers along with coaxial extension cables. See Section D.2 for details.

The mode shape vector entries detected during Moholt One relates to the entries in Figure A.2:

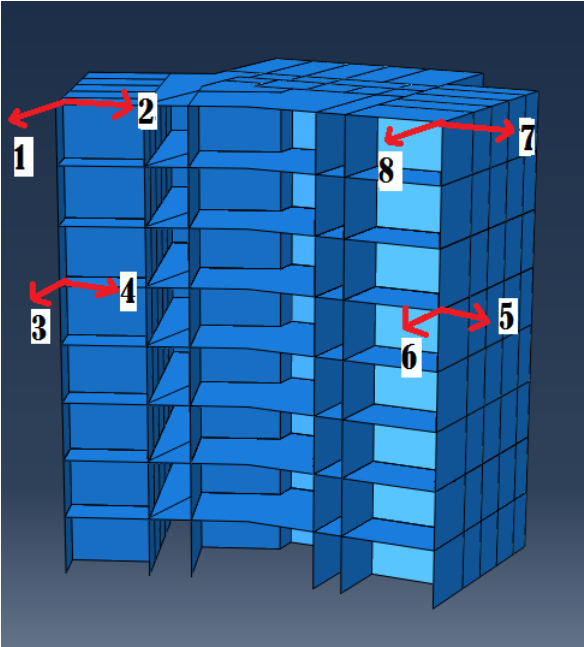


Figure A.2: Position and direction of each vector entry in the detected mode shapes in the global coordinate system

A.1.2 Moholt Two System Layout Specifics

The given access to tower A allowed for measurements to be taken close to the ceiling in the 9th floor along the equivalent facade used during Moholt One. Kistler accelerometers were used, and measured voltages were not converted to m/s^2 inside the VI. The voltages have to be scaled by the scaling factor 4.905 found in table D.1. The sampling rate was set to 1652Hz using FPGA. Measurement file names of excitation method 1 and method 2 are found in Table A.2. In *LangMaaling.tdms*, samples 36e6 to 48e6 are used and correspond to the samples gathered from approximately 7pm to 9pm.

Excitation Method	File name	Input
1	shakeNorthX.tdms	X-North
1	shakeNorthZ.tdms	Z-North
1	shakeSouthX.tdms	X-South
1	shakeSouthZ.tdms	Z-South
2	ForsteMaaling.tdms	Wind + Construction Activity
2	LangMaaling.tdms	Wind

Table A.2: File names and inputs of Moholt Two

The western accelerometers only utilized cables from their producers, while the western

A.1. SYSTEM LAYOUTS

utilized coaxial extension cables as well. See Section D.2 for details.

A Two hour measurement was recorded with activity on site, and an overnight recording was performed without activity on site. When there was no activity on site, the tape holding the cable for the western accelerometer had loosened some time during the recording. The next morning, the accelerometer had turned approximately 135° about the local Z-axis. The time series in Figure A.3 show a huge acceleration peak in channels 1 and 2 about one hour into the recording, and seem likely to be the incident when the accelerometer fell out of its intended alignment relative to the global X-axis.

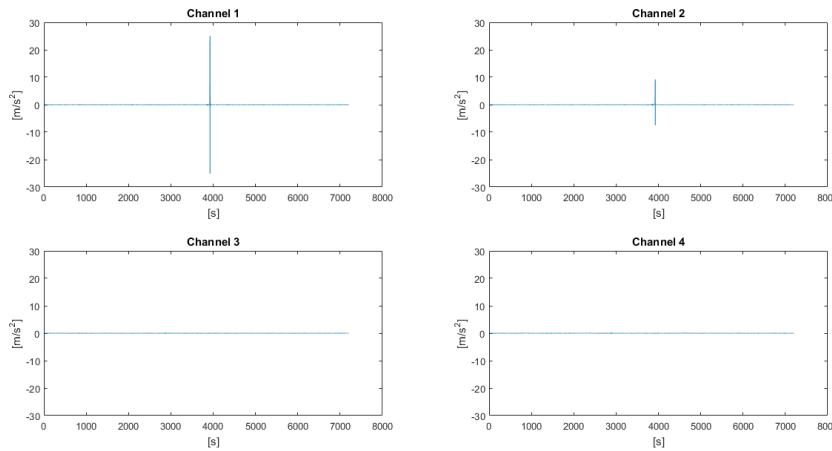


Figure A.3: Two first two hours of overnight recording during Moholt Two

Table A.3 relates measurement files from Moholt Two to the local coordinate systems in Figure A.1:

Floor	Channel	Direction	Scaling Factor	Sensor Position	Accelerometer
9	1	X	-1	W	Kistler
9	2	Z	1	W	Kistler
9	3	X	-1	E	Kistler
9	4	Z	1	E	Kistler

Table A.3: Relations between measurement files and local coordinate systems

The mode shape vector entries detected during Moholt Two relates to the entries in the figure below

Figure A.4 shows how each vector entry in the detected mode shapes relates to the global coordinate system proposed in Figure A.1:

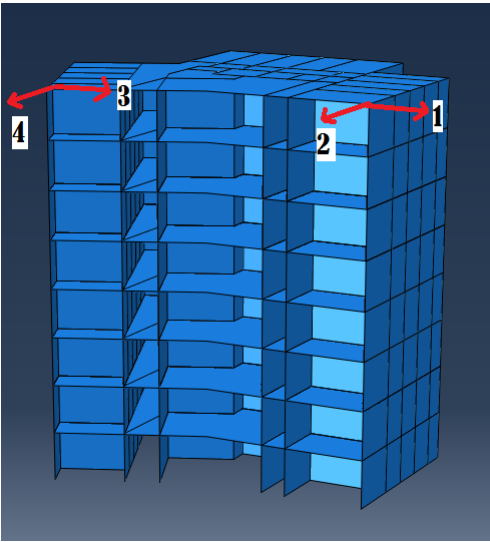


Figure A.4: Position and direction of each vector entry in the detected mode shapes in the global coordinate system

A.2 Moholt One Results

Method One brought four people to the top floor. The biggest response amplitudes were recorded when the metronome was set to 150 beats per minute (bpm). Measurements were only taken when the main input direction was in the global Z-direction at the northern spot indicated in figure A.1.

The VI was never debugged in LabVIEW using any form of sampling timestamps and the source(s) of error causing the huge drop in sampling rate was never identified. The approximated sampling rate is used to create a time axis for plots of Method One, and an assumption used to identify the frequency of potentially activated modes during the recordings.

A.2.1 Method 1 - Results

Maximum Acceleration and Dynamic Displacements

The data was downsampled from 700Hz to 70Hz. Then it was lowpassed at 4.375Hz and highpassed at 0.44Hz after each numerical integration.

A.2. MOHOLT ONE RESULTS

Channel	Max. Acc. [mm/s^2]	Max. Displ. [mm]
1	60,9663	0,5946
2	28,1048	0,4263
3	46,1013	0,4441
4	23,8152	0,2836
5	103,1025	1,2003
6	57,6193	0,7025
7	51,8827	0,4016
8	22,6078	0,2191

Table A.4: Max. Acc. and Max. Dyn. Displ. from Moholt One, Method 1

The acceleration time series look the following:

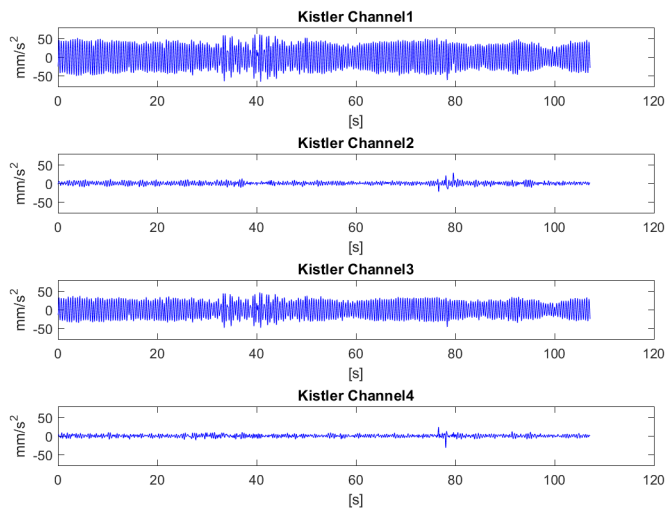


Figure A.5: Acceleration time series of the Kistler accelerometers

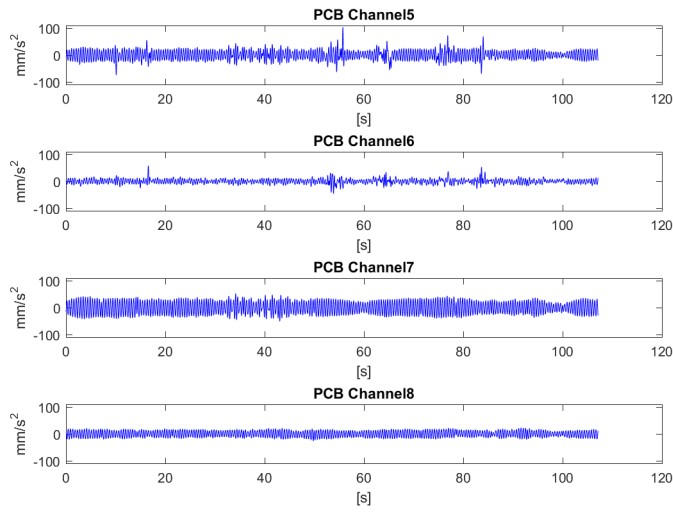


Figure A.6: Acceleration time series of the PCB accelerometers

The resulting dynamic displacement time series are:

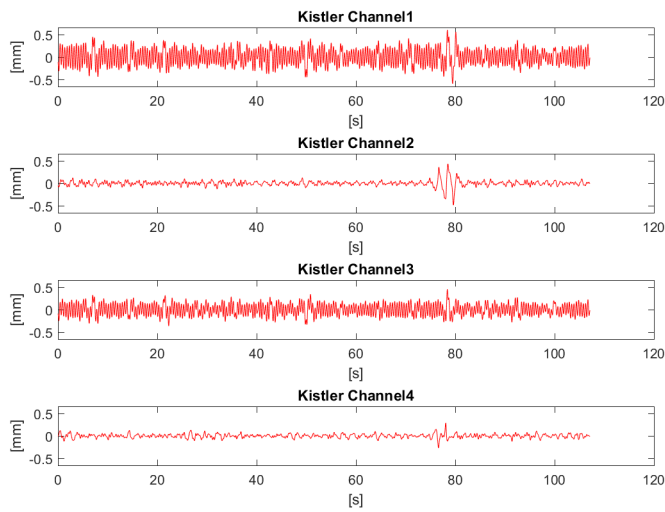


Figure A.7: Displacement time series of the Kistler accelerometers

A.2. MOHOLT ONE RESULTS

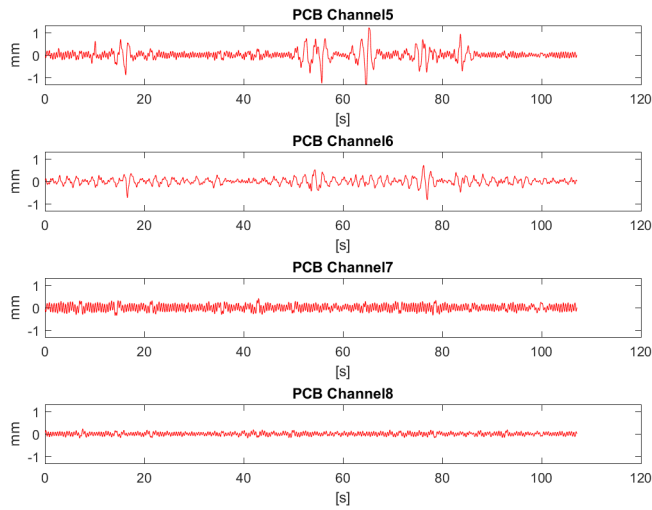


Figure A.8: Displacement time series of the PCB accelerometers

Channels 1 and 5 show the largest acceleration response amplitudes at each side of the building, which makes sense considering the input loading was mainly in the global Z-direction. The largest peak acceleration was detected by channel 5. Maximum dynamic displacement was also obtained from channel 5.

Auto Power Spectral Densities

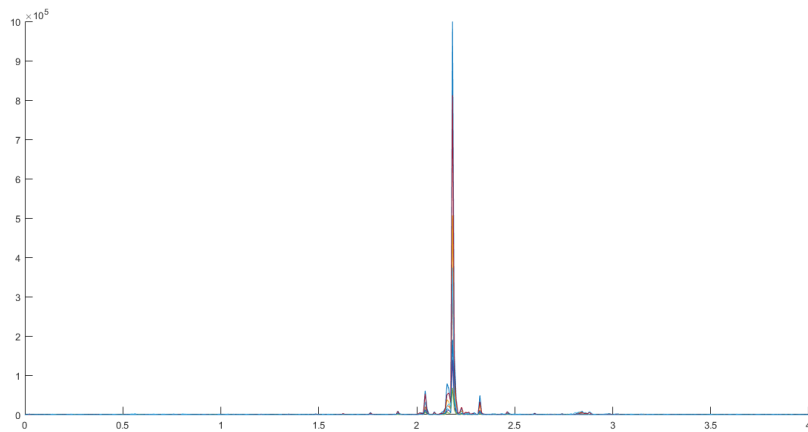


Figure A.9: APSD Moholt One

The tallest peak would be expected to land at 2.5Hz because this is the dominating input frequency on the system. Assuming the sampling frequency was 698Hz, it landed at 2.182Hz. Two other peaks occur at about 2.034Hz and 2.322Hz and indicate that some of the response consist of other distinct frequency components. A lot of uncertainty is present in this experiment. Scatter in rhythmic sense of the people in the top floor makes the input frequency uncertain. Detected frequency components are uncertain due to the uncertain sampling frequency.

A.2.2 Method 2 - Results

Time series recorded by the PCB accelerometers show seemingly non-physical behaviour with large sudden jumps or drops with no following oscillations within the same magnitude. An example of this behaviour is shown below:

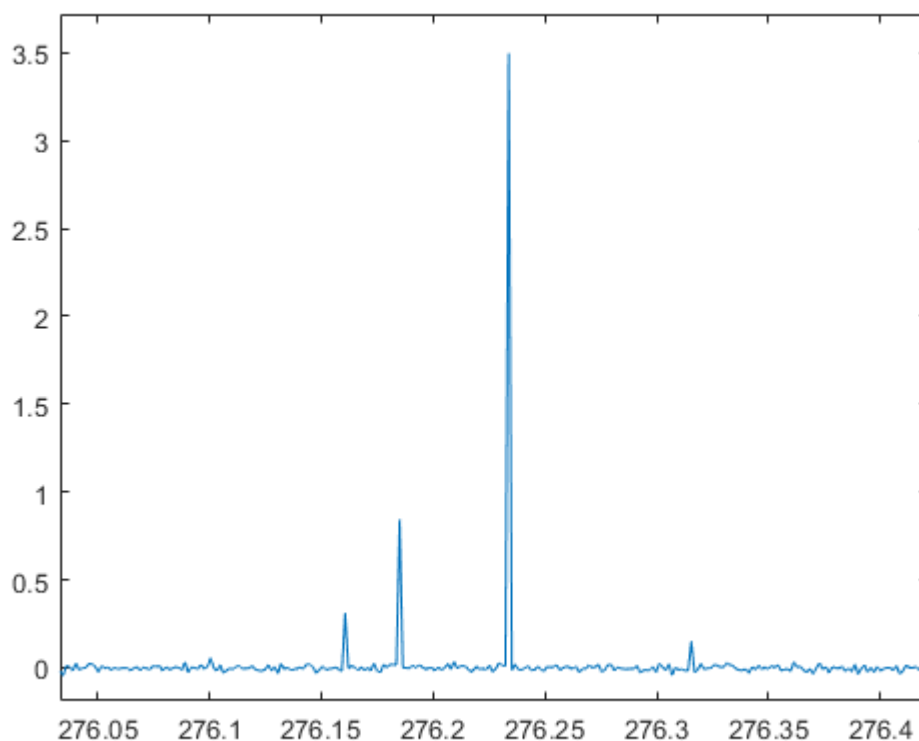


Figure A.10: Peaks considered non-physical with respect to structural behaviour.

The behaviour is indeed of high frequency and should go away after lowpassing the signal. A better picture of the mode shapes could probably have been extracted by including the PCB accelerometers. However, the PCB accelerometers are not as sensitive

A.2. MOHOLT ONE RESULTS

as the Kistlers, and because of the low excitation levels they have been left out of the analysis.

Weather data recorded about one kilometre away at Voll weather station indicates that the highest mean wind speed during the time of the recording was never more than $3.7m/s$ and the largest gusts were about $6.1m/s$. See "Vind_Moholt1.xls" in the digital appendix for details. Very little excitation was recorded, so the time series used to present the results are from while there was activity on site. The VI used to record the time series was a relatively complicated VI. It was created with little concern about even sampling rates and jitter effects, and provided mostly measurements of noise. The sampling frequency is assumed to be 700Hz within this subsection.

Limits on frequency and damping used to extract natural frequencies and damping ratios from Cov-SSI is shown in table A.5.

Mode	f_n range [Hz]	ξ range [%]
1	2.14-2.23	2-8
2	2.44-2.51	2.12
3	2.75-2.83	2-12

Table A.5: Limits on frequency and damping for Moholt One

Natural Frequencies

Mode	fn from APSD	Mean f_n from Cov-SSI	σ_{f_n}
1	2.217	2.185	1.51e-2
2	2.485	2.480	1.10e-2
3	2.870	2.800	1.50e-2

Table A.6: Natural Frequencies detected during Moholt One

Damping Ratios

Mode	Mean Value of ξ from Cov-SSI	σ_ξ	Orders considered stable
1	5.53	8.53e-1	12 to 146
2	6.07	2.13	20 to 152
3	5.42	7.22e-1	12 to 160

Table A.7: Damping ratios for Moholt One

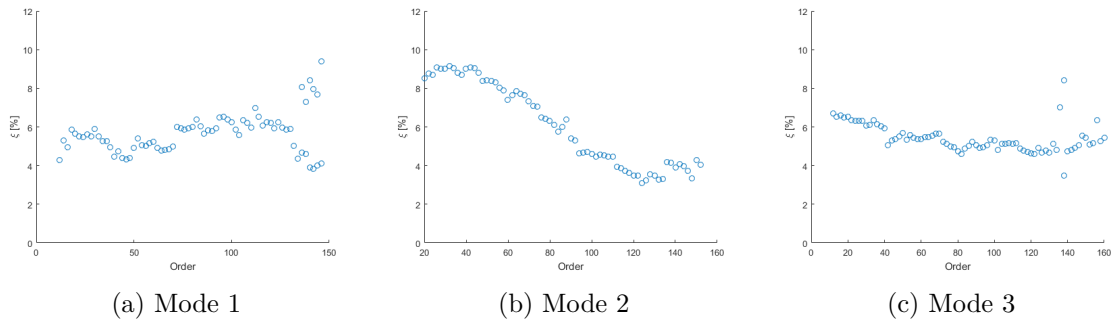


Figure A.11: Scatter of Damping Estimates

Damping estimates for mode 1 show quite a lot of variation, and the estimates for mode 2 seem to decrease for increasing system order. The estimates for mode 3 seem more stable.

Mode Shapes

As discussed at the beginning of this subsection, only the mode shapes detected by the Kistler accelerometers at the eastern side of the building have been included. This makes detection of torsional modes impossible, but the analysis allows detection of a dominant direction in the mode shape.

Entry	Mode 1	Mode 2	Mode 3
1, Z-direction	1.000	-0.157	1.000
2, X-direction	0.546	1.000	0.482
3, Z-direction	0.965	-0.155	0.819
4, X-direction	0.245	0.793	0.492

Table A.8: Relative lengths of each eigenvector

Entry	Mode 1, Z	Mode 2, X	Mode 3, Z
1, Z-direction	-0.428+8.453i	-0.159-0.022i	-1.000+0.821i
2, X-direction	-0.667+4.575i	-1.000+0.223i	-0.601+0.167i
3, Z-direction	-0.276+8.161i	-0.087-0.133i	-0.932+0.505i
4, X-direction	-1.000+1.819i	-0.759+0.291i	-0.580+0.262i

Table A.9: Complex entries of each eigenvector

A.2. MOHOLT ONE RESULTS

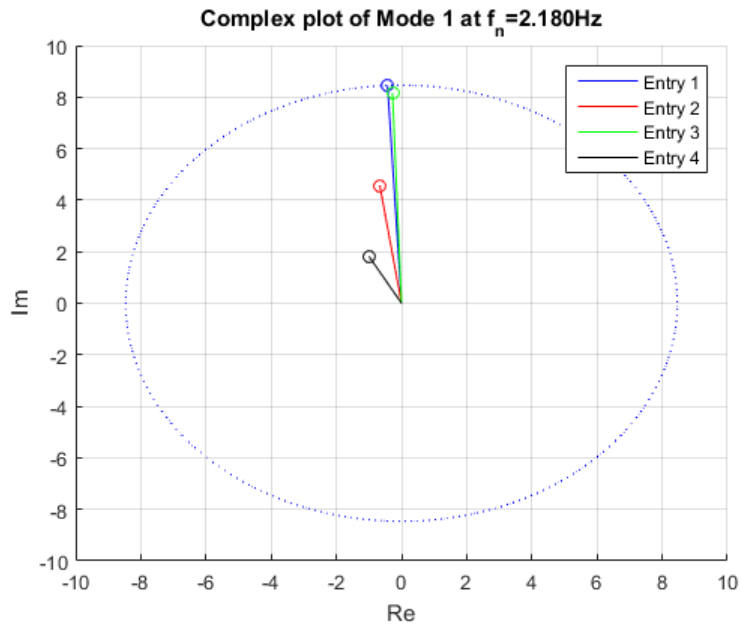


Figure A.12: Mode 1

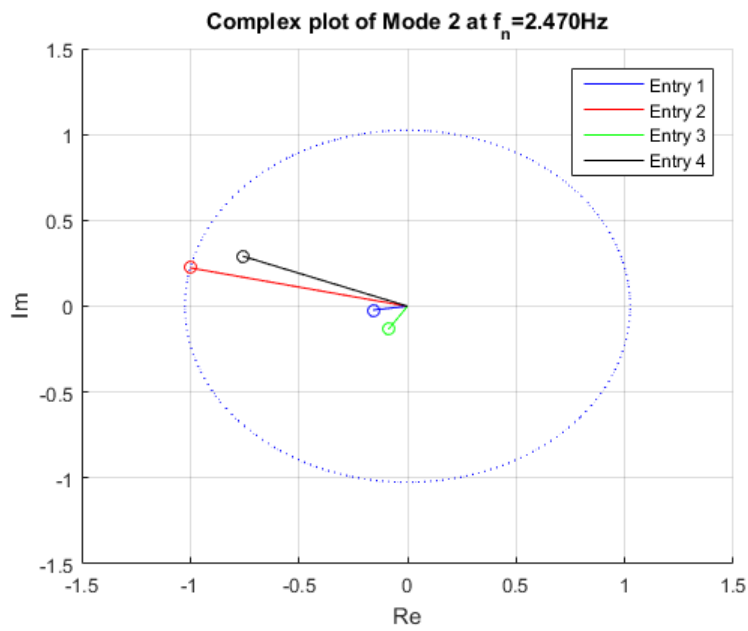


Figure A.13: Mode 2

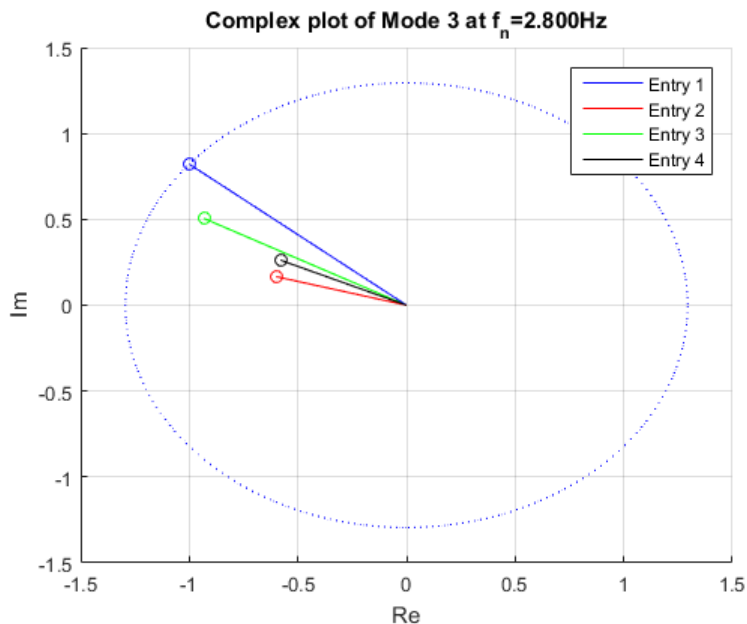


Figure A.14: Mode 3

Mode 1 and 3 seems to have their dominating direction in the global Z-direction, while mode 2 seems to have its dominating direction in the global X-direction.

Auto Power Spectral Densities

The following plot shows the Auto Power Spectral Densities of channel 1 and 2 using Welch's Estimate [8] weighing 60 segments with MatLab's built-in hanning window [5] and 50% overlap between each segment.

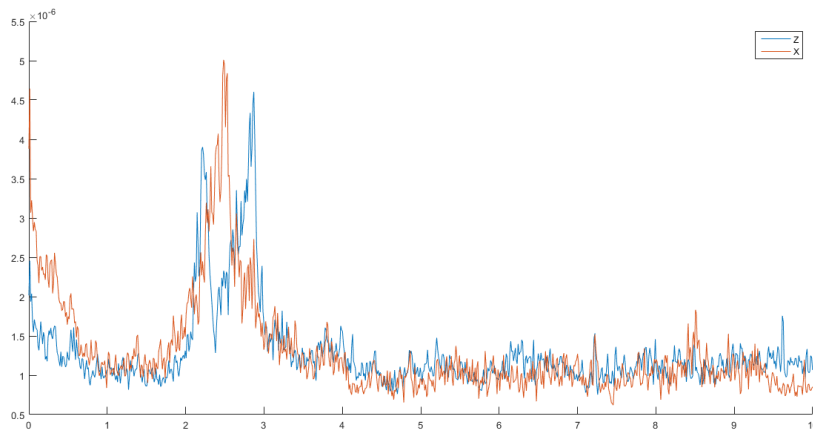
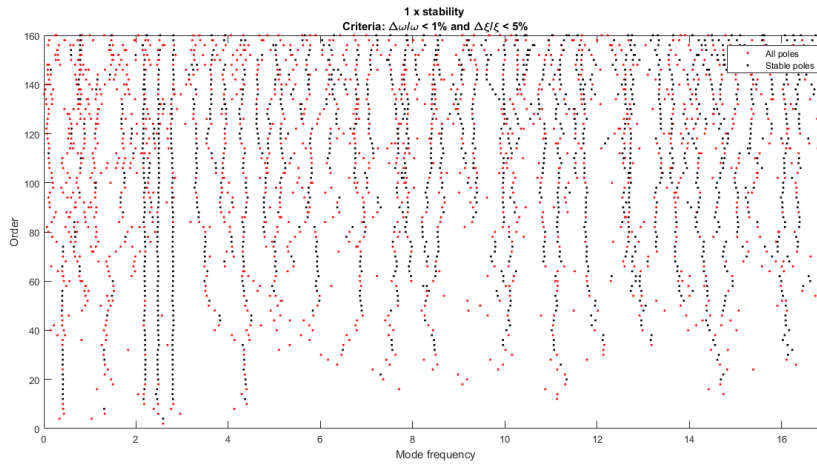


Figure A.15: Auto Power Spectral Density of channel 1 and 2

Stabilization Diagram of Kistler Accerlerometers

The following stabilization diagram has been created after downsampling the signal from 700Hz to 35Hz and using 40 blockrows.



Peak Acceleration and Maximum Dynamic Displacement

The lowpass filter was set to 4.4Hz and the hignpass filter was set to 0.4Hz. The peak accelerations from each time series is shown in Table A.10

Channel	Max. Acc [mm/s^2]	Max Displ [mm]
1	51,52	2,491
2	189,45	2,119
3	115,20	1,361
4	158,19	2,130
5	54,94	0,408
6	74,71	0,966
7	61,63	2,420
8	72,09	1,355

Table A.10: Peak accelerations of each channel during Moholt One, Method 2

The acceleration time series look like the following:

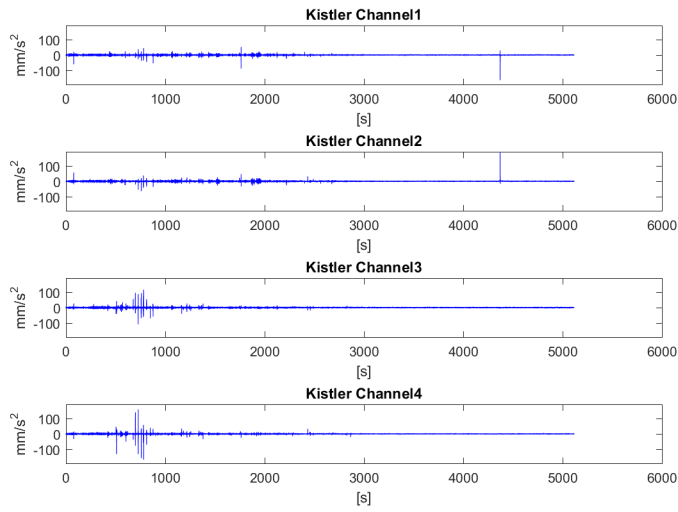


Figure A.16: Acceleration time series of the Kistler accelerometer

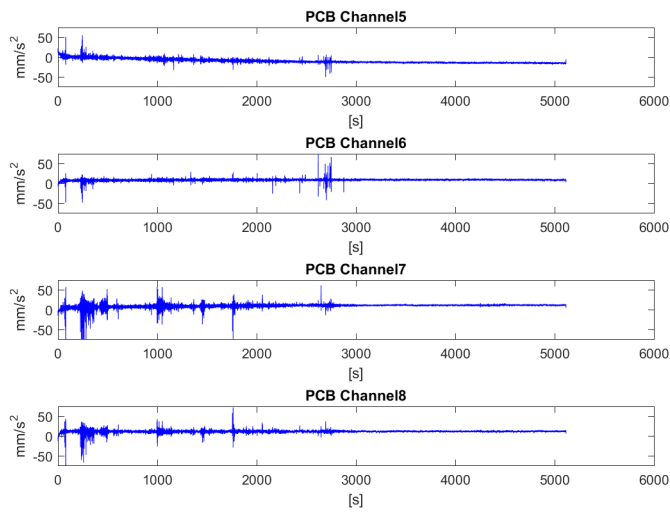


Figure A.17: Acceleration time series of the PCB accelerometers

A.2. MOHOLT ONE RESULTS

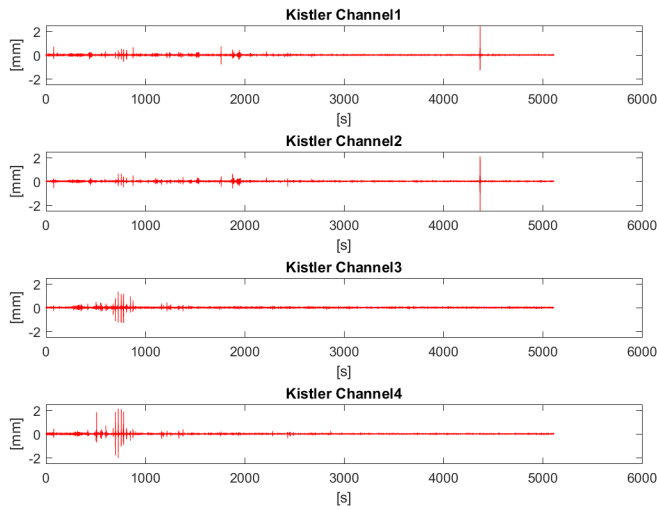


Figure A.18: Dynamic displacement time series of the Kistler accelerometers

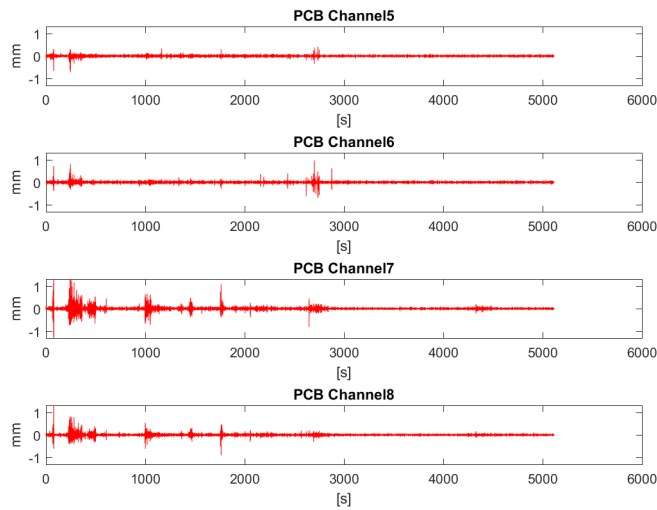


Figure A.19: Dynamic displacement time series of the PCB accelerometers

If an external source had excited the building, it might have been expected to see a response peak at both ends of the building. Instead, each accelerometer seem to react rather locally with large response amplitudes. The peak values are therefore not considered representative for the global system response.

A.3 Moholt Two Results

The approved access on the construction site allowed for measurements to be taken in tower A. Method 1 of excitation was performed by two people. Method 2 of excitation was performed under two different external loading conditions, that is, with and without construction site activity close to the foundation of the building.

A.3.1 Excitation Method 1

Figure A.1 shows two positions in the upper floor, where two people stepped back and forth at 150bpm in the global X and Z-direction.

Auto Power Spectral Densities of all channels

The two plots in figure A.20 shows the auto power spectral densities of all channels for input the global X-direction and Z-direction. The first column are APSDs for inputs on the northern side and the second column are inputs on the southern side. Row 1 is X-direction, and row 2 is the Z-direction.

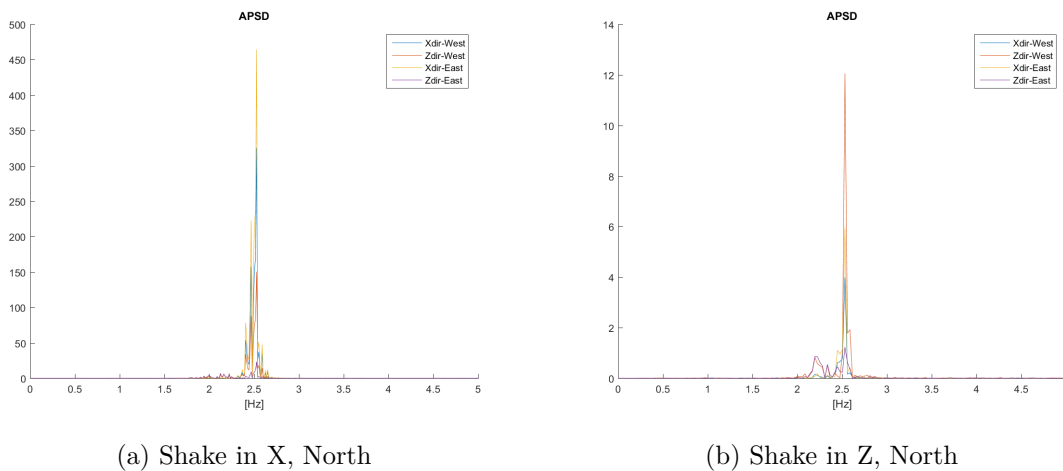


Figure A.20: APSDs for Moholt Two, Method 1

The 2.5Hz frequency component is dominating the measured response in the accelerometers. This is expected, because the input frequency was 2.5Hz. The second eigenmode with dominating translational component in the global X-direction does also have its eigenfrequency at about 2.5Hz (see table A.13). When the excitation force was applied to the main Z-direction, the APSDs show that other frequency components play a greater role in the total measured response. Note that the time series are of different

A.3. MOHOLT TWO RESULTS

length, hence a comparison of the power of each plot in figure A.20 does not make sense before they are normalized.

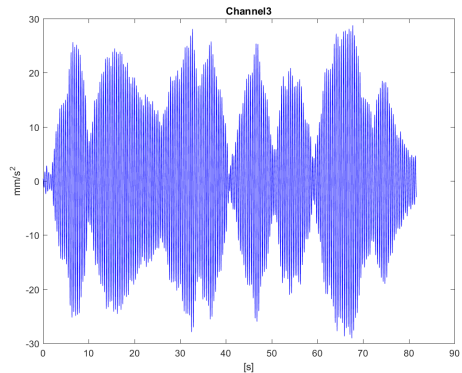
Peak Acceleration and Maximum Dynamic Displacement

The lowpass filter was set to 3.75Hz, and the highpass filter was set to 0.436Hz. Table A.11 shows the representative maximum acceleration recorded from each time series:

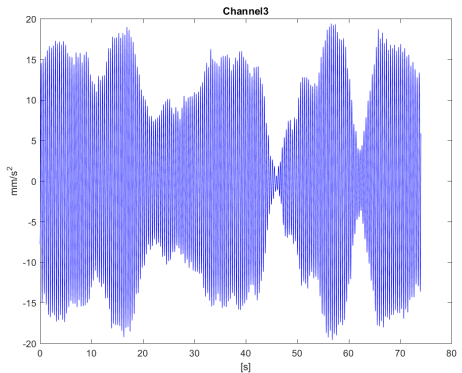
Input Position	Input Direction	Peak Acceleration[mm/s^2]	Peak Dynamic Displacement[mm]
North	X	28.77	0.1615
North	Z	6.967	0.0551
South	X	19.40	0.1326
South	Z	18.62	0.1204

Table A.11: Maximum detected peak acceleration and dynamic displacements

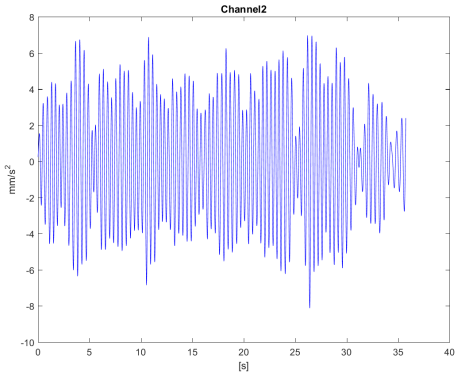
Figures A.21 and A.22 show the channels experiencing the maximum accelerations and dynamic displacements:



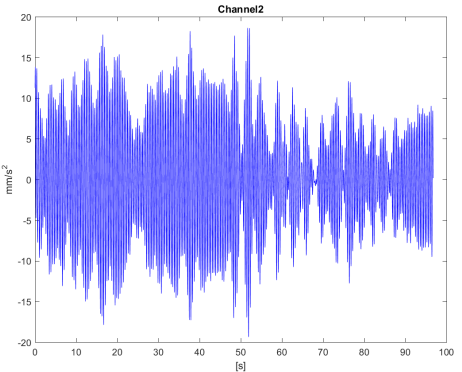
(a) Shake in X, North



(b) Shake in X, South



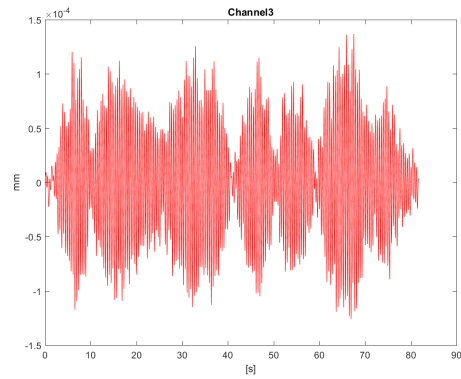
(c) Shake in Z, North



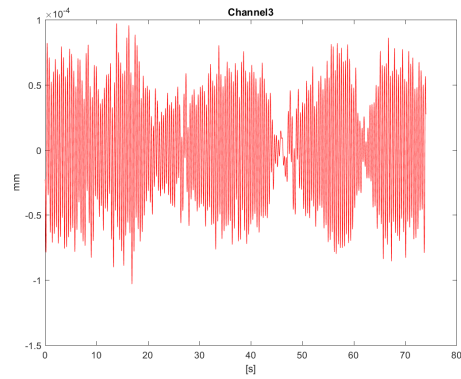
(d) Shake in Z, South

Figure A.21: Peak acceleration time series of Moholt Two, Method 1

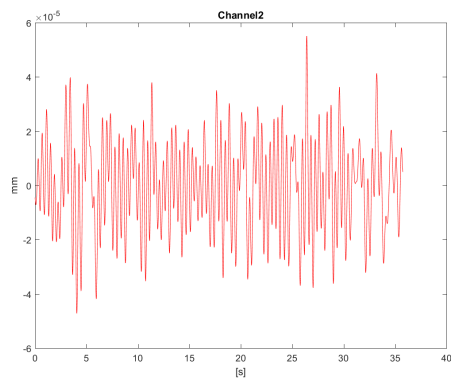
A.3. MOHOLT TWO RESULTS



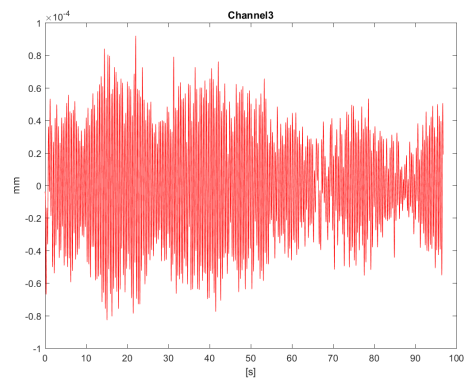
(a) Shake in X, North



(b) Shake in X, South



(c) Shake in Z, North



(d) Shake in Z, South

Figure A.22: Peak dynamic displacement time series of Moholt Two, Method 1

A.3.2 Excitation Method 2, Activity on Construction Site

The time series used to find the following results was recorded between 11am and 1pm on the 24th of May, 2016.

Table A.12 shows the limitations used to extract natural frequencies and damping from Cov-SSI:

Mode	f_n range [Hz]	ξ range [%]
1	2.16-2.20	1-3
2	2.46-2.50	1-3
3	2.75-2.80	1-3
3	6.55-6.65	1-3

Table A.12: Limits on frequency and damping for Moholt Two, Method 2 with Construction Activity

Natural Frequencies

Mode	f_n from APSD	Mean f_n from Cov-SSI	σ_{f_n}	Orders Considered Stable
1	2.183	2.183	4.33e-3	50 to 280
2	2.466	2.483	2.85e-3	66 to 280
3	2.796	2.779	7.76e-3	66 to 280
4	6.582	6.609	7.57e-3	30 to 254
5	(7.532)	-	-	
6	(8.341)	-	-	
7	(12.32)	-	-	
8	(15.19)	-	-	

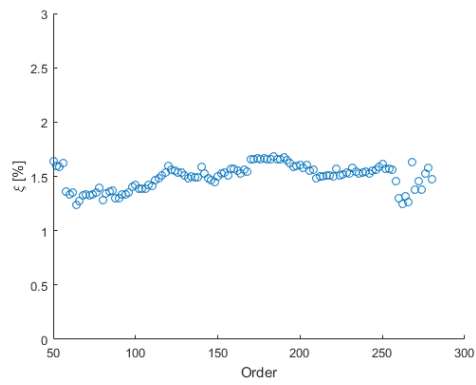
Table A.13: Natural Frequencies from Moholt Two, Method 2 with Construction Activity

Damping Ratios

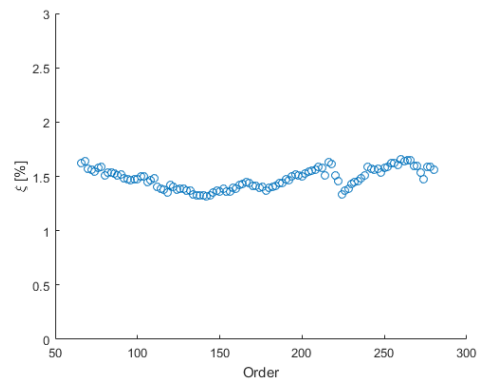
Mode	ξ	σ_{xi}	Orders Considered Stable
1	1.50	1.13e-1	50 to 280
2	1.48	9.31e-2	66 to 280
3	2.05	3.44e-1	66 to 280
4	2.26	9.41e-2	30 to 254

Table A.14: Damping Ratios from Moholt Two, Method 2 with Construction Activity

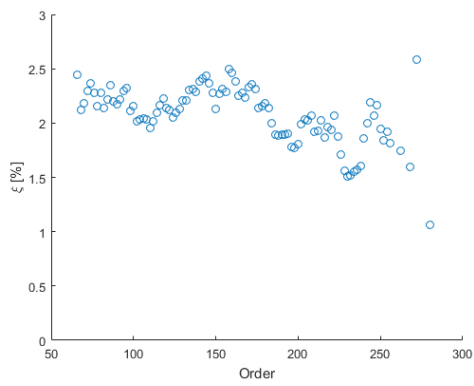
A.3. MOHOLT TWO RESULTS



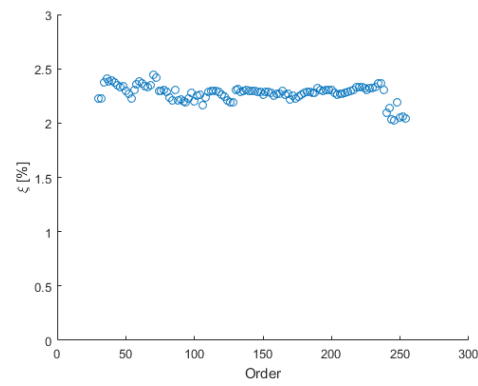
(a) Mode 1



(b) Mode 2



(c) Mode 3



(d) Mode 4

Figure A.23: Scatter of Damping Estimates from Moholt Two, Method 2 with Construction Activity

Mode Shapes

Entry	Mode 1, Z	Mode 2, X	Mode 3, Torsion	Mode 4, Z
1	-0.256	-0.856	-0.183	-0.359
2	-0.910	0.612	1.000	1.000
3	-0.243	-1.000	-0.391	-0.211
4	-1.000	-0.216	-0.901	-0.750
Order	134	144	186	162
Cov-SSI Mode Number	8	9	12	20

Table A.15: Relative lengths of each mode shape entry

Entry	Mode 1, Z	Mode 2, X	Mode 3, Torsion	Mode 4, Z
1	-0.255-0.050i	0.842-2.271i	-0.126-0.162i	0.363-0.033i
2	-0.905-0.186i	-0.696+1.584i	-1.000+0.511i	1.000+0.165i
3	-0.237-0.066i	1.000-2.645i	0.300-0.321i	0.208-0.047i
4	-1.000-0.175i	0.450-0.411i	0.970-0.289i	0.759-0.024i
Order	134	144	186	162
Cov-SSI Mode Number	8	9	12	20

Table A.16: Complex representation of each Mode Shape

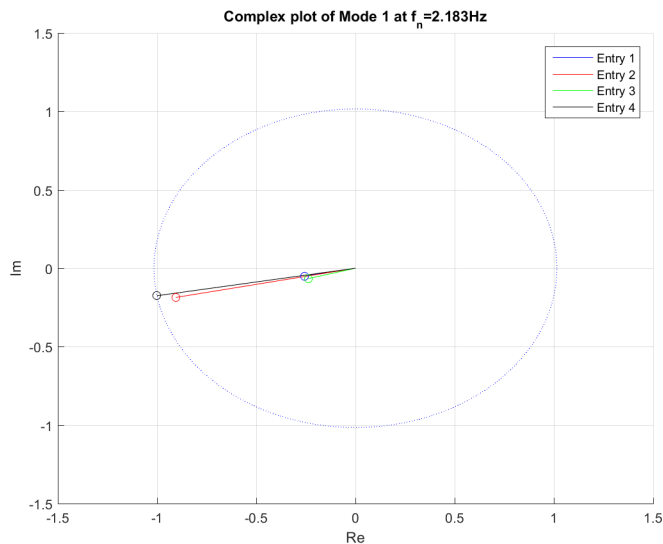


Figure A.24: Argand Diagram of Mode 1

A.3. MOHOLT TWO RESULTS

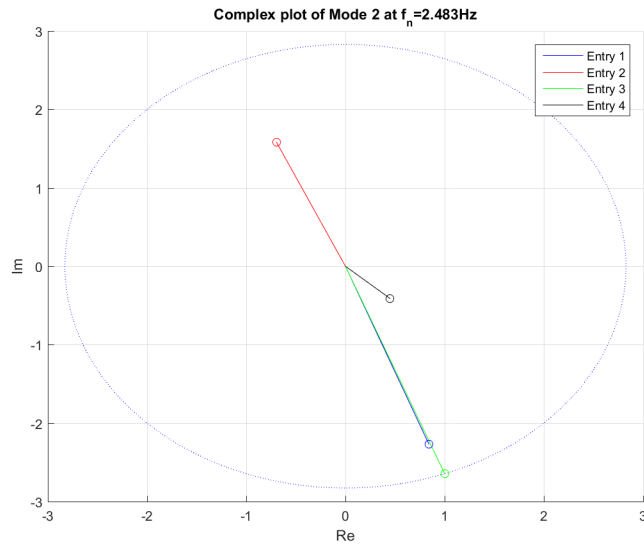


Figure A.25: Argand Diagram of Mode 2

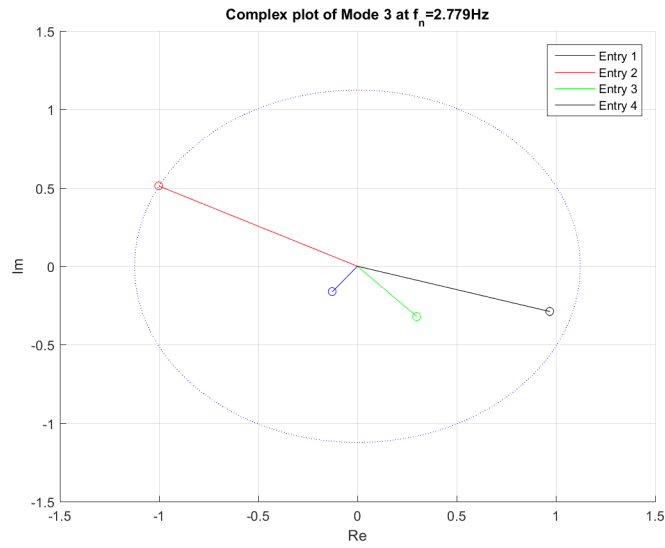


Figure A.26: Argand Diagram of Mode 3

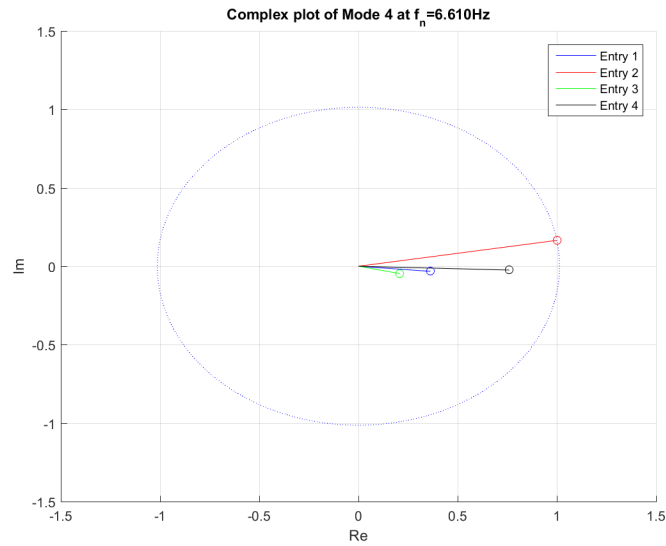


Figure A.27: Argand Diagram of Mode 4

The argand diagrams show generally that the phase shift between the dominating entries in each mode are small. The phase shift of entry 4 in mode 2 and entries 1 and 3 in mode 3 does not fulfill the criteria stated by Rönquist 2005 [39], but the amplitudes are low and it could be expected that the corners actually experiences the rotating motion represented in mode 2 and 3 due to the unsymmetric shape of the building. The trivial representation of vector lengths is considered sufficient for the characterisation of each mode type and dominant direction.

APSD of all channels

Figure A.28 shows the APSDs of all channels using Welch’s Estimate in MatLab weighing 60 segments with MatLab’s built-in hanning window with 50% overlap:

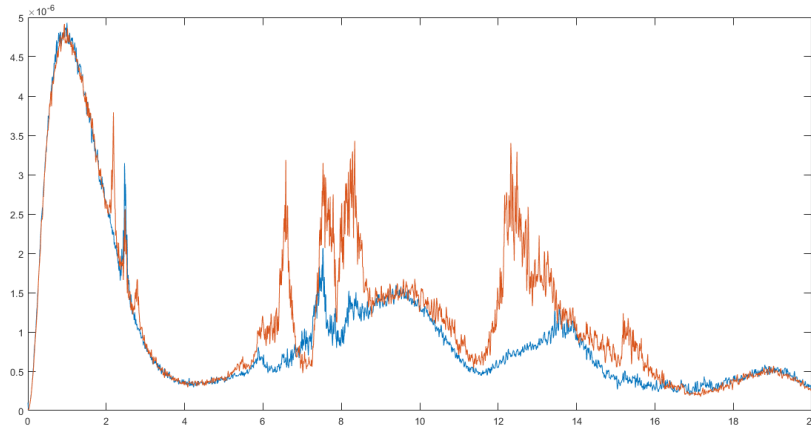


Figure A.28: APSD of each Channel from Moholt Two, Method 2 with Construction Activity

Stabilization Diagram

The following stabilization diagram is based upon data converted into the global coordinate system using equations A.1 and A.2. The measurement data has been downsampled from 1652Hz to 59Hz using MatLab’s resampling function with a built-in anti-aliasing filter [7]. 70 blockrows have been used to establish the corresponding Toeplitz matrix of the system:

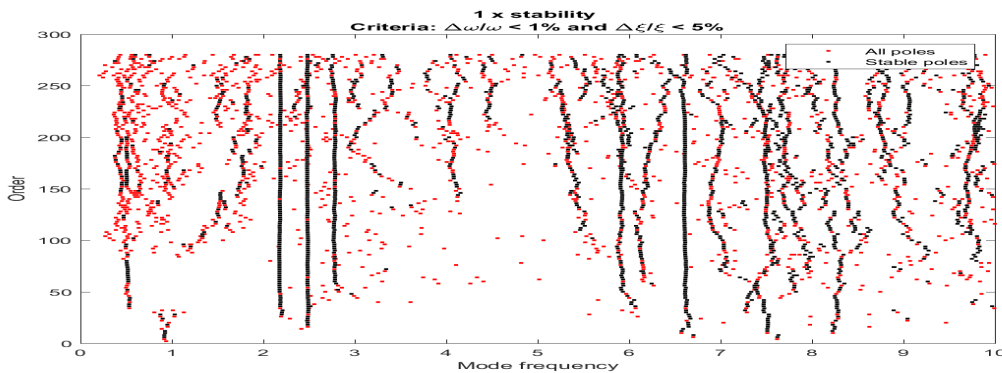


Figure A.29: Stabilization diagram from Moholt Two, Method 2 with Construction Activity

Peak Acceleration and Maximum Dynamic Displacement

The lowpass filter was set to 3.75Hz, and the highpass filter was set to 0.4Hz. People were doing work inside the building while the recording was going on. Channels 3 and 4 have been left out of the consideration, because the filtered time series experienced extreme peak values compared to the standard deviation of their time series

Channel	Max. Acc [mm/s^2]	Max. Displ [mm]
1	5,20	0,0425
2	5,12	0,0500
3	136,86	4,6633
4	696,19	8,4633

Table A.17: Max. Acc. and Max. Dyn. Displ. from Moholt Two, Method 2 with Construction Activity

The corresponding time series used to detect the peak acceleration and dynamic displacement are shown in Figure A.30 and Figure A.31:

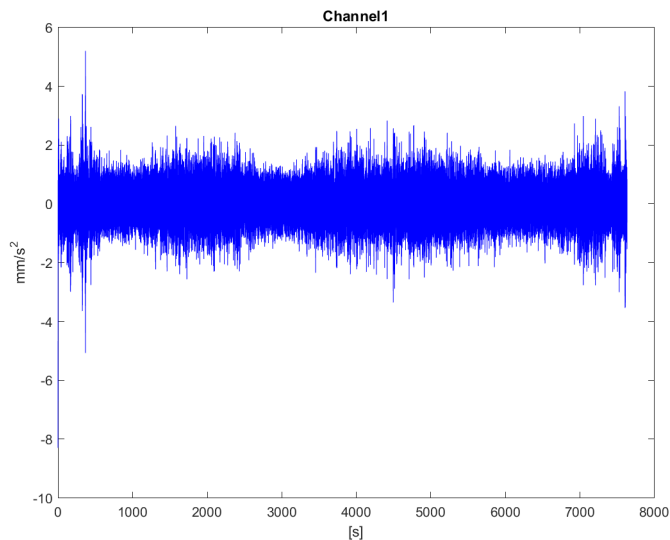


Figure A.30: Acceleration time series in X-direction

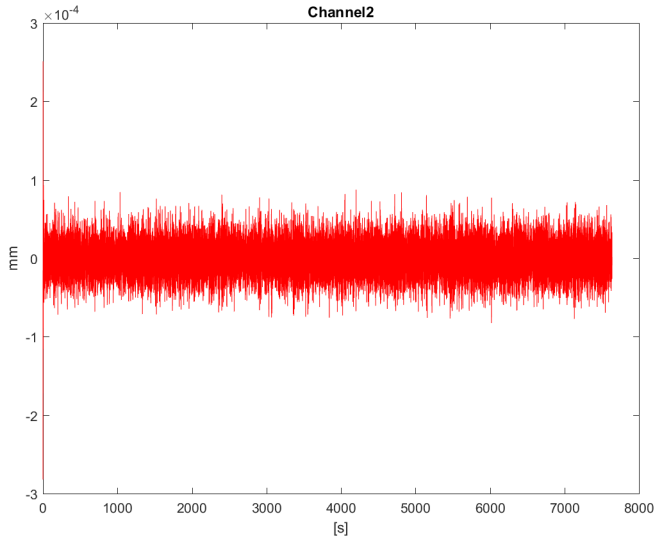


Figure A.31: Dynamic Displacement time series in Z-direction

A.3.3 Excitation Method 2, Without Construction Activity on Site

With no activity on the construction site, little response was detected by the accelerometers. Compared to the situation where there was activity on site, fewer frequency components were detected and the damping estimates were more scattered. The time series used to find the following results was recorded between 7pm and 9pm on May 24th, 2016. As stated in the beginning of this section, the western accelerometer was tilted about 135° the next morning. The time series used for this analysis is performed on the overnight time series after the huge acceleration peak after about one hour into the recording that could have been the cable falling down and rotating the accelerometer.

Table A.18 shows the limitations used to extract natural frequencies and damping from Cov-SSI:

Mode	f_n range [Hz]	ξ range [%]
1	2.16-2.20	1-3.5
2	2.47-2.57	1.5-4.5
4	6.57-6.67	1.5-3.5
5	7.50-7.65	1.5-4.5

Table A.18: Limits on frequency and damping for Moholt Two, Method 2 without Construction Activity

Natural Frequencies

Mode	f_n from APSD	Mean f_n from Cov-SSI	σ_{f_n}	Orders Considered Stable
1	2.189	2.187	9.55e-3	96 to 198
2	2.478	2.523	1.73e-2	44 to 232
4	(6.591)	6.606	7.57e-3	24 to 180
5		7.574	3.07e-2	28 to 266
6	(12.77)	-	-	
7	(16.21)	-	-	

Table A.19: Natural Frequencies from Moholt Two, Method 2 without Construction Activity

Damping Ratios

Mode	ξ	σ_ξ	Orders Considered Stable
1	2.68	3.31e-1	96 to 198
2	2.88	7.96e-1	44 to 232
4	2.41	1.05e-1	24 to 180
5	2.96	2.59e-1	28 to 266

Table A.20: Damping estimates from Moholt Two, Method 2 without Construction Activity

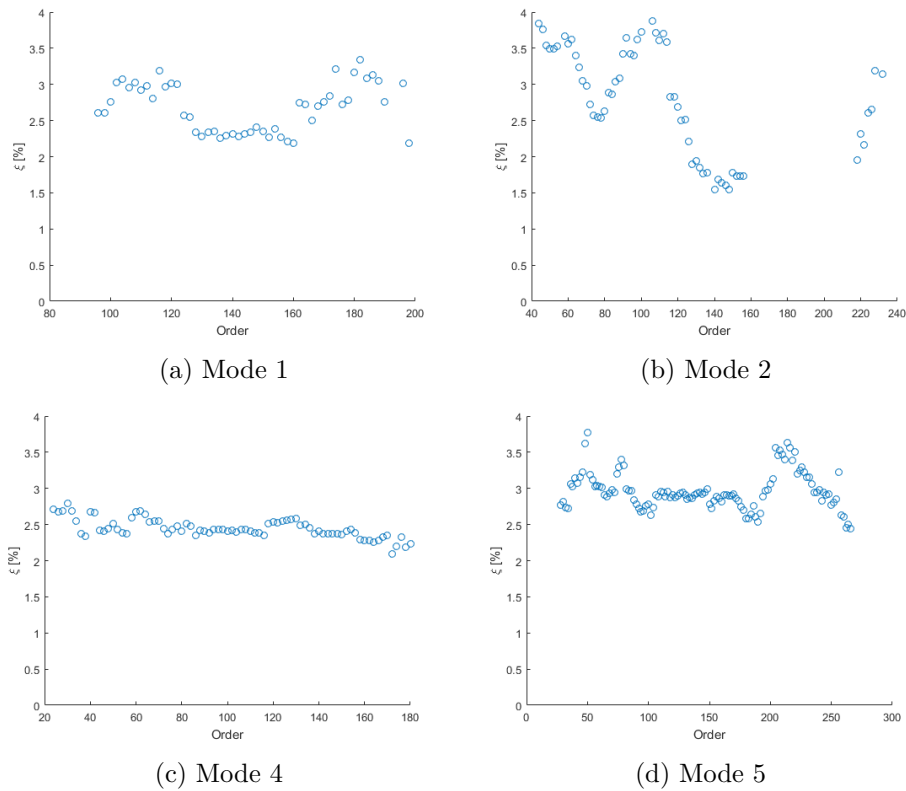


Figure A.32: Scatter of Damping Estimates from Moholt Two, Method 2 without Construction Activity

The damping estimates are widely scattered compared to the estimates for activity on site. The damping level seems to have increased for wind as the only input. The construction site activity could have pumped energy into the modes resulting in a lower damping level or the excitation caused by wind only could simply have been too low to provide good estimates.

Mode Shapes

The resulting system layout, missing only the western X-direction, should have been able to indicate whether it was a bending mode in Z or a torsional mode about the Y -axis. The eastern accelerometer had not been tilted, and should be able to detect whether the dominating direction of a mode is along the global X or Z -direction. Mode shape estimates turned out to be bad, and showed more than $\pm 10^\circ$ phase angle on the same or opposite side of the Argand Diagram, which is not sufficient to be classified as a mode shape [39]. Due to the poor detections of each mode, no relative entry magnitudes and only the Argand Diagrams have been included for a complete report of the situation:

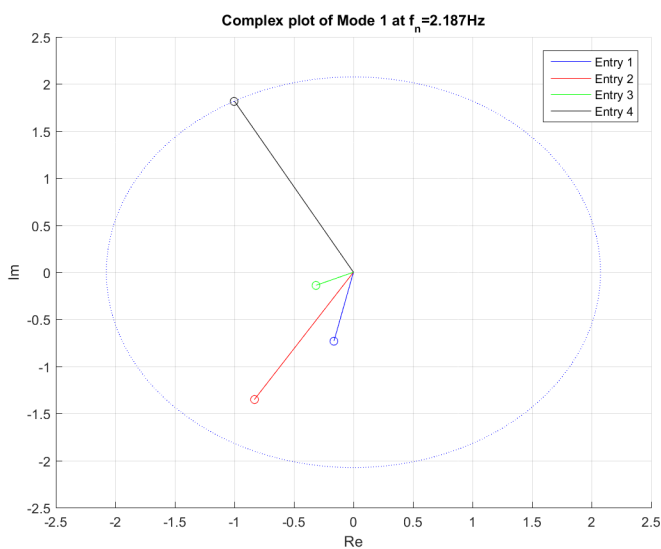


Figure A.33: Argand Diagram of Mode 1

A.3. MOHOLT TWO RESULTS

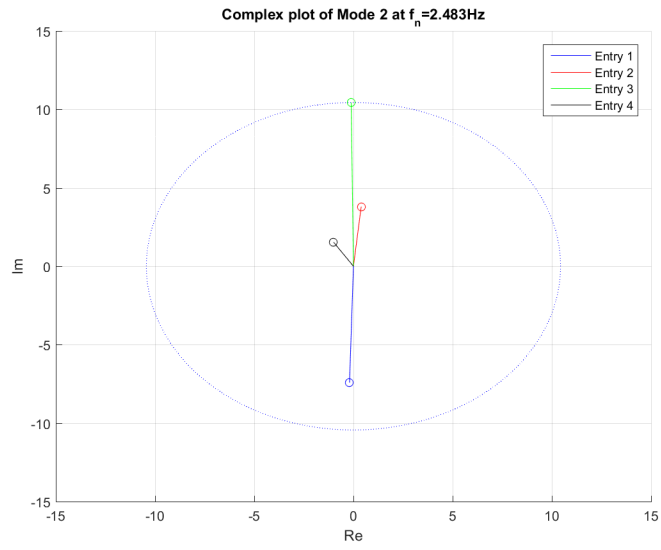


Figure A.34: Argand Diagram of Mode 2

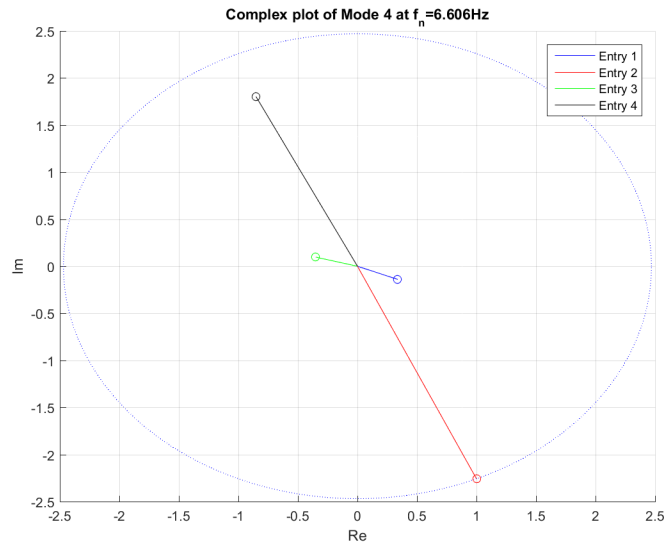


Figure A.35: Argand Diagram of Mode 4

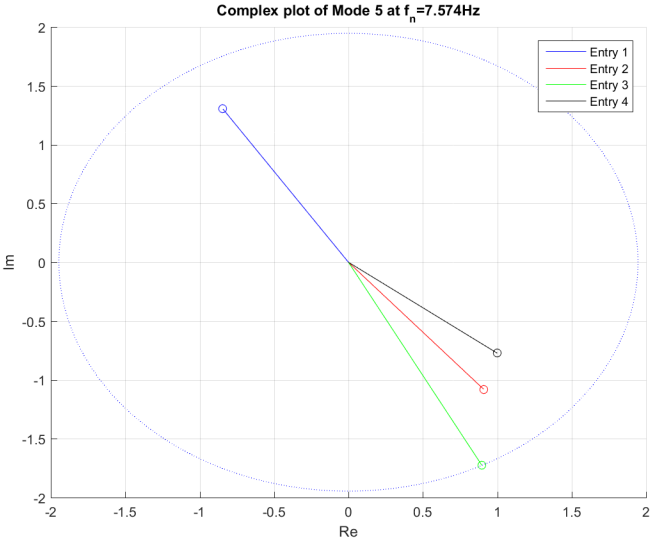


Figure A.36: Argand Diagram of Mode 5

The mode shapes are selected from the stabilization diagram in Figure A.38 at the following orders and Cov-SSI mode numbers:

Mode	Order	Cov-SSI Mode Number
1	86	4
2	132	6
3	142	17
5	138	19

APSD of all channels

Figure A.37 shows the APSDs of channels X and Z at the eastern accelerometer using Welch's Estimate in MatLab [8] weighing 60 segments with MatLab's built-in hanning window [5] and 50% overlap:

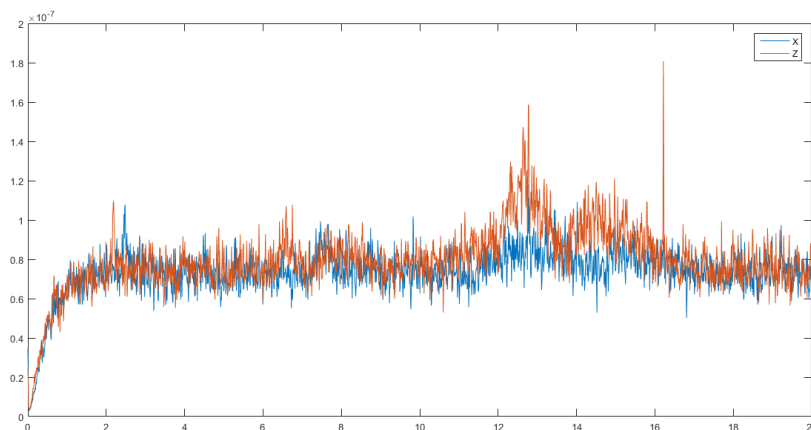


Figure A.37: APSDs of Channels 3 and 4

The auto power spectral densities in X and Z for the eastern accelerometer does not show the broad banded peaks at 0 to 3Hz and 6 to 11.5Hz that was observed with activity on site in figure A.28. This indicates that they were indeed detected input frequencies from construction work around the building within the latter frequency bands, and not the narrow banded peaks that are expected from a structure with constant properties.

Stabilization Diagram

The following stabilization diagram is based upon data converted into the global coordinate system using equations A.1 and A.2. The data has been downsampled from 1652Hz to 59Hz using MatLab's resampling function with a built-in anti-aliasing filter [7]. 70 blockrows have been used to establish the corresponding Toeplitz matrix of the system.

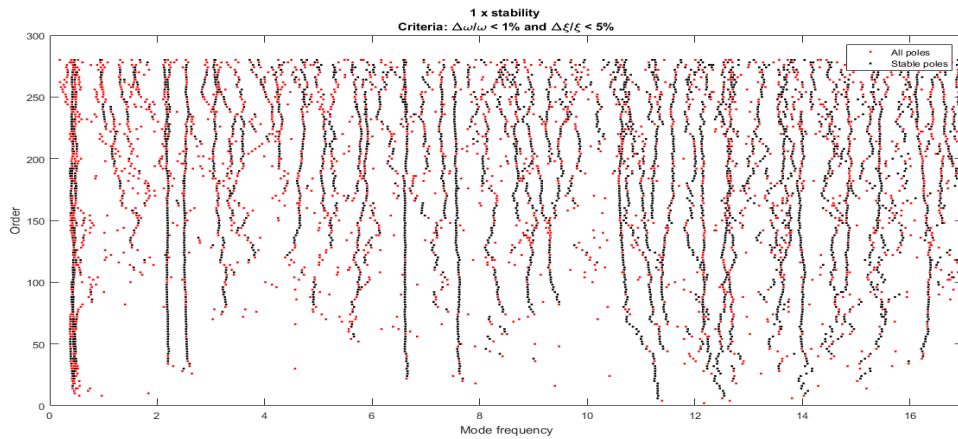


Figure A.38: Stabilization Diagram of Moholt Two, Method 2 without Construction Work

Peak Acceleration and Maximum Dynamic Displacement

The lowpass filter was set to 3.75Hz, and the highpass filter was set to 0.218Hz. Channel 1 has been ignored due to its misalignment with the global coordinate system. The maximum acceleration response amplitudes and corresponding dynamic displacements are shown in table A.21

Channel	Max. Acc. [mm/s^2]	Max. Dyn. Displ. [mm]
1	1,757	0,0728
2	2,360	0,0990
3	2,594	0,0756
4	2,135	0,1188

Table A.21: Max. Acc. and Max. Dyn. Displ. from Moholt Two, Method 2 without Construction Activity

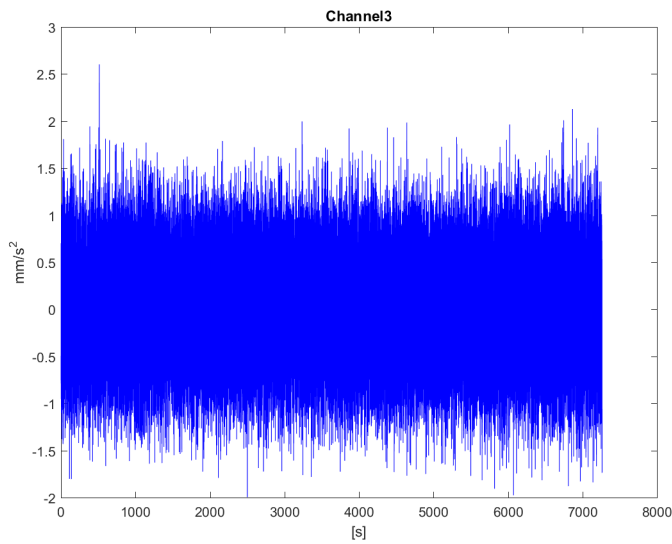


Figure A.39: Acceleration time series in Channel 3

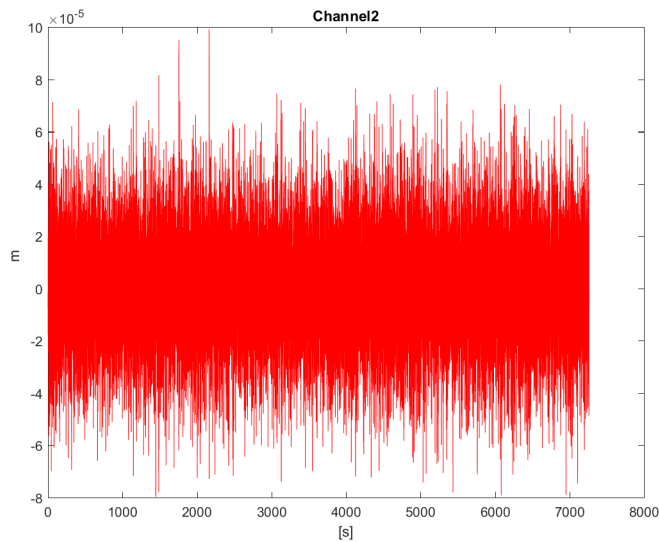


Figure A.40: Dynamic Displacement time series in Channel 2

The maximum detected acceleration is about half the maximum detected acceleration when there was activity on the site, and the maximum dynamic displacement obtained through numerical integration is larger than when there was activity on site. Even after the signal has been filtered, some of the power within the selected frequency band will come from noise.

Appendix B

Treet

Accelerometer measurements in Treet were carried out two times during this thesis. On Day 1, the measurements were acquired using scan mode and experienced uncertain and lowered sampling rates. On Day 2, the data was acquired using scan mode and FPGA at two different accelerometer layouts. The sampling rates on day two were as expected and without data loss.

The measurement files were too big to include into the digital appendix, and were given to supervising professor Kjell Arne Malo on a memory stick [25].

B.1 System Layouts

The accelerometer time series are related to the axes in the figure B.1. The accelerometers were mounted close to the ceiling in the 13th floor and close to the floor in the 9th floor. Not all the accelerometers were aligned with this coordinate system. Each time series must therefore be scaled by 1 or -1 depending on the orientation of the accelerometer during each recording. The details of each system layout is presented in tables B.1, B.2 and B.3. The coordinate system used to present the results is shown in Figure B.1, [4]:

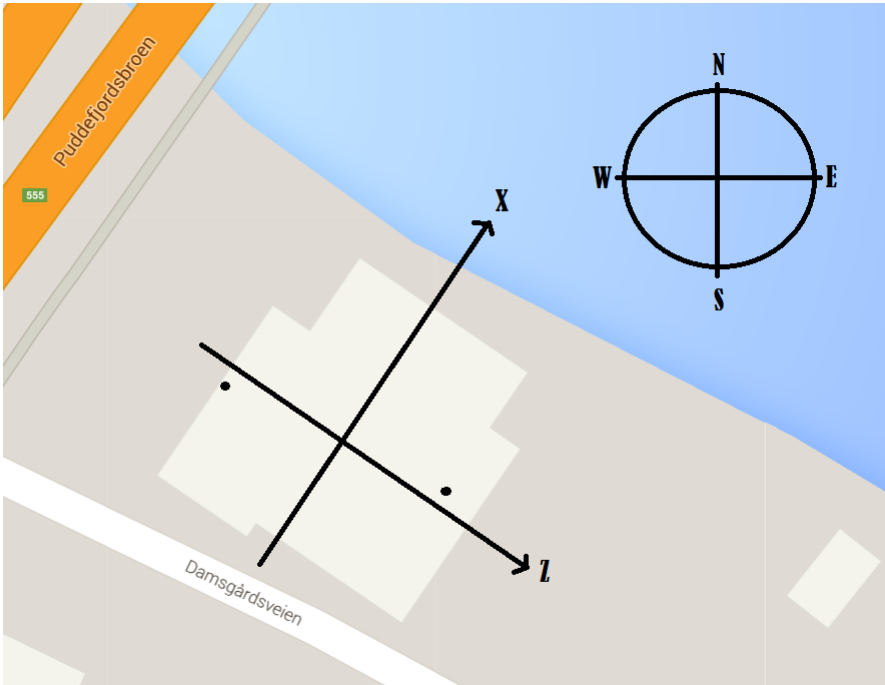


Figure B.1: Coordinate system used to present the results from Treet

When measurements were carried out both in the 9th and 13th floor at the same time, the accelerometers in each floor were connected to the cRIO or expansion chassis only with the cables from their respective producers. Between the expansion chassis and the cRIO, an Ethernet cable was used. When measurements were only carried out in the 13th floor, they were only performed using Kistler accelerometers connected directly to the cRIO with the cables from their producers. See Section D.2 for details.

B.1.1 Day 1

On day 1, accelerometer data is related to the coordinate system in figure B.1 according to table B.1. Voltages were directly converted into m/s^2 inside the VI. The sampling

B.1. SYSTEM LAYOUTS

rate was originally set to 1000Hz. The results presented for Day 1 are base upon the measurement file *Wind1000HzSiste2*.

Floor	Channel	Direction	Scaling Factor	Sensor Position	Accelerometer
13	1	X	1	NW	PCB
13	2	Z	1	NW	PCB
13	3	X	1	SE	Kistler
13	4	Z	-1	SE	Kistler
9	5	X	-1	NW	PCB
9	6	Z	1	NW	PCB
9	7	X	-1	SE	Kistler
9	8	Z	-1	SE	Kistler

Table B.1: Relation between measurement files and local coordinate systems, Day 1

B.1.2 Day 2, FPGA

The following accelerometer layout was used for data aquisition in FPGA mode. Note that the time series are voltages, thus have to be scaled by the individual scaling factors for each accelerometer given by Table D.1. The sampling rate was set to 1652Hz. The results presented for Day 2 using FPGA are based upon the measurement file *FPGA2timerkl0930.tdms*.

Floor	Channel	Direction	Scaling Factor	Sensor Position	Accelerometer
13	1	X	-1	SE	Kistler
13	2	Z	1	SE	Kistler
13	3	X	1	NW	Kistler
13	4	Z	-1	NW	Kistler

Table B.2: Relation between measurement files and local coordinate systems, Day 2, FPGA

B.1.3 Day 2, Scan mode

The time series are voltages, thus have to be scaled by the individual scaling factors for each accelerometer found in Table D.1. Scan mode was set to 1000Hz. Each channel were filtered by a point by point butterworth filter set to 20Hz. Then, every 20th data point of each channel were sent to the .tdms-file found in the digital appendix. The resulting signal has a sampling frequency of 50Hz.

The results presented for Day 2 using scan mode are based upon the measurement file named *scan2timer50Hzkl1247.tdms*.

Floor	Channel	Direction	Scaling Factor	Sensor Position	Accelerometer
13	1	X	-1	SE	Kistler
13	2	Z	1	SE	Kistler
13	3	X	1	NW	PCB
13	4	Z	-1	NW	PCB
9	5	X	-1	SE	Kistler
9	6	Z	1	SE	Kistler
9	7	X	1	NW	PCB
9	8	Z	-1	NW	PCB

Table B.3: Relation between measurement files and local coordinate systems, Day 2, scan mode

B.2 Results

Estimates for the detected natural frequencies have been performed using two different methods. The first method looks at the position of peaks in the auto power spectral densities. If a peak is not well distinguished from surrounding noise, it is placed within a paranthesis indicating its uncertainty. The second method uses results from Cov-SSI. As the estimates vary for different system orders, a statistical representation with a mean value and a standard deviation σ has been chosen. A statistical representation has also been chosen for the damping estimates from Cov-SSI. Mode shapes are indicated by arrows on the structural system, indicating the relative acceleration magnitudes detected between each accelerometer in each mode. The directions are related to the coordinate system in figure B.1.

The mode shapes come in three classes indicated in the figures below. When each mode shape is represented, its order and eigenmode number from Cov-SSI is stated along its physical mode number.

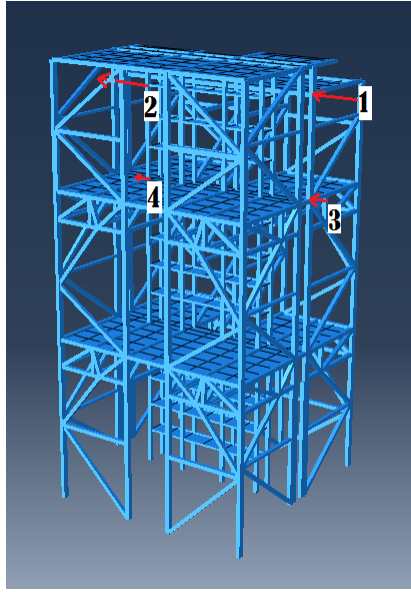


Figure B.2: Bending Mode in Z-direction

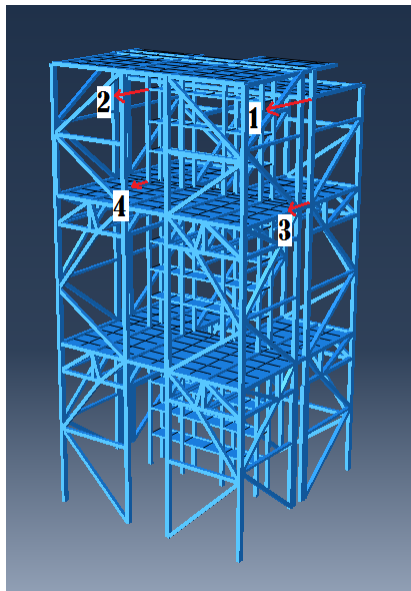


Figure B.3: Bending Mode in X-direction

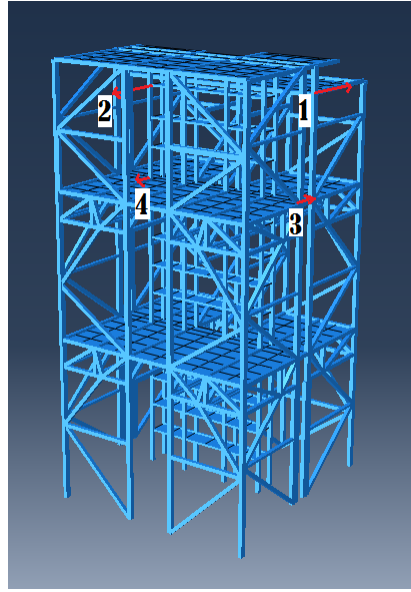


Figure B.4: Torsional Mode

B.2.1 Day 1

The acceleration time series were acquired using scan mode. The accelerometers were mounted close to the ceiling in the 13th floor and close to the floor in the 9th floor. The sensors used on the south-eastern part of the building were the Kistlers. On the north-western part, the PCB sensors were used. The results presented in this thesis are based upon the file named "Wind1000HzSiste2.tdms" which can be found on the memory stick delivered to Kjell Arne Malo [25].

Table B.4 shows the limitations used to extract natural frequencies and damping from Cov-SSI:

Mode	f_n range [Hz]	ξ range [%]
1	0.978-0.983	1-3
2	1.136-1.144	1-3
3	1.800-1.815	1-3

Table B.4: Limits on frequency and damping for Bergen Day 1

Natural frequencies, Scan Mode

After timing the number of points per second using a stopwatch, the sampling ratio was found to be somewhere between 760 and 780Hz. For longer observations, the sampling

rate usually landed close to 770Hz, and this is the assumed sampling rate for Day 1 in Bergen.

Mode	f_n from APS D	Mean f_n from Cov-SSI	σ_{f_n}	Orders Considered Stable
1	0.974	0.979	4.11e-4	4 to 362
2	1.15	1.140	9.14e-4	26 to 390
3	Unclear	1.807	1.93e-3	14 to 434

Table B.5: Natural Frequencies from Bergen Day 1

Damping ratios

Mode	ξ	σ_ξ	Orders Considered Stable
1	1.89	2.70e-2	4 to 362
2	1.45	6.79e-2	26 to 390
3	1.74	1.97e-1	14 to 434

Table B.6: Damping Ratios from Bergen Day 1

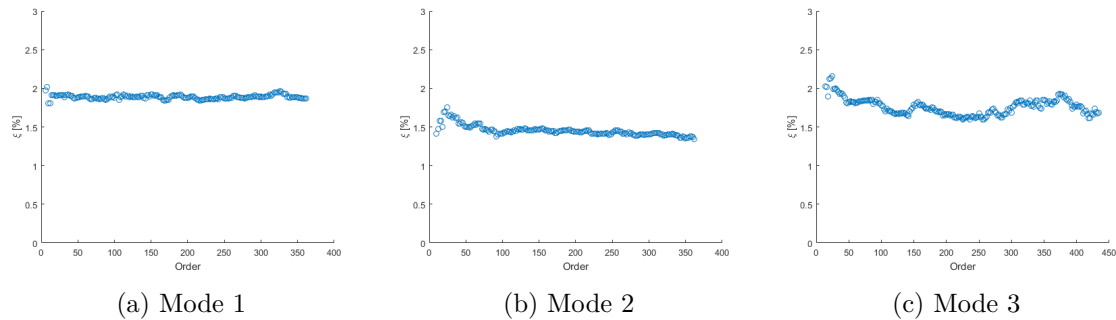


Figure B.5: Scatter of Damping Estimates

Mode Shapes

On Day 1, three modes were relatively well detected. The relative magnitudes of each eigenvector indicated in Figures B.2, B.3 and B.4 are shown in the tables below. The eigenvectors are detected using Cov-SSI and are the eigenvectors obtained using equation (3.77) at the corresponding system orders and Cov-SSI eigenvalue numbers are also indicated in tables B.8 and B.7. Only the entries in the dominant direction of a mode have been included.

B TREE

Entry	Mode 1, Z	Mode 2, X	Mode 3, Torsion
1	1.000	0.909	1.000
2	0.982	1.000	-0.679
3	0.650	0.634	0.708
4	0.672	0.680	-0.324
Order	238	152	234
Cov-SSI mode-number	16	16	23

Table B.7: Relative lengths of each eigenvector

Entry	Mode 1, Z	Mode 2, X	Mode 3, Torsion
1	1.000+0.232i	0.831-0.795i	1.000+0.058i
2	0.958+0.314i	1.000-0.775i	-0.677-0.061i
3	0.655+0.124i	0.558-0.575i	0.709+0.001i
4	0.665+0.182i	0.650-0.565i	-0.324-0.013i
Order	238	152	234
Cov-SSI mode-number	16	16	23

Table B.8: Complex entries of each eigenvector

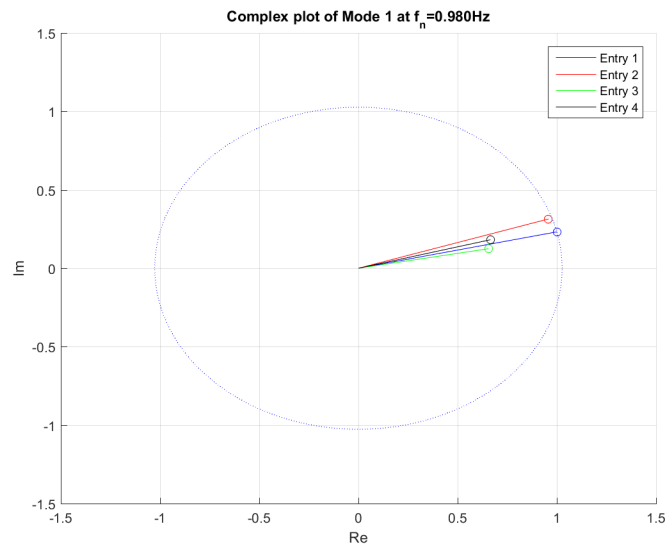


Figure B.6: Argand Diagram of Mode 1

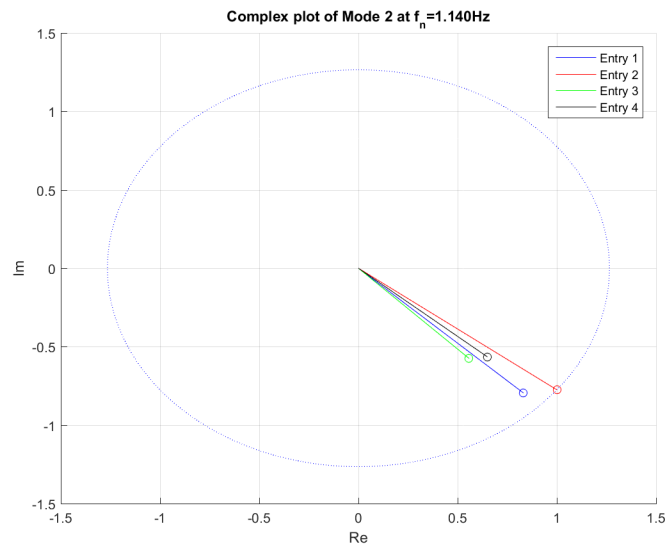


Figure B.7: Argand Diagram of Mode 2

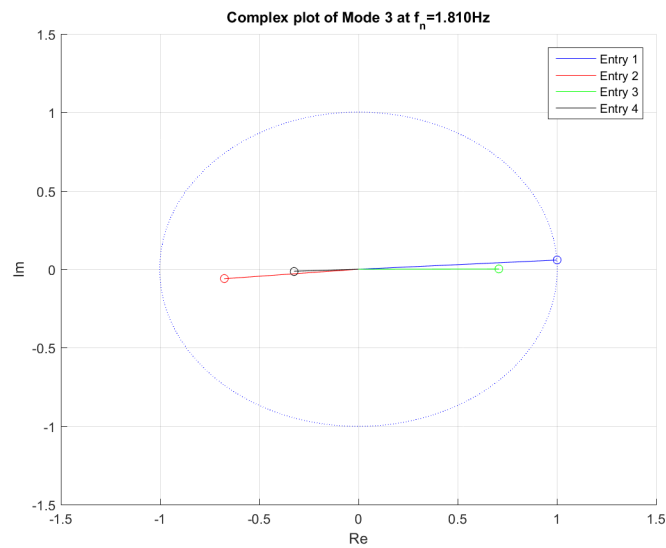


Figure B.8: Argand Diagram of Mode 2

The Argand Diagrams show small phase angles between each DOF. They will pass the real plane at almost the same time, and fulfil the criterion discussed in subsection 3.4.1. The representation in table B.7 is therefore both a suitable and trivial representation of the detected mode shapes.

APSD of all channels, Scan mode

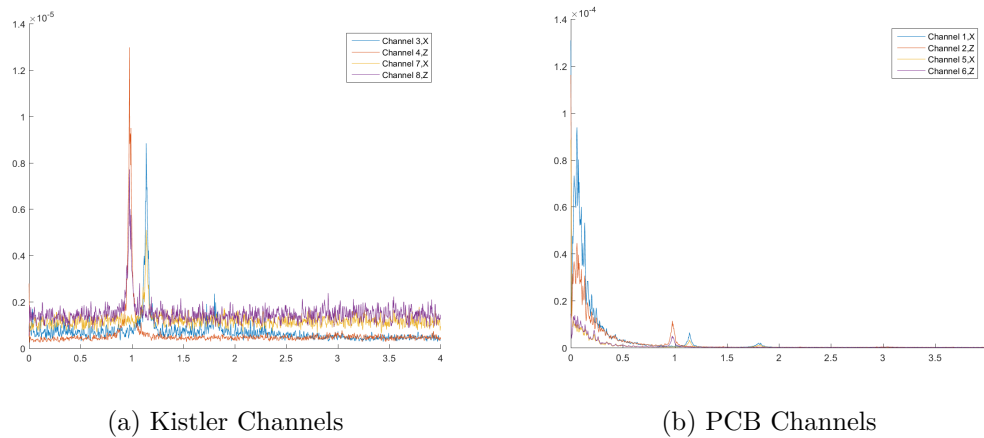


Figure B.9: APSD of all Channels

The PCB accelerometers show a lot of low frequency noise compared to the Kistlers. Before processing the time series, the mean value of the entire time series were subtracted from each channel. When zooming into the time PCB time series, low frequency components can be seen throughout the entire time series. Figure B.10 shows a segment of the time series from channel 1 lowpassed at 2.5Hz.

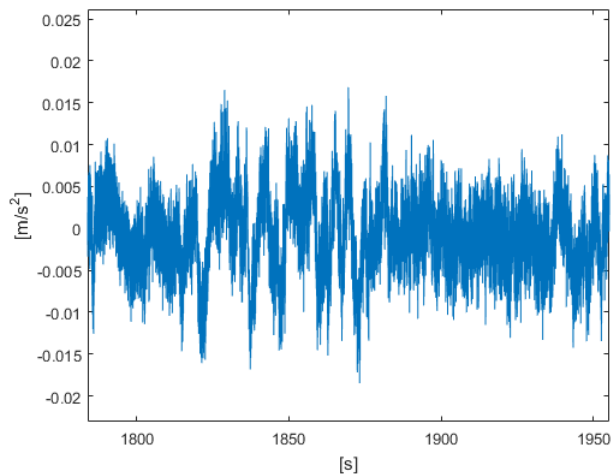


Figure B.10: PCB time series in Channel 1

Stabilization Diagram

The following stabilization diagram has been created after resampling each channel from the assumed 770Hz down to 33Hz. 68 blockrows have been used to establish the Toeplitz matrix of the system.

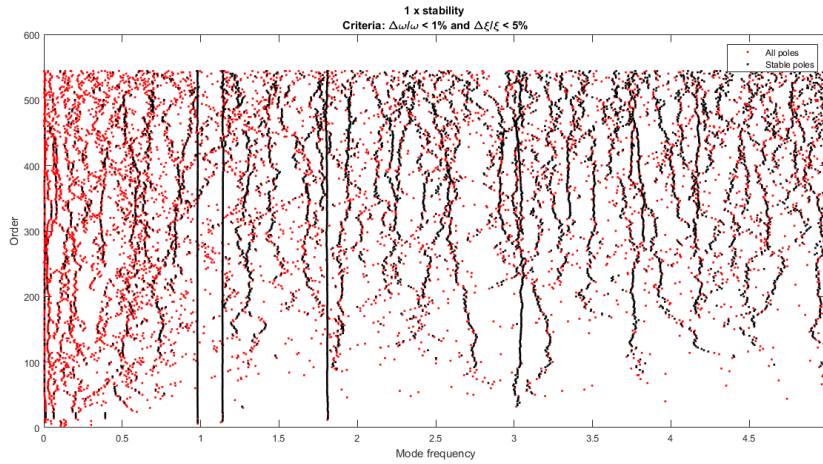


Figure B.11: Stabilization diagram of Day 1

Peak Acceleration and Maximum Dynamic Displacement

In order to remove the spurious low frequency components from the PCBs, a highpass filter was set to 0.5Hz. Then, the lowpass filter was set to 2.5Hz and the highpass filter was set to 0.097Hz between each integration. The maximum accelerations and displacements are shown in Table B.9:

Channel	Max. Acc. [m/s^2]	Max. Dyn. Displ. [mm]
1	10,178	0,9940
2	16,524	1,2118
3	7,142	0,7034
4	5,896	0,6160
5	20,994	1,5807
6	14,103	1,2737
7	6,836	0,8385
8	8,810	0,7458

Table B.9: Max. Acc. and Max. Dyn. Displ. in all channels from Bergen Day 1

Even after applying the filters, Figures B.12 and B.13 show that the PCB accelerometers experience local peaks while the Kistlers do not. The behaviour is therefore not

considered representative for a global acceleration response caused by wind input. The Kistlers in the 9th floor show higher acceleration than the Kistlers in the 13th floor, and Figure B.12 shows all over a higher acceleration level in the 9th floor. Considering the fact that the time series contain a lot of noise due to the uneven sampling rates discussed below, non of the displacement or acceleration magnitudes are considered an accurate representation of the global response in the building.

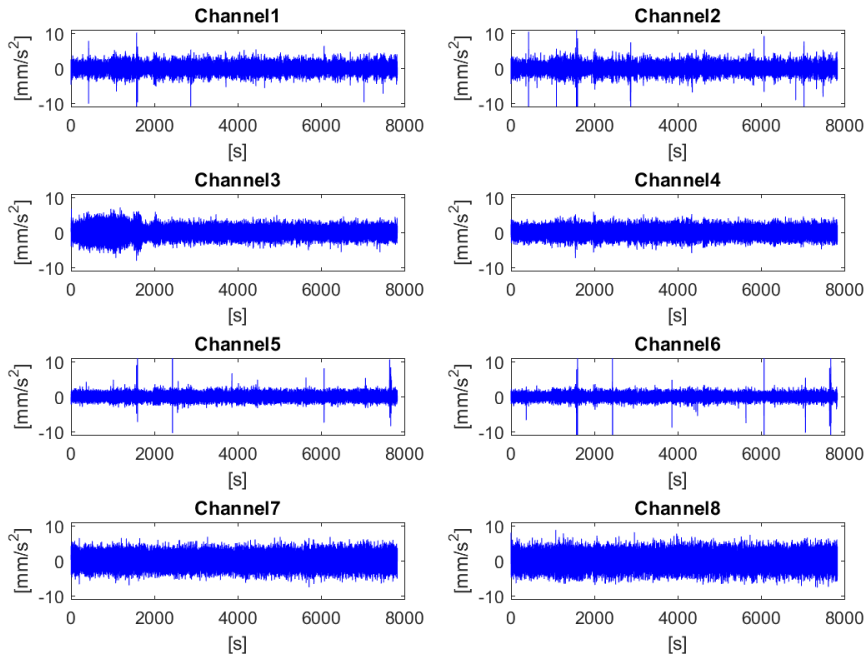


Figure B.12: Acceleration time series of each channel during Day 1

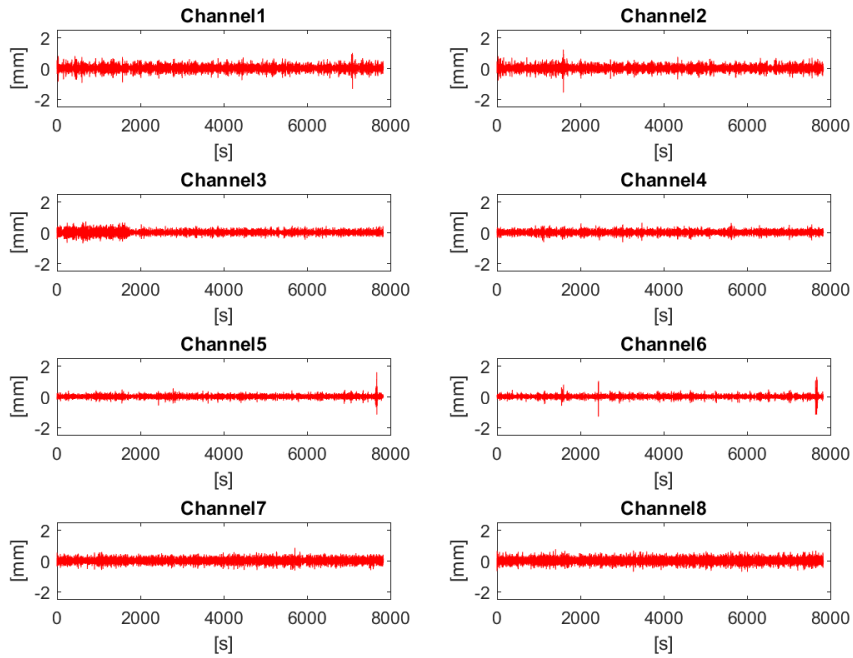


Figure B.13: Dynamic displacement time series of each channel during Day 1

B.2.2 Day 2, Scan Mode Results

In scan mode, timestamps recorded how long each timed loop needed to feed data into the FIFO. The timestamps show that no points were lost, and that the sampling rate was not experiencing any significant jitter (see Figure C.3). Scan mode was set to 1000Hz, and each channel was filtered down to 20Hz using a 10th order pt. by pt. butterworth filter defined in LabVIEW. Then, every 20th data point was sent into the FIFO, resulting in a sampling rate of 50Hz.

Table B.10 shows the limitations used to extract natural frequencies and damping from Cov-SSI:

Mode	f_n range [Hz]	ξ range [%]
1	0.965-0.980	1-3
2	1.125-1.132	1-3
3	1.780-1.800	1-3
4	2.980-3.020	1-3
5	3.680-3.720	0.5-2

Table B.10: Limits on frequency and damping for Bergen Day 2 using scan mode

Natural frequencies, Scan Mode

Mode	f_n from APSD	Mean f_n	σ_{f_n}	Orders considered stable
1	0.969	0.973	4.30e-4	8 to 236
2	1.13	1.13	5.03e-4	14 to 288
3	1.78	1.79	2.17e-3	14 to 232
4	(2.99)	3.00	3.18e-3	22 to 264
5	(3.70)	3.69	4.69e-3	26 to 268

Table B.11: Detected Natural Frequencies using Scan Mode

Damping ratios, Scan Mode

Mode	Mean ξ	σ_{ξ}	Orders considered stable
1	1.99	2.79e-2	8 to 236
2	1.75	3.93e-2	14 to 288
3	2.09	1.02e-1	14 to 232
4	2.30	9.01e-2	22 to 264
5	1.23	1.73e-1	26 to 268

Table B.12: Detected Natural Frequencies using Scan Mode

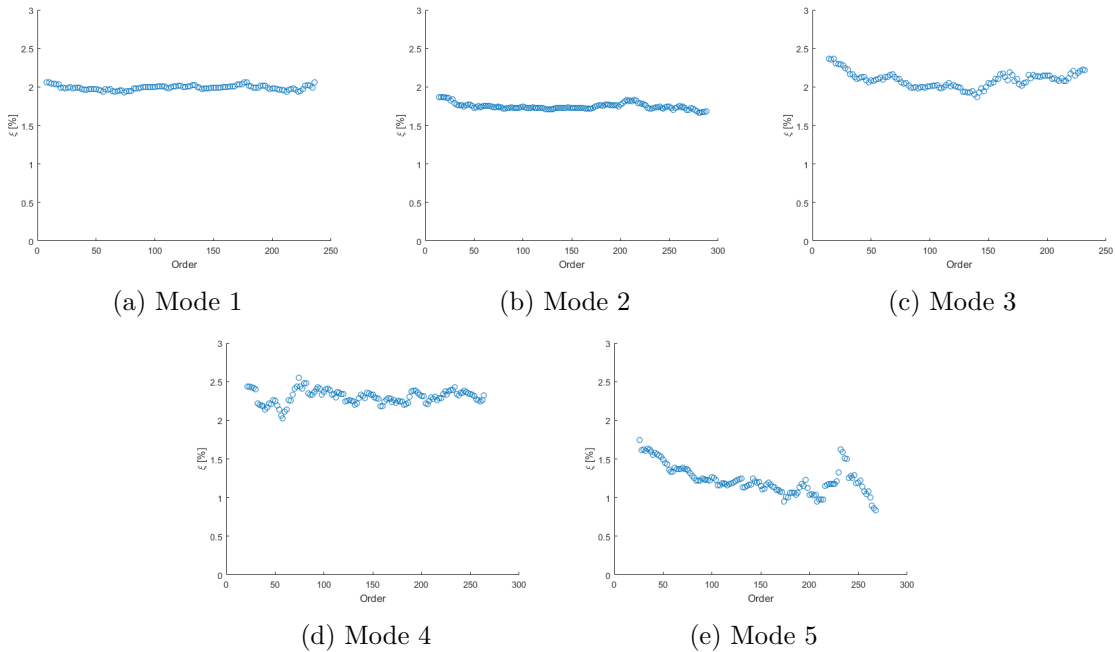


Figure B.14: Scatter of Damping Estimates

Mode Shapes, Scan Mode

On day 2, five modes were relatively well detected using scan mode. The relative magnitudes of each eigenvector entry indicated in Figures B.2, B.3 and B.4 are shown in the tables below. Modes 4 and 5 refer to Figures B.2 and B.3 respectively.

Entry	Mode 1, Bending Z	Mode 2, Bending X	Mode 3, Torsion	Mode 4, Bending Z	Mode 5, Bending X
1	1.000	-1.000	-0.626	0.916	-1.000
2	0.971	-0.888	1.000	1.000	-0.936
3	0.695	-0.701	-0.431	-0.811	0.754
4	0.687	-0.651	0.761	-0.806	0.713
Order	160	112	134	90	104
Cov-SSI mode-number	13	13	17	18	24

Table B.13: Lengths of each eigenvector entry

Entry	Mode 1, Bending Z	Mode 2, Bending X	Mode 3, Torsion	Mode 4, Bending Z	Mode 5, Bending X
1	1.000-4.950i	-1.000-0.135i	0.771-2.609i	-0.918+1.319i	1.000-0.987i
2	0.430-4.887i	-0.894-0.061i	-1.000+4.231i	-1.000+1.440i	0.803-1.042i
3	0.771-3.423i	-0.702-0.089i	0.548-1.793i	0.737-1.215i	-0.472+0.948i
4	0.312-3.456i	-0.656-0.031i	-0.767+3.217i	0.756-1.195i	-0.579+0.818i
Order	160	112	134	90	104
Cov-SSI mode-number	13	13	17	18	24

Table B.14: Complex eigenvector entries

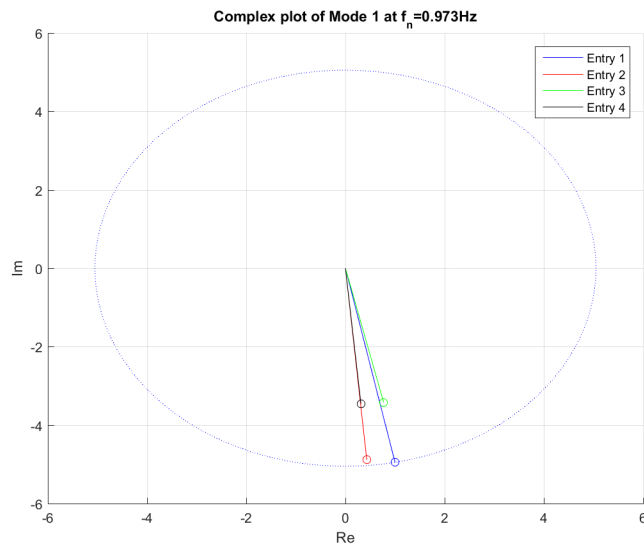


Figure B.15: Argand Diagram of Mode 1

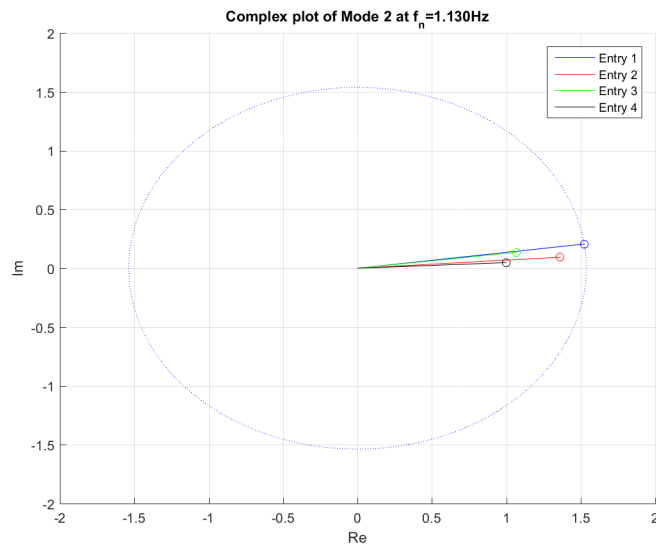


Figure B.16: Argand Diagram of Mode 2

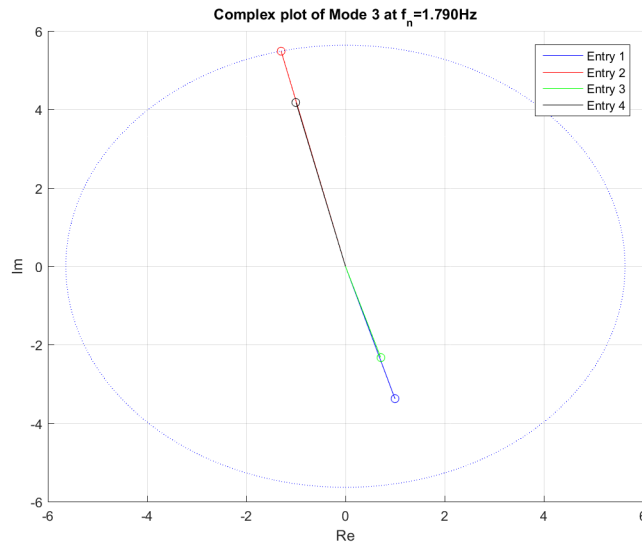


Figure B.17: Argand Diagram of Mode 3

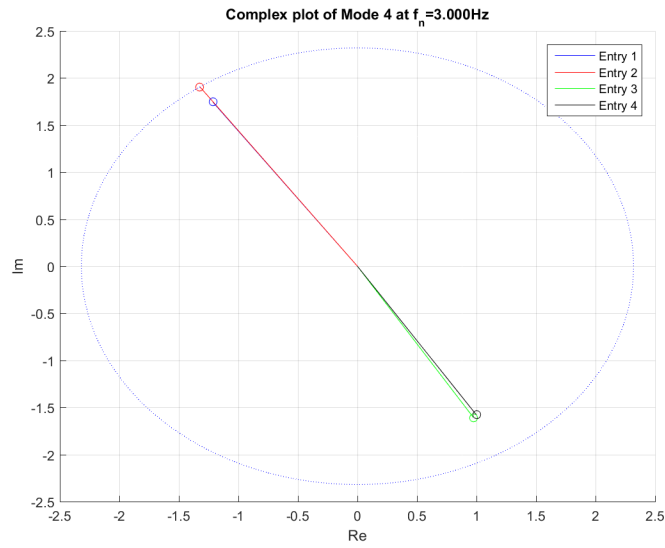


Figure B.18: Argand Diagram of Mode 4

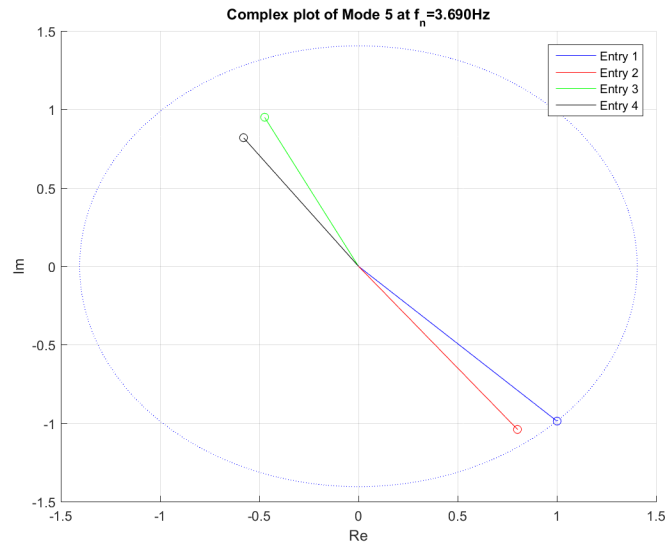
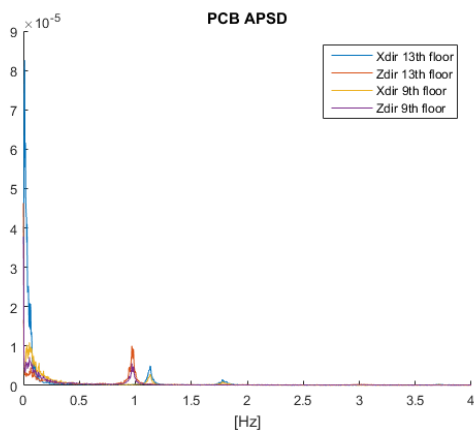


Figure B.19: Argand Diagram of Mode 5

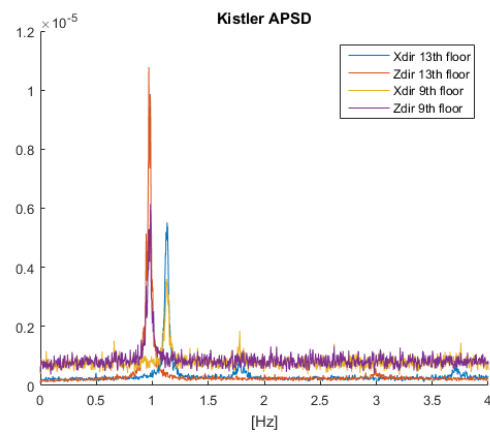
Modes 1 and 5 exhibit the largest phase shifts, but compared to the variation of mode estimates over different system orders, the absolute value representation in table B.13 seems to be a suitable representation of the mode shapes.

APSD of all Channels

The APSDs are calculated using welch’s estimate in MatLab for 20 segments and 50% overlap weighted by MatLab’s hanning window:



(a) APSD of the PCB Time Series



(b) APSD of the Kistler Time Series

Stabilization Diagram, Scan Mode

The following stabilization diagram has been created after resampling each channel from 50Hz down to 25Hz. 40 blockrows have been used to establish the Toeplitz matrix of the system.

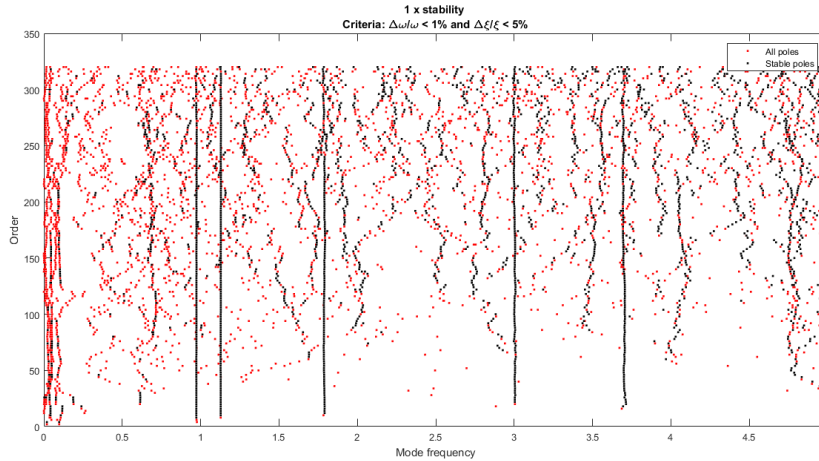


Figure B.21: Stabilization diagram of data obtained using Scan Mode

Maximum Acceleration and Displacement, Scan Mode

In order to remove the spurious low frequency components from the PCBs, a highpass filter was set to 0.5Hz. Then, the lowpass filter was set to 4.75Hz, and the highpass filter after each integration was set to 0.097Hz. The peak accelerations and dynamic displacements are reported in Table B.15. The peak acceleration time series and obtained dynamic displacement series are shown in Figures B.22 and B.23.

Again, the peak accelerations detected by the Kistlers are larger in the 9th floor than

Channel	Max. Acc. [mm/s^2]	Max. Dyn. Disl. [mm]
1	7,712	0,1212
2	10,331	0,2398
3	24,960	0,3323
4	39,253	0,8411
5	12,971	0,1935
6	11,970	0,2155
7	8,027	0,2005
8	25,899	0,1691

Table B.15: Max. Acc. and Max. Dyn. Displ. from Bergen Day 2, scan mode

the 13th floor. The PCBs exhibit what are considered spurious peaks, and their peak values are not considered representative. It can be seen from Figure B.22 that the accelerometers in the 9th floor experiences an increase in response towards the end of the time series, while the accelerometers in the 13th floor do not. Therefore, only the Kistlers in the upper floor have been considered representative.

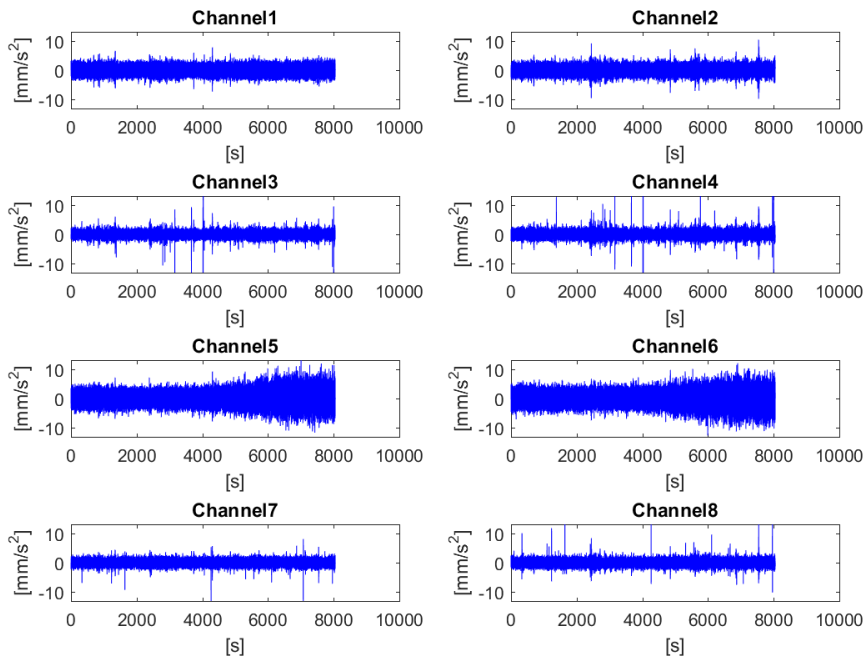


Figure B.22: Acceleration time series of each channel. Day 2, scan mode.

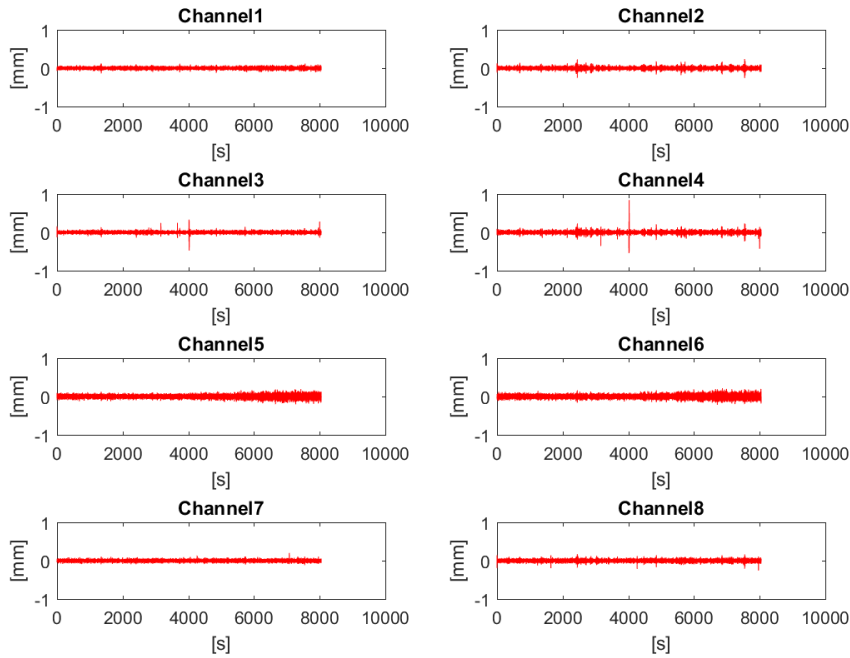


Figure B.23: Dynamic Displacement time series of each channel. Day 2, scan mode.

B.2.3 Day 2, FPGA Results

Timestamps were not directly implemented into the FPGA VI, but every 280th point from each channel received a timestamp in the Real-Time VI. Figure C.5 shows that very few data points are uncertain with respect to sampling rate and data loss. The sampling rate was set to 1652Hz.

Table B.16 shows the limitations used to extract natural frequencies and damping from Cov-SSI:

Mode	f_n range [Hz]	ξ range [%]
1	0.960-0.980	1-3
2	1.120-1.130	1-3
3	1.770-1.800	1-3
4	3.000-3.030	1-3
5	3.700-3.760	1.5-3.5

Table B.16: Limits on frequency and damping for Bergen Day 2, FPGA

Natural frequencies, FPGA

Mode	f_n from APSD	Mean f_n	σ_{f_n}	Orders considered stable
1	0.975	0.972	7.57e-5	30 to 306
2	1.13	1.12	2.92e-4	38 to 328
3	1.80	1.79	4.49e-4	58 to 266
4	(3.01)	3.01	1.78e-3	40 to 328
5	Unclear	3.72	4.94e-3	58 to 218

Table B.17: Natural Frequencies from Bergen Day 2, FPGA

Damping ratios, FPGA

Mode	Mean ξ	σ_{ξ}	Orders considered stable
1	1.84	7.85e-3	30 to 306
2	1.61	1.68e-2	38 to 328
3	1.98	4.93e-2	58 to 266
4	2.28	5.74e-2	40 to 328
5	2.45	9.26e-2	58 to 218

Table B.18: Damping Ratios from Bergen Day 2, FPGA

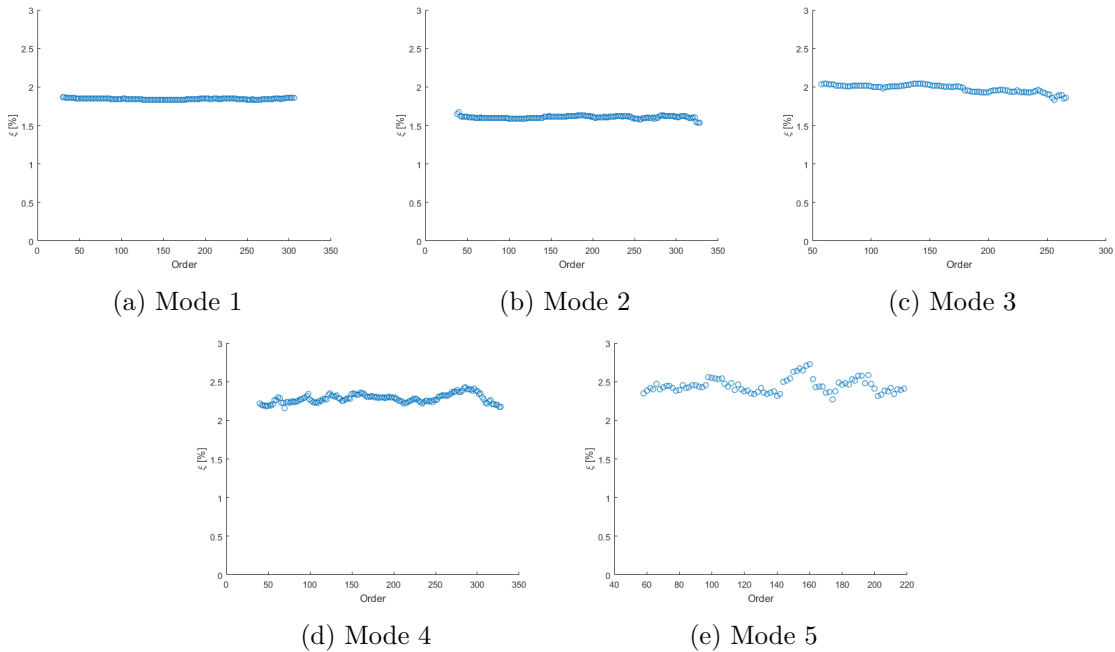


Figure B.24: Scatter of Damping Estimates

Mode Shapes, FPGA

On day 2, five modes were detected using Cov-SSI. The relative magnitudes of each eigenvector entry indicated in Figures B.2, B.3 and B.4 are shown in the tables below. Modes 4 and 5 relate to Figures B.2 and B.3, respectively.

Entry	Mode 1 Z	Mode 2 X	Mode 3 Torsion	Mode 4 Z	Mode 5 X
1	0.995	1.000	-0.615	0.950	1.000
2	1.000	0.944	1.000	1.000	0.901
Order	142	140	122	136	120
Cov-SSI mode-number	4	6	7	9	10

Table B.19: Relative lengths of each eigenvector

Entry	Mode 1 Z	Mode 2 X	Mode 3 Torsion	Mode 4 Z	Mode 5 X
1	0.995+0.042i	1.000+0.001i	-0.613-0.057i	-0.934-0.251i	-1.000-0.314i
2	1.000+0.038i	0.944-0.014i	1.000+0.038i	-1.000-0.195i	-0.920-0.214i
Order	142	140	122	136	120
Cov-SSI mode-number	4	6	7	9	10

Table B.20: Complex entries of each eigenvector

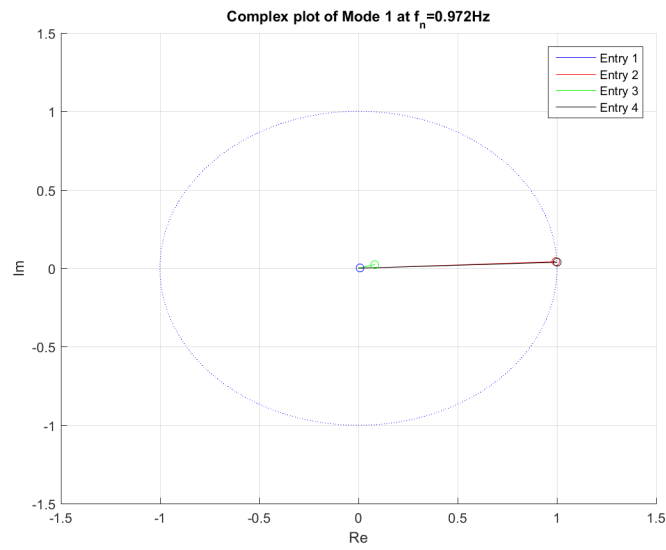


Figure B.25: Argand Diagram of Mode 1

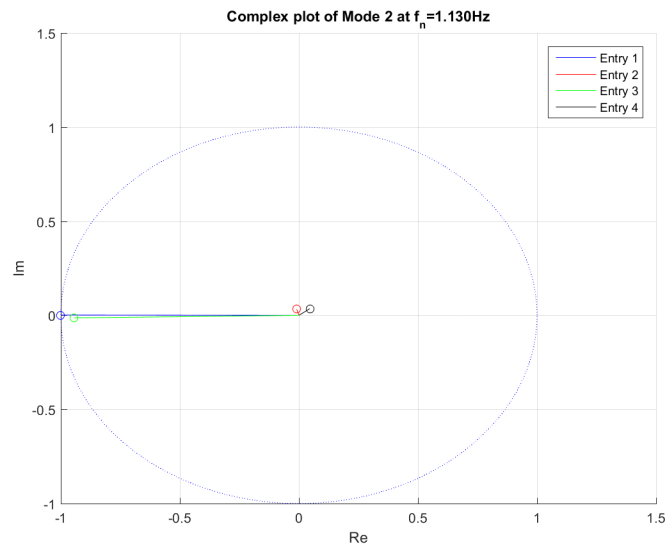


Figure B.26: Argand Diagram of Mode 2

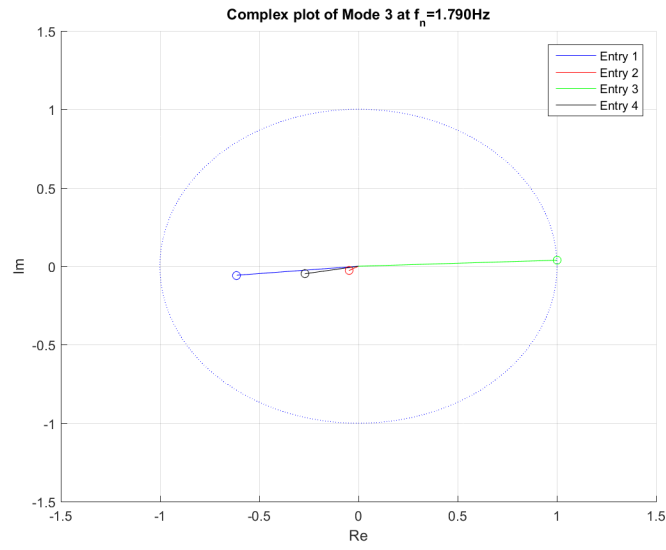


Figure B.27: Argand Diagram of Mode 3

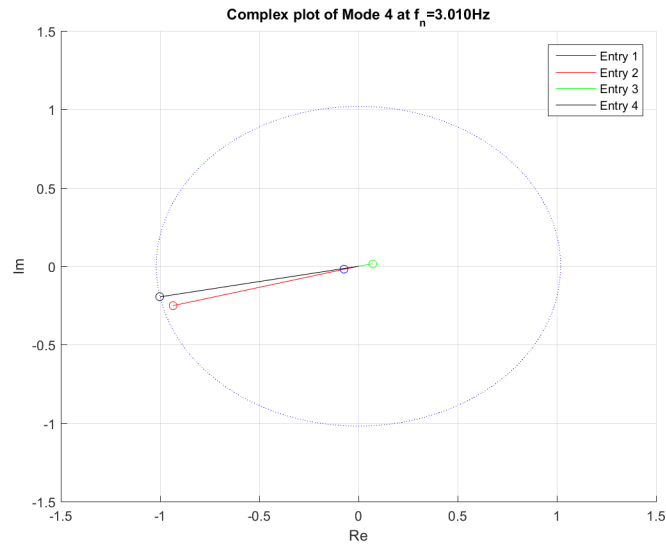


Figure B.28: Argand Diagram of Mode 4

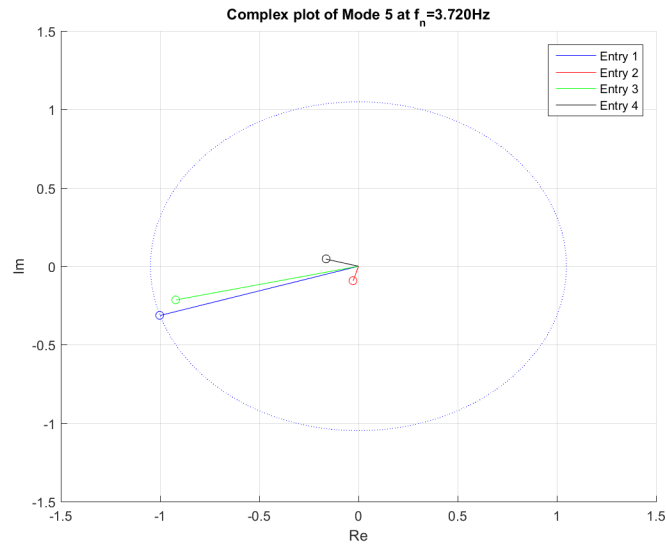


Figure B.29: Argand Diagram of Mode 5

The Argand diagrams show that the contributions from the non-dominant directions are small. Mode 3 experiences a small contribution in Z-direction, and its presence is assumed to be a consequence of the fact the position of the rotation center is not known, and is not necessarily in the middle of the two accelerometers. The building is more symmetric than Moholt 50|50, but it is not perfectly symmetric, and this could also result in contributions from the non-dominant directions in a mode shape.

APSD of all channels, FPGA

In order to calculate the APSDs, the measurement file was downsampled from 1652Hz to 59Hz. Then, Welch's Estimate was calculated weighting 40 segments with hanning windows [5] and 50% overlap.

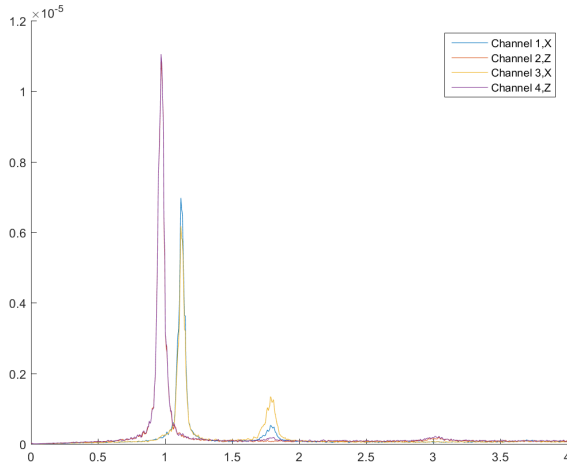


Figure B.30: APSD of all channels

Stabilization Diagram, FPGA

The following stabilization diagram has been created after downsampling each channel from 1652Hz down to 59Hz. 90 blockrows have been used to establish the Toeplitz matrix of the system.

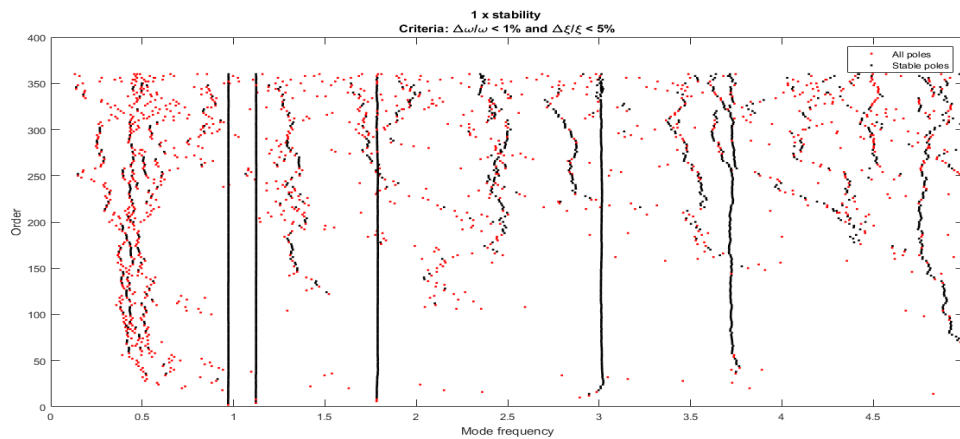


Figure B.31: Stabilization diagram of data obtained using FPGA

Maximum Acceleration and Displacement, FPGA

The lowpass filter was set to 3.5Hz and the highpass filter was set to 0.097Hz after each integration.

Channel	Max. Acc. [mm/s^2]	Max. Dyn. Displ. [mm]
1	6,973	0,2131
2	7,748	0,3221
3	7,365	0,2500
4	8,228	0,3349

Table B.21: Max. Acc. and Max. Dyn. Displ. of each channel Bergen Day 2, FPGA

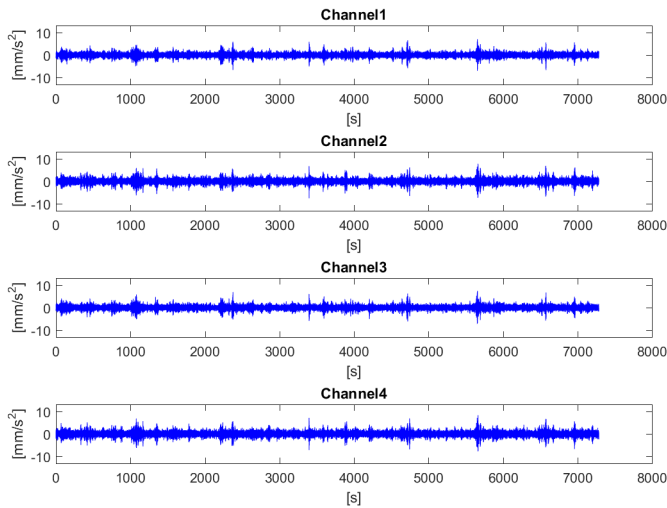


Figure B.32: Acceleration time series of each channel Day 2

B.2. RESULTS

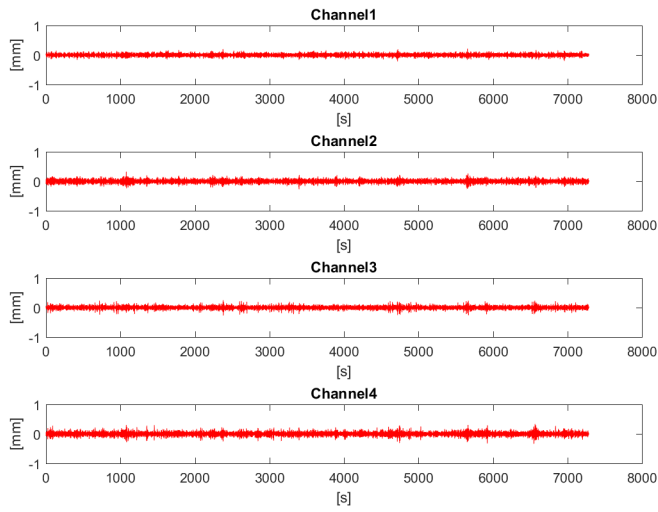


Figure B.33: Dynamic displacement time series of each channel Day 2

B TREE

Appendix C

Evaluation of Time Series

In this chapter some of the time series used to present the results are investigated and potentially validated. Evaluation of Moholt Two has not been included because it utilized the same FPGA VI architecture as Bergen Day 2.

C.1 Moholt One, Method 2

Method Two was intended to create hour-long time series measuring vibrations due to environmental loads during the weekend. When returning to the construction site approximately 72 hours later, only 50 files were recorded. The difference in the relative timestamped file names, using the unadjusted internal clock on the cRIO, show that a new file was created about every hour and 26 minutes. Scan mode was originally set to 1000Hz, which means that on an average sense, the sampling rate should be about $1000Hz \cdot \frac{1hour}{1.433hours} \approx 698Hz$.

The screws that were supposed to connect the accelerometers to the structure were not tested prior to the operation, and did not fit into the accelerometers. Instead, electrician tape was used. During the weekend, the tape holding the accelerometers in the 9th floor had loosened and the accelerometers were found misaligned relative to their indented coordinate system. Only the first time series has been used for the analysis. It is named *03_11_16__02_44_14 AM.tdms* together with the two next files showing the 1 hour 26 minutes timestamp differences. They can be found on the memory stick given to supervising professor Kjell Arne Malo [25].

C.2 Bergen Day 1

No timestamps were recorded on Day 1, and the recordings experienced on average a lowered sampling rate. The sampling rate was measured using a stop watch and looking at how many samples had been acquired. It was measured for 50000, 200000, 300000 and 3500000 samples and the resulting mean sampling rate was around 770Hz instead of the intended 1000Hz. Uncertainties to what information the FFT in MatLab provides arises when the sampling rate is no longer determined. The sources of error were investigated by implementing a Tick Count in two different VIs. The first VI had timestamps as the 9th channel, and the second VI had channel 8 replaced by a timestamp. Two VIs were created because a lowered sampling rate could indicate a sensitivity in regards to the amount of data being written on the Real-Time Target. The new VIs revealed four main sources of error causing the on average lowered and undetermined sampling rate. The time between each data point, δt , was also subject to indeterministic irregularities. Time series of 10 000 points were used to identify the sources of error causing the sampling rate. The time series used for investigation can be found in the digital appendix under the name *InvestigatingBergenDay1.xlsx*.

Source One: The scan engine used more than 1ms to acquire each data point, because a Real-Time Wait VI was used. This caused each for loop iteration to wait an extra ms before the next point was acquired instead of making every iteration last exactly 1ms. After investigating the timestamps of both VIs, it was found that all data where $\delta t \in [900\mu s, 8900\mu s]$, the mean value lies around $1341.5\mu s$. If this was the only source of error, the sampling rate should have been somewhere around $10^6(\mu s/s)/1341.5\mu s = 745.43Hz$.

It was also discovered variation for this data range with standard deviation $\sigma_{\delta t}$ around 350ms. Figure C.1 shows the effect of different variations of δt .

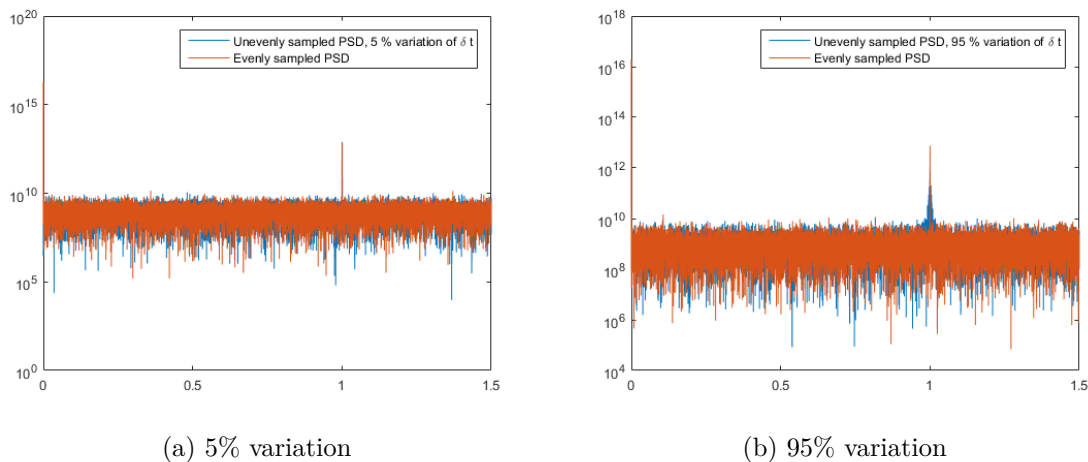


Figure C.1: Comparison of detected frequency at different variation in δt

The variation of δt is zero mean, thus the dominating detected frequency remains the same. The power seems to be distributed over a wider frequency band for wider variation of δt , and shows a similarity to the phenomenon *spectral leakage* discussed in subsection 3.5.4.

Source Two: On average, every 20th point sent into the FIFO experienced a sudden drop in δt , indicating that the Real-Time Wait did not wait 1ms between all samples. The timestamps show that when a drop occurs, the mean value lies around $320\mu s$, and has a standard deviation of $\sigma_{\delta t_{drop}} = 75\mu s$. The drops in δt should contribute to a higher sampling frequency on the average sense. By dropping every 20th point down to $320\mu s$, the sampling frequency should on average increase by:

$$\frac{20 * 1341.5\mu s}{19 * 1341.5\mu s + 350\mu s} = 3.84\%$$

Due to the standard deviation of the drop in δt , this effect should also introduce noise to the FFT the same way source one did. This effect alone would on average increase the sampling frequency from Source One up to $1.0384 * 745.43 = 774.03\text{Hz}$.

Source Three: After 1000 for loop iterations, an array of 8×1000 points were sent out to the TDMS-Write, and this process took several milliseconds. In both VIs, the time between each for loop was approximately between 9 and 14ms. This uncertainty in saving time should introduce noise the same way source one and two did. For simplicity, assuming the time spent on saving was on average 11.5ms, the sampling frequency should drop to approximately:

$$\frac{1341.5\mu s * 1000\text{points}}{1341.5\mu s * 1000\text{points} + 11500\mu s} = 99.15\%$$

Under the previous assumptions, the sampling frequency should be around $0.9915 * 774.03\text{Hz} = 767.45\text{Hz}$. The time series used to identify the errors were of entirely different length than the time series acquired on Bergen Day 1 (10 000 points with timestamps compared to 5 500 000 points on Day 1). Considering the fact that the statistical distributions and actual standard deviations of each source of error is unknown, the average sampling frequency could still be both higher or lower. The VIs used to detect the errors could also have been changing the sampling frequency themselves. Sources one, two and three introduce noise into the FFT, which in MatLab assumes evenly sampled data [1]. Assuming the average sampling frequency of 770Hz may not give the *exact* answer, and the results coming out of the analyses are expected to contain a higher level of uncertainty compared to a signal sampled more correctly. The results from Day 2 in Bergen confirms that Day 1 gave results representing the reality. Measurements from Day 1 detected fewer modes and contain less accurate results compared to Day 2.

C.3 Bergen Day 2, Scan Mode

Every 20th point was sent into the FIFO, and Scan Engine was set to 1000Hz. Hence, δt should be stable around $20\,000\mu s$.

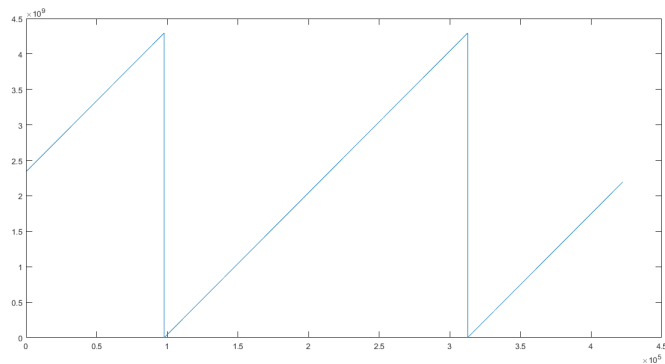


Figure C.2: Value of Tick Count in micro seconds

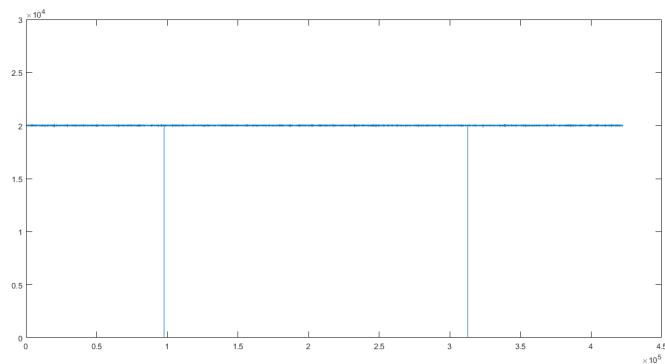


Figure C.3: Value of δt for every point being sent from the timed loop into the FIFO

Only two jumps were detected. They coincide with the Tick Count reaching its maximum value, and no data points were lost during this recording.

C.4 Bergen Day 2, FPGA

In LabVIEW, the VI providing timestamps was counting the number of micro seconds between each batch of data coming from the FPGA VI. Due to its numerical range, it reached its maximum value twice during a two hour recording. Below are plots showing the value of the timestamp and the difference between each timestamp $\delta t = t_{i+1} - t_i$.

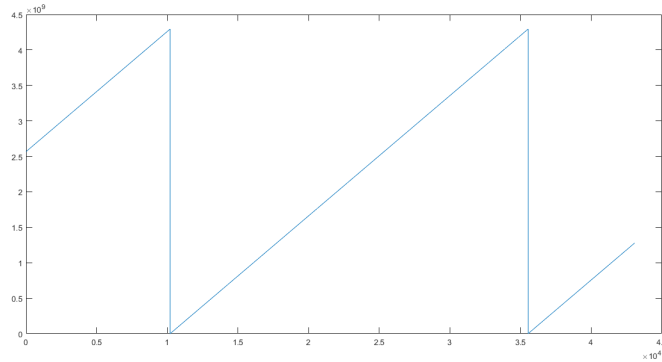


Figure C.4: Value of Tick Count in micro seconds

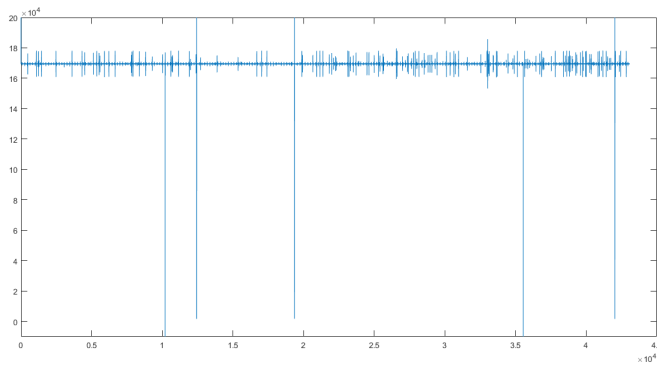


Figure C.5: Value of δt for every 280th point being sent into the FIFO

C EVALUATION OF TIME SERIES

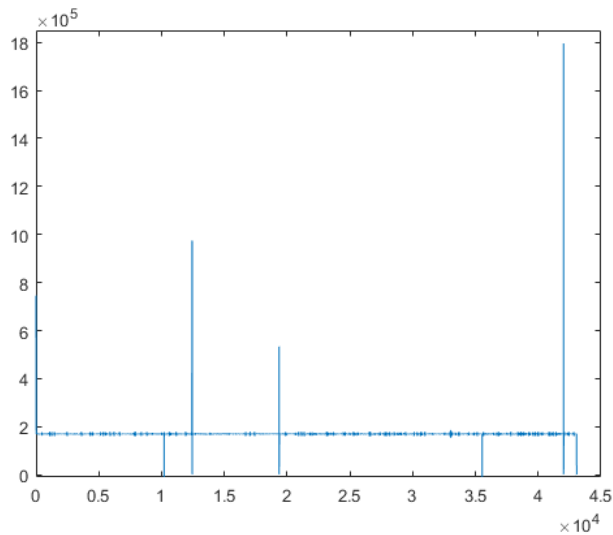


Figure C.6: Value of δt for every 280th point being sent into the FIFO

The upper plot shows the tick count value, and the lower plot shows the time difference between each batch of data coming out of the FIFO. Two drops are expected in the lower plot, because δt becomes negative when the Tick Count has to reset. Many smaller jumps can be seen throughout the time series, and are likely to be there because the timestamps are recorded on the receiving end of the FIFO. The smaller jumps in Figure C.5 are always followed by a few smaller drops, indicating that this is just the FIFO catching up. Three other large jumps could indicate that the FIFO was working slowly or experienced a time-out. A worst case would be that each unexpected jump is a time-out, and data points were lost. When looking at the largest value of δt , it is about $1800ms$. The time-out was set to $5000ms$, which means that no data points were lost throughout the time series.

C.5 Evaluation of Max. Acc. and Max. Dyn. Displ. Estimates

Welch's Estimate with the same number of windows and same amount of overlap has been used to estimate the APSD for both time series of Moholt Two, Method 2. Both time series are sampled at the same frequency and are two hours long. If it is assumed that the contribution to the APSD from the structural response is simply superimposed on to the APSD from measurement noise, the local increase in power within the response bandwidth should be able to describe the amplitude of the dominating harmonic component coming from the structural response. According to Strømmen, 2010 [43], the contribution to the APSD of a narrow banded process is related to the area under

C.5. EVALUATION OF MAX. ACC. AND MAX. DYN. DISPL. ESTIMATES

a peak in the APSD through the following relation

$$S(\omega_k) = \frac{c_k^2}{\Delta f} \quad (\text{C.1})$$

If the peaks related to the structural response in the APSDs are assumed to range over the same frequency band, Figures A.28 and A.37 indicate that the excitation caused by wind and site activity causes about 50 times the power of the excitation caused by wind only.

$$\frac{c_{WithActivity}}{c_{NoActivity}} = \frac{\sqrt{2\Delta f \cdot 50}}{\sqrt{2\Delta f \cdot 1}} \approx 7 \text{ times the response amplitudes.}$$

The assumptions made above might be too coarse, and introduce other errors that are not accounted for. When the power of the measurement noise is a significant contribution to the power of the signal, finding the response amplitudes through picking peaks in a filtered time series might not be very accurate. However, it seems reasonable that the response amplitudes of weak wind only are 7 times less the response amplitudes with construction activity close to the foundation of the building.

For all other time series recorded with environmental loading the response amplitudes exhibited sensitivity in regards to the cut-off frequencies of the lowpass and highpass filters. In other words, it does not seem likely that the reported response amplitudes are only from structural response, when a lot of energy in the remaining frequency band is measurement noise.

Appendix D

Hardware

This chapter contains key information about the accelerometers used to carry out the measurements in this thesis.

D.1 Accelerometer Power Inputs and Outputs

Accelerometer	Volt to m/s^2	Power Configuration
Kistler 8395A2D0ATTA00	4.905	AC Coupled
PCB Piezotronics 356A16	98.1	IEPE AC Coupled

Table D.1: Accelerometer information

D.2 Cables

Some of the cable lengths were never exactly measured, but Table D.2 shows their approximate lengths:

Cable Type	Length
Kistler	$10m \pm 2m$
PCB	$10m \pm 2m$
Coaxial Extension Cables	$20m \pm 2m$
Ethernet Cable	50m

Table D.2: Cable Lengths

Appendix E

Digital Appendix

In the digital appendix the following folders can be found:

Models

The model folder contains three different models of Moholt 50|50. The model used for the end results are *Moholt3.cae*. The three models are:

Moholt.cae Moholt2.cae Moholt3.cae

Matlab scripts

The Matlab script folder contain the matlab scripts used for processing the measurement data and show some aspects in regards to aliasing and uncertain sampling rates.

References

The references folder contain some downloaded pdfs of web pages and other sources used for the bibliography.

LabVIEW projects

The LabVIEW projects folder contain subfolders with the projects and VIs used during measurements. The subfolders are sorted by time and location.

E.1 Memory stick

Due to limitations regarding allowed file sizes of the digital appendix, the time series have been delivered to Kjell Arne Malo on a memory stick.

Time series

The time series folder contain all time series used for analyses and evaluation. It is split into subfolders sorted by time and location. In addition, and .xlsx file containing data basis for evaluation of Bergen Day 1 is included.